Interstellar Objects in a Galactic Context

Matthew James Hopkins

St John's College

University of Oxford

A thesis submitted for the degree of

Doctor of Philosophy

Trinity 2025

DECLARATION

I declare that no part of this thesis has been accepted, or is currently being submitted, for any degree or diploma or certificate or any other qualification in this University or elsewhere.

Matthew James Hopkins	2025-07-23

Acknowledgements

To Prof. Chris Lintott and Dr Michele Bannister, my supervisors: You are the giants on whose shoulders I have stood to see so far. Your vision, expertise and shared love of distracting ideas has not just made my DPhil possible, but made it the exciting and enlightening project that has been my pleasure to complete.

To Dr Ted Mackereth, who supervised me in my first year: thank you for helping to get my first published project off the ground, for teaching me what a selection function is, and for comparing me to the crazy pinboard man only once.

To Phil, Fergus, Rohan and James: I could have not have asked for a group of office/band/flatmates more kind, more intelligent, or more absurd to the point of hilarity, and I am so grateful to each of you.

To rest of Oxford Astrophysics: you have each made this department so welcoming, a place of many friends, and of fascinating, insightful, bohemian and sometimes even useful discussions.

To my family, for your unwavering support, and in particular to my brother Jonny, for always being there.

To old friends, Alice, Siv, Damien and Roman, for never leaving my side in any way but the physical: Our endless antics have brought me endless joy. Long may the stories continue!

To Pat and the Roche Lobes: You are each fantastic musicians individually, and together we formed a killer collective the likes of which no conference had seen. Send me a ticket when you're headlining NAM.

To the Donut Kings, especially Millie and Danny: You have given me big band music, a suspicion of Don Ellis, memories of a European tour that took years off my life, and a contempt for HSBC, all of which I will carry onwards with love.

And finally to Rough Edge, Oxford's ultimate party band, and especially Olly, J, Lynn, Leo, Henry and Maria, simply this: You made Oxford my home, and I cannot thank you enough.

To my friends, all of you: thank you.

Abstract

Interstellar objects (ISOs) form a vast Galaxy-spanning population with an number density $\sim 10^{15}\,\mathrm{pc}^{-3}$ in the Solar neighbourhood. Though only two members of this population have been observed, 1I/'Oumuamua and 2I/Borisov, the Vera C. Rubin's Legacy Survey of Space and Time (LSST) which begins later this year is expected to increase our sample of known ISOs by an order of magnitude. In this thesis I model the Milky Way's ISO population, across the Galactic disk, in the solar neighbourhood and streaming through the Solar System, in order to predict the properties of the LSST ISO sample. These predictions combine models of planetary and Galactic processes, and using a Bayesian framework I develop my predictions can be compared to the LSST ISO sample that is actually observed. By doing this, inferences can be drawn about any process modelled, allowing the study of phenomena across astrophysical scales with an entirely different set of biases to traditional observational methods.

Using debiased data from the the APOGEE Milky Way red giant survey I build a model of what the Galactic stellar population would be if stars did not die, naming this the *sine morte* population. By combining this with a protoplanetary disk chemical model I predict the ISO water mass fraction distribution and how this changes with Galactocentric radius, finding that the known stellar metallicity gradient has a matching ISO composition gradient. I demonstrate the Bayesian method of comparing my predictions to observed ISOs by placing constraints, albeit weak ones, on the metallicity dependence of ISO production using the measured composition of 2I/Borisov.

Next I predict the joint composition and velocity distribution, or chemodynamics, of ISOs in the solar neighbourhood. I debias a sample of stars from the *Gaia* survey within 200 pc, reconstruct the *sine morte* stellar population, then from this predict the ISO distribution using the same protoplanetary disk chemical model. I demonstrate that, like the stellar velocity distribution, the velocity distribution of ISOs is complex, with furrows and overdensities caused by orbital resonances with the Galactic spiral arms and bar, as well as correlated with properties such as age and composition. Both known ISOs have typical velocities within the boundaries of my predicted overdensities, and they share their velocities with stars with a range of ages and compositions. Finally I demonstrate that my predicted velocity

distribution could be distinguished from simpler Gaussian approximations used in previous works with ISO sample sizes within the capability of the LSST.

I devise a fast method of sampling observable ISO orbits through the Solar System, for use in simulation of surveys discovering ISOs. The innovations of this method significantly speed up survey simulation by avoiding sampling orbits which have no chance of being observed, allowing longer surveys and wider ranges of ISO sizes to be simulated, as well as increasing the statistical quality of the results. I also present the results of this survey simulation: the LSST ISO sample will consist of 6–51 ISOs dependant on the size distribution, most of them larger than 1I, with a slight discovery bias towards slower velocities relative to the Sun.

Changing tack slightly, I present a hypothesis that collisions between ISOs and neutron stars may be the cause of a significant fraction of fast radio bursts (FRBs), millisecond-length radio transients with many suggested origins. Such collisions are expected to cause FRB-like signals, and I demonstrate that they occur across the local Universe at a comparable volumetric rate to observable FRBs. I further argue that the rate of these collisions will have the same evolution with redshift as is observed in FRBs, and discuss other implications of the hypothesis.

Then changing tack quite significantly, I finish by using my APOGEE-based *sine morte* stellar population model to predict the distribution of single stellar black holes in the Milky way. I predict that though the Milky Way black hole population will show a strong gradient in occurrence relative to stars, this will only have a marginally detectable effect on the yield of the *Nancy Grace Roman Space Telescope*'s microlensing survey relative to larger uncertainties such as in the fraction of stars born which form black holes on their death.

Vue dans son ensemble, l'astronomie est le plus beau monument de l'esprit humain, le titre le plus noble de son intelligence... Conservons précieusement, augmentons même, le dépôt de ces hautes connaissances, les délices des êtres pensans.

— Pierre-Simon Laplace
Exposition du Système du Monde (1796)

'Here's harmony!' said she; 'Here's repose! Here's what may leave all painting and all music behind, and what poetry only can attempt to describe! Here's what may tranquilise every care, and lift the heart to rapture! When I look out on such a night as this, I feel as if there could be neither wickedness nor sorrow in the world; and there certainly would be less of both if the sublimity of Nature were more attended to, and people were carried more out of themselves by contemplating such a scene.'

— Fanny Price
Jane Austen's *Mansfield Park* (1814)

Essentially everything of astronomical interest is either part of a galaxy, or from a galaxy, or otherwise relevant to the origin or evolution of galaxies.

— Beatrice Muriel Hill Tinsley
Evolution of Stars and Gas in Galaxies (1980)

Contents

Rimmer, there's nothing out there, you know. There's nobody out there. No alien monsters, no Zargon warships . . . There's just you, me, the Cat, and a lot of floating smegging rocks. That's it. Finito.

— Lister, *Red Dwarf*

1 Introduction

1.1 History

1.1.1 The Öpik–Oort Cloud

Comets have been observed since ancient times, such as those recorded on ancient Chinese oracle bones (15th–11th centuries BCE; Zhen-Tao et al. 1995) or the *Sidus Iulium* described in the *Metamorphoses* (in Book XV; Ovid 8). Bright comets are visible to the naked eye as fuzzy comae with extended tails directed away from the Sun, making transient apparitions that last weeks or months. Though thought by many including Aristotle to be atmospheric phenomena as they are found displaced from the zodiac (Heidarzadeh 2008), they were shown to be external to the Earth's atmosphere by Tycho Brahe and Michael Maestlin who measured the parallax of the Great Comet of 1577, placing it at a distance of at least four times that of the Moon (Barker 2002). Realising that the comet apparitions of 1531, 1607, and 1682 were the same object, Halley (1704) predicted its return in 1759 and in that year was proven correct, 17 years after his death. The object was named after him, and 1P/Halley became the first known short-period comet.

Distinct from the short-period comets are the long-period comets. Whereas the short-period comets generally have periods of less than 200 years and low inclinations relative to the ecliptic, long-period comets enter the inner Solar system

on highly-elliptical ($e \lesssim 1$), parabolic ($e = 1$), or slightly-hyperbolic ($e \gtrsim 1$) orbits, with a wide range of inclinations. The tenuously-bound nature of these long-period comets meant their origins were debated until the mid-20$^{\text{th}}$ century. In his own doctoral thesis on the origin of these comets, Fabry (1893) concluded that «*L'absence des orbites fortement hyperboliques, parmi les comètes que nous voyons passer au périhélie, est inexplicable dans la théorie qui fait venir ces astres des espaces interstellaires. Nous concluons donc finalement que cette théorie doit être rejetée et que les comètes sont des membres permanents du système solaire*»[1], denouncing the theory first formalised by Laplace (1813) that comets originated in interstellar space. The possibility of an interstellar origin however remained under debate (cf. Lyttleton 1948; van Woerkom 1948).

The first step to what we now consider the correct theory was taken by Öpik (1932) who demonstrated that the perturbations from passing stars on comets on large semi-major axis and high-eccentricity orbits would both raise their perihelia and randomise their inclinations, forming a spherical cloud that would be remain bound, albeit tenuously, to the Sun. Following this Oort (1950) realised that this spherical cloud of comets, now called the Öpik–Oort cloud, was the natural result of small icy bodies being scattered by gravitational interactions with the giant planets shortly after the formation of the Solar System. These scattering events would place comets on highly elongated elliptical orbits, then the stellar perturbations studied by Öpik (1932) would raise their perihelia out of reach of the influence of the giant planets, saving them from further scattering which would result in their complete unbinding and ejection from the Solar System. The long-period comets we observe today are the small number of Öpik–Oort cloud objects which, by some additional perturbation, return to the inner Solar System on near-parabolic orbits.

Around this time the nature of comets as 'dirty snowballs', $\sim$ 1–10 km-diameter solid but low-density nuclei of dust and ice which begins to sublimate when the

[1] "The absence of strongly-hyperbolic orbits among the comets we have seen to pass perihelion is inexplicable by the theory that these stars [referring to the comets] come from interstellar space. We finally conclude that this theory should be rejected, and that comets are permanent members of the Solar System" (my translation).

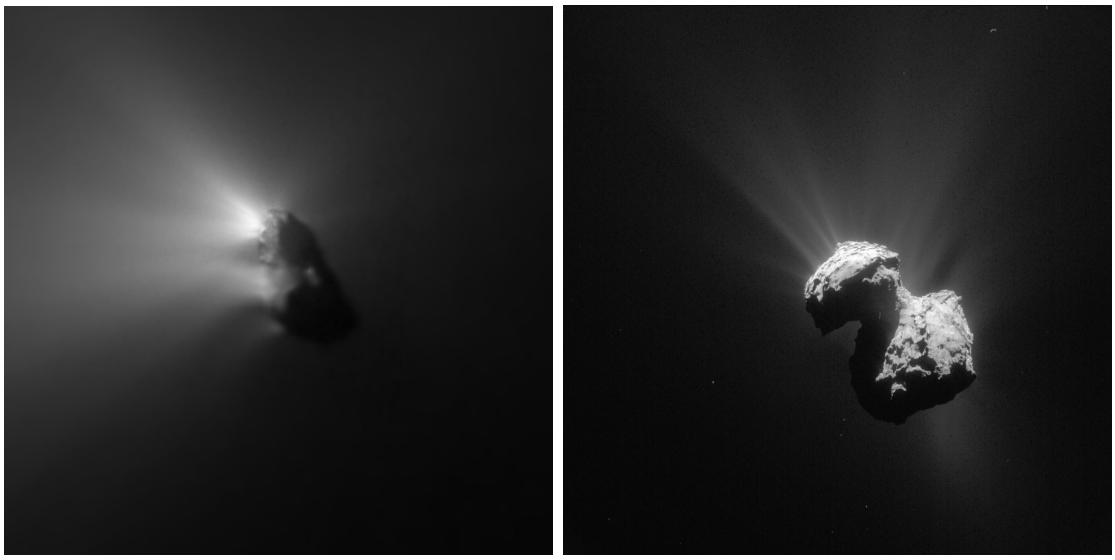

Figure 1.1: The nucleus of 1P/Halley (diameter 11 km) imaged by *Giotto* spacecraft on 1986-03-14 (left), and the nucleus of 67P/Churyumov–Gerasimenko (diameter 4 km) imaged by *Rosetta* spacecraft on 2015-07-07 (right).
Credit: ESA/MPS (left), ESA/Rosetta/NAVCAM (right)

comet approaches the Sun, was proposed by Whipple (1950, 1951, 1955). Though later refined to describe comet nuclei as 'icy dirtballs' instead (Keller 1989), this theory was confirmed over the 'flying sandbank' hypothesis of Lyttleton (1948) with spacecraft visits to comet nuclei starting with the 1986 apparition of Halley's comet (See Fig. 1.1).

The most relevant implication for this thesis of the existence of the Öpik–Oort cloud is that it implies the existence of a Galactic population of interstellar comets. Works such as those of Fernandez (1978) and Brasser et al. (2006) predict that the capture of comets into the Öpik–Oort cloud is highly inefficient: $\lesssim 10\%$ of the cometary bodies scattered by the giant planets are retained, with the rest being completely ejected. With $\sim 10^{12}$ comets in the Öpik–Oort cloud (Weissman 1983; Dones et al. 2004), this implies the Sun alone ejected $\gtrsim 10^{13}$ cometary objects into the Galaxy. Under a Copernican assumption that other stars contribute a similar number of objects, ejected small bodies must form a huge Galactic population.

1.1.2 The Search for Interstellar Comets

Since the formation of the Öpik–Oort cloud implied the existence of comets in interstellar space, which should on occasion pass through the Solar system on hyperbolic orbit, the following question could be posed: Was the lack of detections of these interstellar comets consistent with our expectations for planetary system formation?

As noted by Fabry (1893), orbit determinations have been sufficiently accurate since the early 19$^{\text{th}}$ century that had an interstellar comet been observed, it would have been characterised as such. Using the lack of observations in the preceding century, Sekanina (1976) places an upper limit on the mass density of interstellar comets in the solar neighbourhood of $\sim 200 M_{\oplus}\text{pc}^{-3}$. This is consistent with modern estimates (Do et al. (2018) estimate a mass density of $\sim 4 M_{\oplus}\text{pc}^{-3}$ from the detection of 1I/'Oumuamua, discussed below).

McGlynn and Chapman (1989) were the first to discuss the potential tension between models and nondetections. Using previous numerical modelling work on the formation of the Öpik–Oort cloud they used a capture efficiency of $\sim 1\%$ with an Öpik–Oort cloud size of $\sim 10^{12}$ to estimate that the Solar system produced $\sim 10^{14}$ interstellar comets. Assuming every star ejected a similar number, they then predicted a number density of interstellar comets of $\sim 10^{13}\,\text{pc}^{-3} \simeq 10^{-3}\,\text{au}^{-3}$. With this they calculate that several strongly-hyperbolic comets should have been detected passing through the inner Solar System in the last 150 years, and discuss the implications of this discrepancy. Stern (1990) further formalises this discrepancy, calculating a constraint relating the fraction of stars which form exo-Öpik–Oort clouds, their average size, and the efficiency of capture of comets into them.

Both works discount the possibilities of these interstellar comets being significantly harder to detect than long-period comets or destroyed by some process in interstellar space. Though they suggest the possibility that the Sun may be rare in having a planetary system, both mainly argue that the number of comets ejected from the Solar System must have been exaggerated. With a modern perspective this is what appears to be the cause of the discrepancy: we now know planetary

systems are common, implying many stars eject a comparable number of interstellar comets to the Sun, but the number ejected is now thought to be smaller by approximately an order of magnitude due to a higher capture efficiency of comets into the Öpik–Oort cloud of $\sim 10\%$ (Brasser et al. 2006).

Moro-Martín et al. (2009) took a different approach to estimate the number of inactive interstellar comets (i.e. those not showing cometary activity) expected to be observed in the upcoming Legacy Survey of Space and Time, or LSST (Ivezić et al. 2019). They did this by estimating the total mass that is ejected from protoplanetary disks to form interstellar comets, then divided this into realistic size distributions from Solar System small body populations. With this they predicted an upper limit on the number density of objects with diameter greater than 1 km of $\sim 10^{-6}\,\mathrm{au}^{-3}$, three orders of magnitude smaller than the estimated density of McGlynn and Chapman (1989), and concluded that it was not surprising that none had been discovered. Cook et al. (2016) extended the work of Moro-Martín et al. (2009) to include active interstellar comets, and concluded similarly: "Frankly, some optimism is required to conclude that LSST will detect even one interstellar object". From this point onwards, in both the literature and this thesis, the term "interstellar object" or ISO is used to refer to both inactive and active interstellar small bodies. Using non-detections in Pan-STARRS1, the Mt. Lemmon Survey, and the Catalina Sky Survey, Engelhardt et al. (2017) placed an upper limit on the density of inactive ISOs with diameter greater than 1 km of $\sim 2 \times 10^{-2}\,\mathrm{au}^{-3}$ and, six months before the discovery of 1I/'Oumuamua, concluded "The prospects for identifying a large chunk of material ejected by an extra-solar system passing through our own Solar System appear to be bleak".

Each of these works predicting a continued lack of detections of ISOs each assumed that ISOs would be large (> 1 km in diameter) cometary objects, based on a presumed similarity to Öpik–Oort cloud comets. It is for this reason that the discovery of 1I/2017 U1 ('Oumuamua) was unexpected.

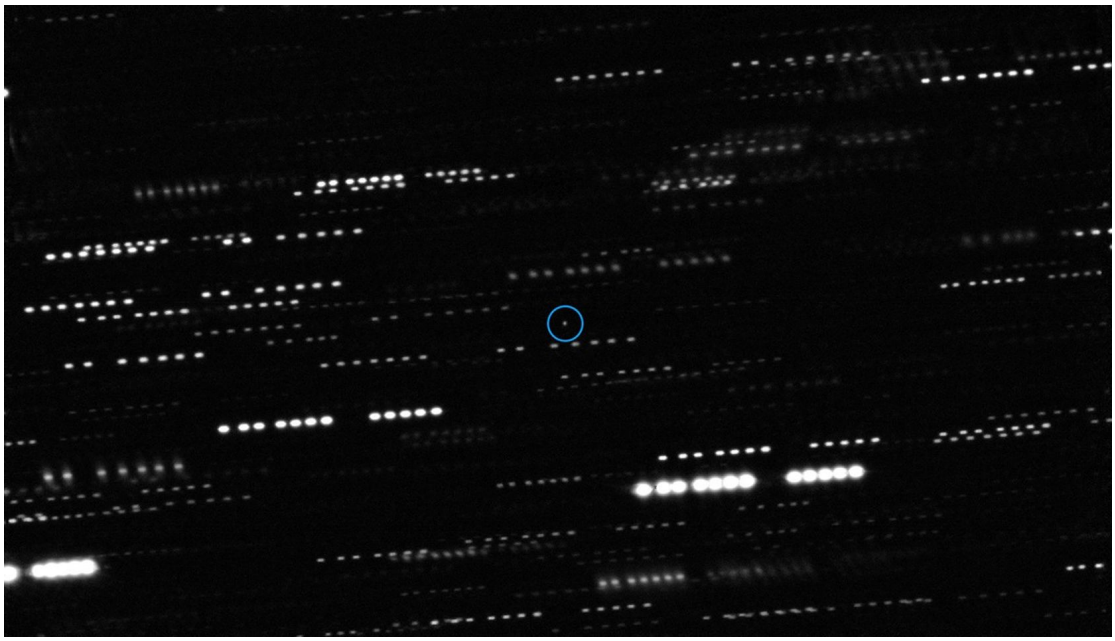

Figure 1.2: A deep stacked image of 1I/2017 U1 (‘Oumuamua), circled, combining images from the VLT and the Gemini South telescope (25th–27th October 2017). Its rapid proper motion causes the background stars to form streaks over the integration time, and the lack of observed coma prompted 1I’s first change in designation.
Credit: ESO/K. Meech et al.

1.2 1I/2017 U1 (‘Oumuamua)

1.2.1 An Unexpected Discovery

The discovery of 1I/2017 U1 (‘Oumuamua) was surprising in many ways. In addition to being thought so rarefied as to be undetectable, ISOs were expected to be cometary in nature.[2] This caused some confusion in nomenclature: Its discovery announcement on 2017-10-25 with a data-arc span of only 6 days classified it as a long-period comet (a class which includes hyperbolic comets). The following night in a deep stacked image taken with the Very Large Telescope (VLT) no observable cometary activity was reported (Fig. 1.2), resulting in the first of ‘Oumuamua’s redesignations to A/2017 U1 (MPEC 2017-U183) as ‘a minor planet misdesignated as a comet’ (*Minor Planet Circulars* 23803), the first time an A/ designation had been used. Within two weeks however 1I received its second and final redesignation to 1I/2017 U1 (‘Oumuamua), the first of the I/ designations, invented to accommodate true ISOs

[2]N.B. Non-cometary objects from the Öpik–Ort cloud (‘Manx comets’, for they lack a tail) had been and continue to be discovered (Meech et al. 2016), but these are in the minority.

and differentiate them from the weakly-hyperbolic LPCs with Solar System origins (MPEC 2017-V17). For ease of both reading and typing, 1I/2017 U1 (ʻOumuamua) is also referred to in the literature and this thesis by 1I/ʻOumuamua, ʻOumuamua, or simply 1I. The Pan-STARRS team chose the name ʻOumuamua; it is derived from the language of Hawaiʻi and its meaning "reflects the way this object is like a scout or messenger sent from the distant past to reach out to us" (MPEC 2017-V17).

On discovery 1I was clearly hyperbolic, with its announcement (MPEC 2017-U181)listing a short-arc orbit fit with an inverse semi-major axis of $1/a = (-0.75 \pm 0.02)\,\mathrm{au}^{-1}$, implying a clearly interstellar excess velocity of $v_\infty = \sqrt{-GM_\odot/a} = (25.9 \pm 0.3)\,\mathrm{km\,s}^{-1}$. This was later refined with further observations forming an 80-day arc, to which has been fit a hyperbolic orbit with an inverse semi-major axis $1/a = (-0.7860 \pm 0.0001)\,\mathrm{au}$ and eccentricity $e = 1.201\,13 \pm 0.000\,02$, listed in the JPL Small-Body Database[3], by Davide Farnocchia. With no known mechanism of accelerating a bound Solar System object to this speed (Schneider 2017), ʻOumuamua was widely recognised as the first true ISO to be discovered.

The discovery announcement sparked a flurry of observations before ʻOumuamua passed too far away and dimmed beyond the magnitude limit of detectability, as it had already passed both perihelion (2017-09-09) and its closest approach to Earth (2017-10-14). A spectrum acquired the night of the announcement by Masiero (2017) with the DBSP optical spectrograph (Oke and Gunn 1982) on Palomar Observatory's 5 m Hale Telescope, albeit with low signal-to-noise, showed 1I to have a red spectral slope with no significant features. The following night using the same telescope, Ye et al. (2017) carried out imaging to confirm the lack of visible coma, and using the same DBSP instrument reproduced a similar featureless red spectrum; using this they put upper limits on 1I's emission of common cometary species CN, C_2, and C_3. Observations over the following week confirmed lack of a coma, non-detections of outgassing of species including OH (Park et al. 2018), CO, CO_2 and dust (Trilling et al. 2018; Hui and Knight 2019), as well as the non-detection of radio transmissions (Harp et al. 2019).

[3] https://ssd.jpl.nasa.gov/tools/sbdb_lookup.html#/?sstr=1I

In photometry, 1I was measured to be slightly redder than Solar colours, consistent with the more colour-neutral Solar system populations such as D-type Jupiter Trojans and the dynamically-excited populations of trans-Neptunian objects, but inconsistent with the ultra-red, dynamically-cold classical Kuiper belt objects (Jewitt et al. 2017; Bannister et al. 2017). Notably, these Solar System objects that 1I is most similar to in colour are thought to have formed at intermediate distances from the Sun, closer than than the cold classical Kuiper belt objects (Nesvorný 2018; Schwamb et al. 2019). Thermal modelling by Fitzsimmons et al. (2018) showed that 1I's lack of cometary activity may be reconciled with a icy interior if long-term cosmic ray exposure created a devolatised, insulating crust.

From its photometry and assumptions about its phase curve, 1I's visual-band absolute magnitude[4] was variously estimated to be $H_V = 22.4$ (Meech et al. 2017), $H_V = 22.95$ (Jewitt et al. 2017), $H_V = 22.8$ (Knight et al. 2017), and $H_V = 22.1$ (Drahus et al. 2018). Though its albedo was not measured, under the common assumption of an albedo of ~ 0.04 these works each find 1I to have a size of $\sim 100\,\mathrm{m}$. This is small, smaller than the objects modelled in any of the studies predicting the observability of ISOs in §1.1.2.

Amidst these observations, an additional surprising feature of 1I's reflected light became apparent: huge 2 mag-amplitude variations in its light curve on a timescale of hours. Under the assumption of a constant albedo across its surface, this variation implied 'Oumuamua had a highly elongated or flattened shape with a longest-to-shortest axis ratio of at least 5:1, higher than any Solar System body observed before or since (Meech et al. 2017; Knight et al. 2017; Bannister et al. 2017; Bolin et al. 2018). Additionally, variation between rotation cycles found by Fraser et al. (2018) and Drahus et al. (2018) implies non-principal-axis rotation or 'tumbling', implying a collision in the object's past. Fraser et al. (2018) additionlly finds evidence of colour variation across the surface of 1I similar to some Kuiper belt objects. Belton et al. (2018) find that both an elongated 'cigar' shape and a flattened oblate 'disk' are consistent with the lightcurve, but Mashchenko (2019)

[4]for a full introduction to the small-body absolute magnitude, see §4.2.1

actually fit the light curve with a range of complex physical models. They find that for all shapes some torque on 1I is necessary to explain the timings of deep light curve minima. They find that the two best fitting ellipsoidal shapes for 1I/'Oumuamua are an elongated 'cigar' (axis ratios $\frac{b}{a} \simeq \frac{c}{a} = 0.13$) and a flattened 'disk' (axis ratios $\frac{b}{a} = 0.96$, $\frac{c}{a} = 0.16$), with a preference for the disk model as the cigar model faces a fine-tuning problem: for a random orientation of the angular momentum vector, the cigar model has only a 16% chance of reproducing the light curve, compared to the disk model's 91% chance.

The final surprise of 1I/'Oumuamua was revealed by Micheli et al. (2018) with high-quality astrometry using data from several telescopes over the ISO's full 80-day arc of observation, including its final detection in images from the Hubble Space Telescope (HST) on 2018-01-02. As it receded from the inner Solar System 1I demonstrated non-gravitational acceleration, deviating slightly but significantly[5] away from a purely gravitational hyperbolic orbit. Non-gravitational acceleration is commonly detected in the orbits of comets (Marsden et al. 1973; Yeomans 1994; Yabushita 1996; Królikowska 2004), driven by the same sublimation and outgassing of ices such as H2O, N2, CO which drives their cometary activity. However, 1I/'Oumuamua showed no such visible cometary activity or detectable outgassing.

1.2.2 Inferred Quantities

The discovery of 1I in Pan-STARRS, a characterised survey, allowed the number density of ISOs to be inferred. By estimating the volume of the Solar System Pan-STARRS has surveyed for objects of 1I's size or greater, Do et al. (2018) used the single detection of an ISO in that volume to estimate the number density of ISOs larger than 1I to be $n \sim 0.2\,\mathrm{au}^{-3}$. Since the number of ISOs observed in a characterised survey is a Poisson statistic with a value of 1, therefore also a variance of 1, the uncertainty on the Do et al. (2018) number density is high (Flekkøy and Toussaint 2023). As Pan-STARRS has continued to survey since

[5]With 30σ-significance, to be punctilious.

2017 and found no more ISOs, throughout this thesis I use a conservative value of $n \sim 0.1\,\mathrm{au}^{-3}$ for the density of 1I-sized ISOs.

This number density is actually perfectly consistent with the humorously antiprescient conclusion of Engelhardt et al. (2017) described in §1.1.2. Engelhardt et al. (2017) estimate an upper limit of $2.4 \times 10^{-2}\,\mathrm{au}^{-3}$ on the ISO number density for ISOs without cometary activity of absolute magnitude $H_V = 19.1$ and brighter (corresponding to diameter larger than 1 km for albedos of 0.04). Under the absolute magnitude distribution assumed by Engelhardt et al. (2017) ($n \propto 10^{0.5H_V}$) the density of $H_V \leq 19.1$ ISOs would be fifty times less than the density of 1I-sized ISOs with $H_V \leq 22.5$. Scaling the density estimate of Do et al. (2018) by this factor gives a density of $H_V \leq 19.1$ ISOs as $n \sim 2 \times 10^{-3}\,\mathrm{au}^{-3}$, an order of magnitude below the upper limit of Engelhardt et al. (2017). Thus the discrepancy between Engelhardt et al. (2017)'s conclusion that the prospects for discovering ISOs looked bleak and the discovery of 1I six months later is simply because no pre-1I study considered such a small, non-cometary object as a possibility.

A further inference made was the age of 1I. The relaxation timescale of an object's excited rotation state can be used to put weak constraints on its age; Fraser et al. (2018) and Drahus et al. (2018) each do this and estimate ages of $\lesssim 10^3$ Gyr and $\lesssim 1$ Gyr respectively. These estimates assume a typical Solar System small body composition, though 1I's true structure and composition remain unknown. Almeida-Fernandes and Rocha-Pinto (2018a) used the stellar age-velocity dispersion relation (Nordström et al. 2004) to place much stronger constraints on the age of 1I. The age-velocity dispersion relation is a result of objects in the Galactic disk scattering off giant molecular clouds, increasing the eccentricities of their orbits (Lacey 1984; Almeida-Fernandes and Rocha-Pinto 2018b), and should affect both stars and ISOs equally. Almeida-Fernandes and Rocha-Pinto (2018a) estimate an age of 1I to be within 200 Myr to 450 Myr, however this is subject to the models of the age-velocity dispersion relation they used.

1.2.3 Hypotheses of Origin

The discovery of 1I was extraordinary: if any ISOs were expected at all, they had been expected to have similar properties to Öpik–Oort cloud comets. Instead, we got something apparently unlike anything seen in the Solar System. This led to the development of hypotheses for its origin that explained its odd collection of properties in a unified manner. Here I discuss these origin hypotheses, grouped by the observed property of 1I each tried to explain.

Since it is highly unlikely that first discovered ISO is highly unusual among ISOs, these hypotheses needed to not just explain how to form an object like 1I, but how to make a large fraction of ISOs like 1I. However, since 1I was unusual compared to Solar System objects, any hypothesis to explain the formation of 1I-like objects also needed to explain why such objects are not found bound to the Sun. This could be done in one of two ways: either 1I-like objects can form in Solar System-like planetary systems but are almost all ejected, or 1I-type objects do not form in Solar System-like systems.

1.2.3.1 Shape

With its extreme axis ratio and tumbling motion, many hypothesised that 1I originated as a fragment of a larger body produced in either a collision or a tidal disruption event. Drahus et al. (2018) ruled out the possibility of this occurring in the Solar System as the debris it would have caused would have been observable, implying if 1I experienced such a violent event it must have occurred in 1I's birth planetary system. Furthermore, 1I being fragmentary would resolve a possible issue: Moro-Martín (2018) argues that the mass density of ISOs implied by the measured number density of Do et al. (2018) is incompatible with the mass budget of material that can be ejected from protoplanetary disks, under the assumption that ISO follow a Solar System size distribution. If instead 1I along with a large fraction of ISOs were fragments, this would create a different size distribution, dominated by small objects, which would not exceed the mass budget for protoplanetary disk ejecta. Zhang and Lin (2020) further demonstrate by numerical modelling

that tidal disruption produces mainly prolate high-axis-ratio shapes, such as the 'cigar' shape that 1I may have.

Since 1I broke the expectation that ISOs would be cometary, several hypotheses attempted to explain how apparently asteroidal ISOs could be produced, largely by placing the origin of 1I in a planetary system unlike our own. Suggesting binary star systems as efficient ejectors of small bodies, Ćuk (2018) argue that systems containing a dense red dwarf star would tidally disrupt terrestrial planets and eject the fragments, and relatively few terrestrial planets would have to be disrupted to cause fragments to dominate the ISO population by number. Jackson et al. (2018) argue binary A- and B- type stars would eject asteroidal objects from the inner parts of their circumbinary disks, during which an ISO may be heated to point of melting then re-solidifing into an oblate shape with a large axis oblate shape ratio due to its spin. Katz (2018) explain the large axis ratio in a similar manner, except suggesting 1I was released from its parent system by stellar mass loss at the end of its parent stars life. In this case, heating is provided by the increase in luminosity of the parent star when it enters the giant phase, driving off volatiles and temporarily fluidising the object. Rafikov (2018a) also suggest an origin for ISOs at the end of their parent star's life, however they argue for fragmentation by the resulting white dwarf, using commonly observed white dwarf pollution (Farihi 2016) to justify the feasibility of such a scenario. Finally, returning to binary stellar systems, Childs and Martin (2022) argue small bodies in highly-inclined circumbinary disks will be subject to nodal precession and high-speed collisions, producing many interstellar fragments. However, these hypotheses would produce completely volatile-free ISOs, and therefore are possibly excluded for the origin of 1I by its observed non-gravitational acceleration.

1I-like objects may also be sourced from Solar System-like systems. Raymond et al. (2018a,b) argue a large number of ISOs will be formed by the tidal disruption and ejection of comets by giant planets such as Jupiter and Neptune. These fragments will have their surfaces devolatised by close passes to their parent star before ejection, resulting in extinct objects with colours, spectra and shapes comparable to

1I, while retaining the interior volatiles which may have driven its non-gravitational acceleration. Additionally—and crucially—Raymond et al. (2020) demonstrate the differences between the ejected and retained small body populations required to explain why a devolatised, fragmentary object like 1I has not been observed bound to the Solar System.

There are some non-violent hypotheses for 1I's shape, which suppose instead that it developed in interstellar space: Domokos et al. (2017) and Vavilov and Medvedev (2019) suggest 'bar of soap' erosion by dust bombardment in interstellar space could increase the axis ratio over time to the extreme value observed. Lorek and Johansen (2024) also demonstrated that highly oblate shapes can be created on formation by the gravitational collapse of rotating clumps of pebbles in the protoplanetary disk. However, neither of these hypotheses immediately explain why such extreme shapes are not seen in bound Solar System objects.

1.2.3.2 Outgassing

In their announcement of the detection of 1I's non-gravitational acceleration, Micheli et al. (2018) suggest that, despite the lack of observed cometary activity, outgassing remained the most likely cause of the anomalous motion. Here I describe outgassing-based explanations of the non-gravitational acceleration.

Their thermal model assumes a jet composed of a mixture of H_2O and CO, and explains the anomalous acceleration without being inconsistent with the upper limit on the water OH dissociation product set by Park et al. (2018), However, upper limits on outgassing of CO and CO_2 in *Spitzer* observations by Trilling et al. (2018) ruled out the CO contribution to this, and Sekanina (2019b) rules out H_2O outgassing as the driver of the observed non-gravitational acceleration as none of the acceleration profiles which fit the data of Micheli et al. (2018) are compatible with the H_2O sublimation law of Marsden et al. (1973).

With these common cometary species ruled out as drivers of outgassing, the possibilities of alternative volatiles were explored. These hypotheses are exotic, requiring compositions for 1I never observed in Solar System bodies; however,

they do explain both observed aspects of 1I as well as why these aspects are not observed in Solar System bodies. Seligman and Laughlin (2020) established that the outgassed species must be a hypervolatile with a low enthalpy of sublimation in order for the energy required to outgass it to be less than 1I's total solar irradiation. They propose H_2 as a candidate, suggesting 1I was a body of solid hydrogen ice formed in a giant molecular cloud core, a possibility further explored by Levine and Laughlin (2021). Such objects would be fundamentally interstellar, unable to survive long in the Solar System, and rapid erosion by cosmic rays in this model explains the large axis ratio, as well as the oft-quoted young age for 1I (however see my discussion of this in §3.4.2).

Inspired by the discovery by the *New Horizons* spacecraft (Young et al. 2008) that large fractions of the surface of Pluto is covered in pure nitrogen ice (Protopapa et al. 2017), Jackson and Desch (2021) and Desch and Jackson (2021) propose 1I and a large number of ISOs are fragments of solid N_2 ice formed by collisions onto the surfaces of Pluto-like exoplanets. The collisional origin of these fragments explains the extreme shape and tumbling of 1I. It is argued that erosion to destruction by cosmic rays would prevent any nitrogen ice fragments created in the early Solar System surviving long enough to be observed coming from the Oort cloud, meaning such objects will only be observed in the ISO population. Both of these exotic ice hypotheses however are not without issues (Hoang and Loeb 2020; Levine et al. 2021; Phan et al. 2021; Siraj and Loeb 2022).

Other hypotheses without exotic compositions also exist: Seligman et al. (2021) argue that the outgassed species may in fact be CO, despite *Spitzer* upper limits, suggesting that the outgassing was highly variable and happened to be at a minimum during the 30 h-period (2017 November 21-22) the *Spitzer* observations were made (Trilling et al. 2018). Finally, Bergner and Seligman (2023a) suggest a H_2O ice body, irradiated by cosmic rays, will build up trapped H_2 that is then released and outgassed on warming as it approaches the Sun, however the feasibility of this process is a matter of debate (Ligterink 2023; Bergner and Seligman 2023b; Hoang and Loeb 2023).

Despite the lack of a single clearly-favoured outgassing-based model for the non-gravitational acceleration of 1I, there is evidence that 1I experienced some form of outgassing in features of its light curve. Soon after the discovery of 1I's non-gravitational acceleration, Rafikov (2018b) argued that, under torque asymmetry typical of Solar System comets, the level of outgassing required to explain it would cause rapid spin evolution in 1I, incompatible with the observed stability of its light curve and leading to its destruction. These results however are contested by the dynamical model developed in Seligman et al. (2019), Seligman et al. (2021), and Taylor et al. (2023), which demonstrates that outgassing from a sub-Solar jet would avoid this spin-up and actually explain some features of the light curve. Additionally Mashchenko (2019), who carried out the most comprehensive analysis of 1I's shape, found that all of the shape models they tested required some torque to explain the timing of the deep dips in the light curve.

Since the discovery of 1I/'Oumuamua a small number of 'dark comets', also with no visible coma but detectable non-gravitational acceleration, have been discovered in the Solar System asteroid belt (Chesley et al. 2016; Farnocchia et al. 2023; Seligman et al. 2023). The motion of these objects may provide a Solar System analogue to 1I's non-gravitational acceleration, and it is suggested to be driven by outgassing (Taylor et al. 2024a,b).

1.2.3.3 Radiation Pressure

With no clearly-favoured outgassing-based explanation for the non-gravitational acceleration, radiation pressure from the Sun was explored as an alternative. Radiation pressure has been measured to affect the orbits of some small Solar System asteroids (Vokrouhlický and Milani 2000; Deo and Kushvah 2017), however it has an incredibly minor effect compared to processes such as outgassing or other radiation-based processes such as the Yarkovsky effect (Öpik 1951). For the tiny force radiation pressure exerts on an object of 1I's inferred size to induce a measurable non-gravitational acceleration, 1I would have to have an exceedingly low mass (Newton 1687).

Moro-Martín (2019), Flekkøy et al. (2019), and Luu et al. (2020) each discuss the possibility of 1I/'Oumuamua being a fractal aggregate, a hypothetical incredibly low density ($\sim 10^{-5}\,\mathrm{g\,cm^{-3}}$), high-axis-ratio collection of dust grains formed in the comae of comets then ejected from their home planetary systems into interstellar space by radiation pressure from their parent star. Sekanina (2019a) proposes a similar aggregate structure, but places its origin instead in the disintegration of an unobserved small interstellar comet, leaving a remnant that we observed as 1I. This explanation however does not account for the lack of observed 1I-like objects originating from the Solar System.

Bialy and Loeb (2018) suggest an alternative structure that would allow the Sun's radiation pressure to provide the observed non-gravitational acceleration: a thin sheet of surface density $\simeq 0.1\,\mathrm{g\,cm^{-2}}$ and thickness $< 1\,\mathrm{mm}$, a shape compatible with the modelling at the time which suggested an oblate disk shape for 1I (Belton et al. 2018) and had only placed an upper limit on its shortest-to-longest axis ratio (of 0.2; Drahus et al. 2018). They argue that if 1I had this structure it cannot have formed naturally, and instead must have been deliberately constructed by an intelligent alien civilisation, surmising that it was designed as a solar sail. To rationalise this 'technosignature' hypothesis, Bialy and Loeb (2018) calculate that such an object would not be rapidly destroyed in the interstellar environment, and Loeb (2022) makes the observation that some Solar System objects with anomalous acceleration such as 2020 SO (MPEC 2020-S78) are later discovered to be human-made space junk (but not all: Spada 2025; McDowell 2025).

The technosignature hypothesis for ISOs has some obvious issues. 'Oumuamua ISSI Team et al. (2019) reviewed the known properties of 1I and the hypotheses at the time for its origin and found no compelling evidence for a technological origin. Due to the unconstrained abundance and nature of intelligent extraterrestrial civilisations, the technosignature hypothesis lacks predictive power for the properties of the ISO population in general. Where it does have predictive power, which is for the properties of 1I/'Oumuamua alone, it does not match the observational data. Mashchenko (2019) shows that a thin solar sail model provides a 'noticeably worse'

fit to 1I's light curve than less extreme shapes. Modelling by Zhou et al. (2022) shows that a solar sail would be likely to demonstrate significantly larger light curve amplitudes than was observed for 1I, as well as a noticeable level of sideways non-gravitational acceleration beyond the radial acceleration observed by Micheli et al. (2018). Furthermore, whereas the human-made object of 2020 SO, used as an example by Loeb (2022), was clearly deduced to be artificial in photometry and spectroscopy (Reddy et al. 2021), 1I/'Oumuamua has colours and a spectrum consistent with natural Solar System objects (see the many works discussed in §1.2.1).

Cowie (2021) takes a philosophical approach to the technosignature origin for 1I/'Oumuamua, and argue that the structure of the underlying argument is flawed. The technosignature hypothesis relies on a misleading eliminative argument: that a technological origin for 1I is the only remaining viable hypothesis because all conceivable natural explanations have been exhaustively eliminated (Loeb 2021). This is not the case, and in order to make this argument properly proponents of the technosignature hypothesis would need to demonstrate the following: Firstly, that any natural origin hypothesis (including any currently unconceived alternatives; Stanford 2006) has a negligible likelihood of being correct—a daunting task, not accomplished. Secondly, that the prior probability[6] of any discovered object having a technological origin is non-negligible. This is also difficult to achieve given the extreme uncertainty in the abundance of technologically-capable extraterrestrial civilisations, largely due to the lack of detections in decades of searches (Wright 2022). Cowie (2021) argues that the above points have not been demonstrated, and this constitutes an argument from uncertainty against the technosignature hypothesis.

Regardless of how unlikely a natural origin for 1I/'Oumuamua appears with our current and incomplete knowledge of small bodies, by application of Occam's razor it is still more competitive than any hypothesis that requires the invocation of an as-of-yet completely unobserved class of extraterrestrial technological civilisations. This will remain the case until proponents of the the technosignature hypothesis can demonstrate that the existence of discoverable extraterrestrial technosignatures

[6]If these terms sound Bayesian, that's because they are (see §1.6).

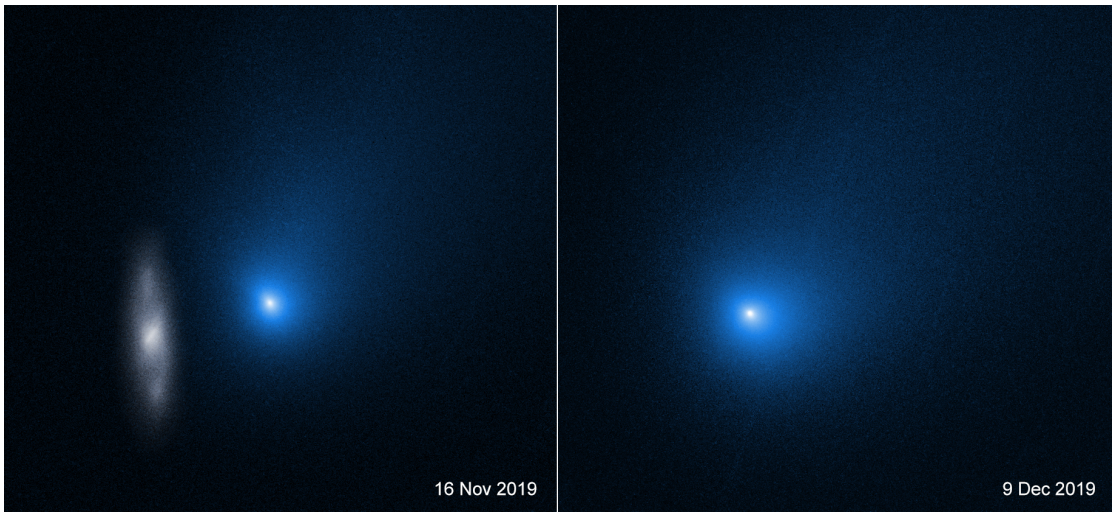

Figure 1.3: 2I/2019 Q4 (Borisov), shortly before (left) and at (right) perihelion. *Credit: NASA, ESA and D. Jewitt (UCLA)*

is not negligibly unlikely. This would be best demonstrated with the detection and completely unambiguous characterisation of a different technosignature, either in the form of a physical object found in our Solar system or a telescopic signal such as those sought by SETI (Ekers et al. 2002) and Breakthrough Listen (Worden et al. 2017). This is not a circular argument: Completely unambiguous characterisation of a technosignature is remarkably difficult to achieve but is not impossible; it would however require more carefully constructed arguments and stronger evidence than are currently available for the technosignature hypothesis for 1I/ʻOumuamua.

The above is just the threshold that must be met in order to make the technosignature hypothesis for 1I plausible. If this was achieved, the technosignature hypothesis would then have to compete with natural-origin hypotheses on the merits of how well it matches the observed properties of 1I, and as discussed above it would struggle. To summarise, even if extraterrestrial technological civilisations had been observed and were known to exist, a technological origin for 1I/ʻOumuamua would remain unconvincing.

1.3 2I/2019 Q4 (Borisov)

Discovered by astronomer Gennadiy Borisov on 2019-08-29, 2I/2019 Q4 (Borisov) is the second object discovered on an interstellar trajectory (MPEC 2019-R106;

MPEC 2019-S72). Unlike 1I/'Oumuamua, 2I/Borisov showed clear cometary activity, exactly had been expected for ISOs since their first predictions. In addition to confirming the predicted existence of a population of cometary ISOs, this presented the possibility of detecting molecular species in its spectra, and measuring the composition of an object formed in another planetary system. However, being discovered outside of a characterised survey meant that its discovery could not be used to further constrain the estimated number density of ISOs beyond that of Do et al. (2018).

Jewitt and Luu (2019), Guzik et al. (2020), de León et al. (2019), McKay et al. (2020), Cremonese et al. (2020), Kim et al. (2020), Fitzsimmons et al. (2019), and Xing et al. (2020) observationally characterised 2I/Borisov and found it to be similar to Solar System comets, with typical dust production rates and detections of OH, CN and atomic oxygen. de León et al. (2020) and Opitom et al. (2019) found non-detections in C_2 in September and October 2019 and suggested 2I to be carbon-chain depleted with implications for its formation (Cochran et al. 2020), but in observations taken shortly before perihelion in late November Bannister et al. (2020) detected C_2, demonstrating instead an evolving C_2 production rate. Using observations from HST and the (at the time) non-detection of non-gravitational acceleration Jewitt et al. (2020b) constrained the nucleus diameter to 0.4 km–1 km. This was later complemented by Hui et al. (2020) who detected non-gravitational acceleration using pre- and post- perihelion observations and constrained its nuclear diameter to less than 0.8 km. Using pre-discovery images as far back as December 2018, Ye et al. (2020) inferred 2I became active at a heliocentric distance of ~ 8 au, implying its activity was triggered by the sublimation of hypervolatiles such as CO or CO_2 rather than H_2O. With pre-discovery images and new data Bolin et al. (2020) measured 2I's brightness trend, demonstrating the onset of water sublimation and estimating a nuclear diameter less than 1.4 km. Bagnulo et al. (2021) measured unusually high polarisation of light scattered from its coma, which they argue means 2I to be highly pristine. Jewitt et al. (2020a) observe an outburst and brief 'double nucleus', which they deduced was caused by the ejection and rotational destruction of a metre-scale chunk by outgassing. They conclude main nucleus

will survive the rest of its Solar System passage. The main significant difference between 2I and other Solar System comets, other than its hyperbolic orbit, is that it was highly enriched in CO relative to H_2O (Bodewits et al. (2020) with HST; Cordiner et al. (2020) with ALMA), and thus probably formed beyond its parent star's CO iceline (Seligman et al. 2022).

1.4 No Others

At the time of the submission of this thesis, no other ISOs have been discovered. Though hyperbolic Solar System comets have occasionally been suggested to have interstellar origins, they are generally considered to have Solar System origins (Whipple 1975). Some Solar System objects have been suggested to be captured ISOs, with Dehnen et al. (2022) calculating a steady state population of ~ 8 ISOs within 5 au of the Sun temporarily bound the the Solar System at any given time. These ISOs are however not necessarily easy to find (recall 1I was only discovered at a geocentric distance of ~ 0.2 au) nor characterise as once-interstellar. Forbes and Loeb (2019) find that ISOs impact the Sun at a rate of approximately once every thirty years, and concludes that statistically one of the sungrazing comets we have observed may have been interstellar in origin, though we cannot tell which one. The next ISO to be discovered, 3I, will likely be found by the LSST starting later this year, as discussed in Chapter 4.

The prospect of interstellar meteor detection has been long-standing for many decades and the discovery of one would be highly interesting (Gregg and Wiegert 2025). Despite claims to the contrary (Siraj and Loeb 2019b) I rely on the assessments of Vaubaillon (2022), Brown and Borovička (2023), Desch and Jackson (2023), Gallardo (2023, 2024), Desch (2024), and Fernando et al. (2024) that no interstellar meteors have yet been discovered.

1.5 State of the Field

1.5.1 The Galactic Context

If you wish to make a Galactic ISO population from scratch, you must first invent the Galaxy. The Milky Way is a barred spiral galaxy: a disk of stars, gas, dust, stellar remnants and ISOs, embedded in a roughly-spherical halo of globular clusters and dark matter (Posti and Helmi 2019).

Since starlight is the principal medium by which we can study the Universe, the study of stars is important in astronomy. Stars have a number of properties which affect their evolution and the light they produce, the most important of which for this thesis are mass, composition and age. Stars are classified spectroscopically into types (Maury and Pickering 1897; Cannon and Pickering 1901) which correlate with surface temperature.[7] Intrinsic luminosities of stars can be calculated from their apparent magnitudes, estimated dust extinction and distance: In the Milky Way, distances can be measured using parallax or the method of Leavitt and Pickering (1912), who discovered a relationship between the absolute magnitudes of Cepheid variable stars and their periods. The mass of a star can be computed from its luminosity and spectral type by an empirical relation (Kuiper 1938) fit to components of stellar binaries with observable periods, which can be related to their masses by Kepler's third law. A star's mass, luminosity and distance can also be inferred from effects in its spectrum such as pressure broadening of lines, allowing purely spectrum-based methods such as that of Leung and Bovy (2019b).

The absorption lines that the chemical elements introduce into a star's spectrum can be used to measure their abundances in the star's atmosphere with methods such as that of Payne-Gaposchkin (1925). She correctly demonstrated that the compositions of stars was dominated by hydrogen and helium, leaving heavier elements (metals) as a small minority. Alternatively, a star's metallicity can be estimated from its colours relative to other stars of the same spectral type, for example the ultraviolet excess caused by weak metal absorption line discovered

[7] *Oh But An F-Grade Kills Me* is this academically-anxious candidate's preferred acronym to remember the Harvard system types in order of descending temperature.

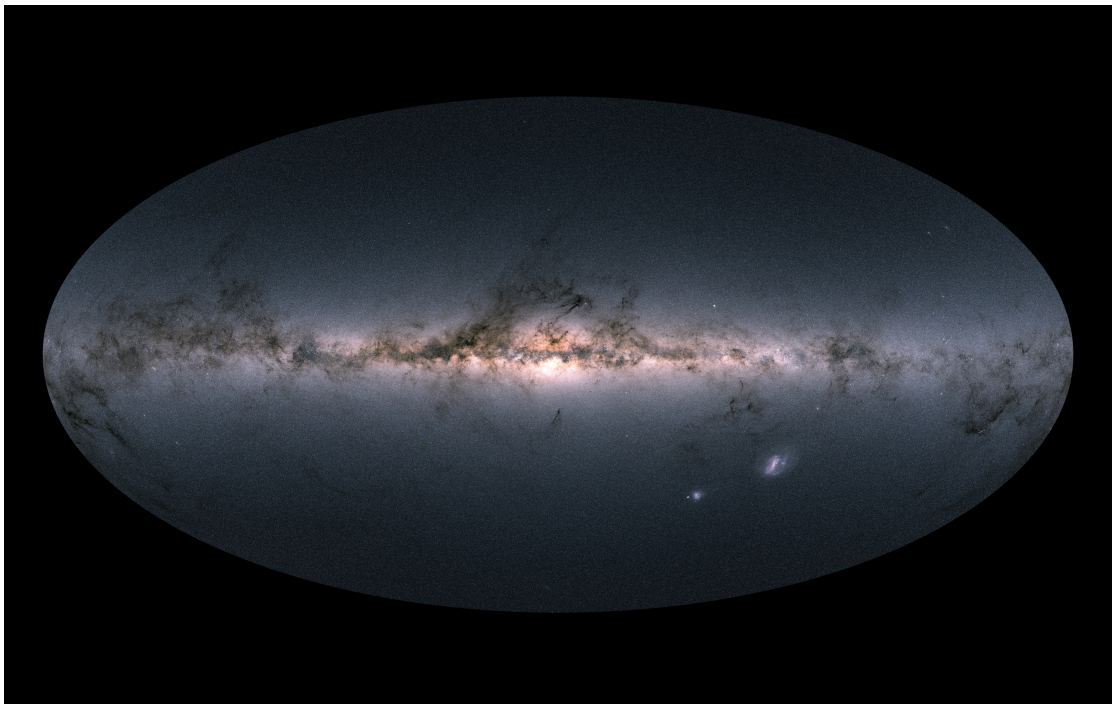

Figure 1.4: *Gaia*'s all-sky view of the Milky Way, with the Galactic centre in the middle, the Large and Small Magellanic to the lower right, and large foreground obscuring interstellar clouds along the Galactic plane.
Credit: ESA/Gaia/DPAC

by Roman (1954). Measuring the ages of stars is made difficult by the stability and lack of change stars experience over the majority of their lives on the main sequence, however methods do exist: Asteroseismology relates minute- to hour-timescale photometric and spectroscopic variations in stars to their evolutionary state (Lebreton and Montalbán 2009), and gyrochronometry relates a star's age to its rotation period, measured from its light curve, which increases with age due to magnetic braking (Weber and Davis 1967; Angus et al. 2015).

Over the 20$^{\text{th}}$ century the layout of the Milky Way was mapped. This effort was and remains to this day significantly more difficult than studying the structure of external galaxies, due to obscuration of large parts of the Galaxy by interstellar clouds (see Fig. 1.4). Oort (1927) cleverly demonstrated that the pattern of velocities of stars near the Sun demonstrated that they lay on approximately-circular orbits about a centre, supposed to be in the direction of the constellation of Sagittarius, from which he estimated the Sun to be offset by $\sim 6\,\text{kpc}$. Using Leavitt and

Pickering (1912)'s method, Shapley (1939) and Baade (1946) used Cepheid variables along sight-lines through the Galactic bulge to measure the distance to Galactic centre to be $\sim 10\,\mathrm{kpc}$.[8] Reber (1944) first detected the Milky Way's spiral arms, deducing them to be the cause of maxima in his radio observations, and they were mapped in the pattern of nearby H II regions (Morgan et al. 1952), then in aggregates of O-, B-, and A-type stars (Morgan et al. 1953), and then again in neutral hydrogen gas traced by the 21 cm hydrogen line (van de Hulst et al. 1954). The Galactic bar, first suggested to exist by de Vaucouleurs (1964), was confirmed by Stanek et al. (1994) in microlensing events towards the Galactic centre. Completing the modern list of components to our Galaxy, Gilmore and Reid (1983) found in addition to the thin disk of stars which dominates the Solar neighbourhood there existed a low-metallicity 'thick disk' of scale height $\sim 1350\,\mathrm{pc}$.

The metals in the Galaxy are not primordial: big bang nucleosynthesis produced almost exclusively hydrogen and helium (Walker et al. 1991; Schramm and Turner 1998), leaving the metals to be produced later, largely in the cores of stars (Maeder 1992) and supernovae (Nomoto et al. 1984; Iwamoto et al. 1999). These production mechanisms cause the Galaxy to chemically evolve over time (Tinsley 1980), a process first modelled by Schmidt (1963). Chemical evolution models have developed in complexity since then, in step with increased knowledge of the stellar population (Matteucci 2021), brought about by modern large-scale Galactic spectroscopic surveys such as GALAH (De Silva et al. 2015), APOGEE (Majewski et al. 2017) and *Gaia* (Gaia Collaboration et al. 2016). These modern surveys have revealed the stellar population to be highly complex with correlated chemical and dynamical[9] features described below:

Abundance gradients First measured in photometric metallicity studies by Janes and McClure (1972) and Grenon (1972), the abundances of multiple different metals decrease with radial distance from the Galactic centre at rates of $\sim 0.05\,\mathrm{dex\,kpc^{-1}}$

[8] Modern estimates of the Sun's Galactocentric distance using various techniques place us at $(8.2 \pm 0.1)\,\mathrm{kpc}$ (see Fig. 1 of Leung et al. 2023).

[9] or 'chemodynamical'

(Shaver et al. 1983). This is due to higher star formation rates in the inner parts of the Galaxy (Larson 1976), an 'inside-out formation' with the inner disk going through more stellar generations, each increasing the metallicity of the gas from which the next generation forms (Frankel et al. 2019).

Age-velocity dispersion relation In the Galactic disk most stars have largely circular orbits around the Galactic centre, but with some oscillation in Galactocentric radius and vertical height around the disk midplane, the amplitudes of which increase with age (Nordström et al. 2004). This age-velocity dispersion relation is explained by stars being born onto near-circular orbits (Frankel et al. 2020) and over time experiencing cumulative scatterings off giant molecular clouds (Gustafsson et al. 2016).

Flat age–metallicity relation Although the oldest stars in the Solar neighbourhood are the lowest in metallicity (Hearnshaw 1972; Powell 1972), over a wide range of ages the relation between stellar age and metallicity has a flat gradient and large scatter (Edvardsson et al. 1993). The feature was initially surprising, as it may be expected that the chemical evolution of the Galaxy would increase the metallicity of stars to increase over time, however it continues to be attested in many surveys of stars (Nordström et al. 2004; Haywood et al. 2013; Mackereth et al. 2017, e.g.) as well as surveys of white dwarfs (Rebassa-Mansergas et al. 2021). The solar neighbourhood's flat age-metallicity relation may be explained by radial migration (Schönrich and Binney 2009a), which is the change in the Galactocentric radii of stars on circular orbits near corotation with the spiral arms due to the torque they induce (Sellwood and Binney 2002; Kormendy and Kennicutt 2004), making the Solar neighbourhood stellar population a mix of inner and outer disk stars. This view however is not unanimous, with some such as Haywood et al. (2013) arguing that radial migration is not required to explain the distribution of stars in age, [Fe/H] and [α/Fe] that they observe.

The [α/Fe]–[Fe/H] **distribution** If the interstellar medium were enriched with different elements at the same rate, the relative abundance of those elements would be constant. This is not what is observed in stellar surveys such as Gratton et al. (1996). This is due to differences in the yields and timescales of different enrichment pathways (Wheeler et al. 1989): Core-collapse supernovae of massive stars contribute largely α-process elements (C, O, Ne, Mg, Si, and S) and, due to the short $\sim$ 10 Myr lifetimes of massive stars, rapidly enrich the interstellar medium after star formation occurs. Conversely, type Ia supernovae which occur on significantly longer timescales and contribute largely Fe (Nomoto et al. 1984). The bimodality in the [α/Fe]–[Fe/H] distribution was further connected to the kinematically-distinguished thin and thick disks (Bensby et al. 2003; Navarro et al. 2011), leading to two-phase formation models such as those of Chiappini et al. (1997) and Haywood et al. (2013) which explain the thick and thin disk as distinct stellar populations with a hiatus in star formation in-between. However, non-episodic models such as that of Schönrich and Binney (2009b) can also recreate the same dynamical and chemical features. Additionally in more recent studies such as Bovy et al. (2012b) and Mackereth et al. (2017, 2019), when the stellar population is divided into mono-abundance and mono-age subpopulations, the picture of a kinematically and chemically distinct thick disk disappears. Instead, these subpopulations show a roughly continuous transitions from low scale heights and high radial scale lengths to high scale heights and low radial scale lengths.

Observational exoplanet surveys (e.g. *Kepler*; Borucki et al. 2010; Petigura et al. 2013; Dressing and Charbonneau 2015) and discoveries of debris disks around stars such as β Pictoris (Smith and Terrile 1984; Ferlet et al. 1987) demonstrate that most stars have planetary systems, implying most stars also form planetesimals like the small bodies we see in the Solar System. Studies of exoplanets find strong positive correlations between the occurrence rates of exoplanets and host star metallicity (Santos et al. 2004; Fischer and Valenti 2005; Petigura et al. 2018), however this picture is highly complicated and uncertain. Different studies disagree

on the slopes of correlations (cf. Table 1 of Osborn and Bayliss 2020), different classes of exoplanets appear to have different strengths of correlations (Brewer et al. 2018), and different classes of exoplanets appear to different correlations with the abundances of different elements, particularly the α-process elements (Bashi and Zucker 2019; Wilson et al. 2022). However, in broad strokes, it is clear that more metals means more planetary material and thus both the Galactic planetary and ISO populations will evolve over time as the Galaxy chemically evolves.

1.5.2 The Life of an ISO

1.5.2.1 Formation and Ejection

As stars form in the collapsing cores of molecular clouds, gas and dust feeding onto the protostar forms a protoplanetary disk, where the formation of planetesimals and planets occur (Armitage 2024). Though other sources for 1I-like ISOs have been proposed (§1.2.3), it is generally accepted that these protoplanetary disks are the birthplaces of ISOs.

Protoplanetary disks in nearby star-forming regions can be studied at a range of wavelengths (e.g. at visible wavelengths with Hubble; O'Dell and Wong 1996) however they are most commonly studied at millimetre and infrared wavelengths with ALMA (Wootten and Thompson 2009; Ansdell et al. 2018; Cazzoletti et al. 2019) and JWST (Sturm et al. 2023) which are sensitive to molecular emission lines (Walsh et al. 2014). These studies show that disks have masses proportional to the masses of their central stars (Andrews et al. 2013), with sizes traced by CO gas in the range 100 au to 500 au (Trapman et al. 2020) but significantly more compact dust disks of < 30 au due to inward radial drift (Guerra-Alvarado et al. 2025). The disk gas is mostly evaporated from the inside by the UV radiation of the central star, giving gas disk lifetimes of ~ 10 Myr with a large scatter and decreasing with central star mass (Pfalzner and Dincer 2024). Since they form from the same dust and gas, a protoplanetary disk's composition is often assumed to be equal to that of its central star (e.g. Bitsch and Battistini 2020), but this is difficult to measure

and confirm due to the freezing-out of molecular species, removing them from the gas phase and detectability (Fedele and Favre 2020).

In the process of forming a planetary system, a lot of material is completely ejected. Giant planets are efficient at ejecting small bodies (Brasser et al. 2006) and do so as they migrate (Gomes et al. 2005; Tsiganis et al. 2005; Morbidelli et al. 2005). Some studies of the asteroid belt and Kuiper belt imply the primordial mass of each was much higher than their present day values (Petit et al. 2001; Stern 1995; Kenyon 2002), however more recent modelling of the asteroid belt in particular has demonstrated it may instead have begun as an empty region that was populated by gravitational scattering (Raymond and Izidoro 2017; Izidoro et al. 2022; Deienno et al. 2024).

Other mechanisms to remove small bodies from their birth planetary systems into the interstellar environment include stellar flybys (Pfalzner et al. 2021b), binary stellar systems (Fitzmaurice et al. 2022), and post-main-sequence mass loss at the end of their parent star's life (although this is expected to produce a minority of ISOs Hansen and Zuckerman 2017; Levine et al. 2023). Each of these mechanisms act at different evolutionary stages and at different distances from the planetry system's central star or stars, possibly producing different distributions in size, composition, and ejection velocity.

1.5.2.2 Galactic Wandering

Ejected from their parent planetary systems at relatively low velocities ($< 10\,\mathrm{km\,s^{-1}}$ Hands et al. 2019; Pfalzner et al. 2021b), ISOs orbit the Galactic centre much like stars do. However, these small velocity differences place ISOs onto slightly different near-circular Galactic orbits to their parent stars, causing them to rapidly drift azimuthally.[10] Instead of staying near their parent stars, ISOs form tidal streams (Portegies Zwart 2021; Forbes et al. 2024), much like those coming off stellar clusters in the Galactic halo (Bonaca and Price-Whelan 2025) or meteoroid streams off comets in the Solar system (Jenniskens 1998). Being as negligibly massless as

[10]This is very well demonstrated by the video showing the orbits of a selection of stars from the Gaia Catalogue of Nearby Stars at https://www.cosmos.esa.int/web/gaia/edr3-gcns

individual stars compared to the giant molecular clouds, bar and spiral arms which influence them, the orbits of ISOs evolve identically to those of their parent stars'.

Most ISOs are expected to survive indefinitely. While bombardment by dust in interstellar space has been suggested to erode and potentially destroy ISOs over time (Domokos et al. 2017; Vavilov and Medvedev 2019, cf.), Öpik–Oort cloud comets have occupied essentially the same interstellar environment for 4.5 Gyr without significant destruction (Stern 1989; Guilbert-Lepoutre et al. 2015). Thus the ISO population is expected to be as old as, if not older than, the stellar population because unlike ISOs, stars experience death.

This old age combined with the short timescale on which orbit uncertainties grow (only ~ 10 Myr, with a corresponding length scale of ~ 100 pc; Zuluaga et al. 2018; Zhang 2018) means that only the youngest $\sim 1\%$ of ISOs can be traced back to their parent star. This means finding the origins of both 1I and 2I are precluded by their dynamical age estimates (Almeida-Fernandes and Rocha-Pinto 2018a). However, the immense scientific potential represented by a link between an ISO under study and its parent system has inspired many to attempt backtracing both 1I and 2I anyway (Mamajek 2017; Gaidos 2018; Feng and Jones 2018; Portegies Zwart et al. 2018; Dybczyński and Królikowska 2018; Bailer-Jones et al. 2018; Dybczyński et al. 2019; Bailer-Jones et al. 2020; Hallatt and Wiegert 2020; Hsieh et al. 2021). As expected, none of these papers find any convincing parent star candidates when read critically. This further makes sense when the timescale for close scattering is considered: an object with a speed of $50\,\mathrm{km\,s^{-1}}$ only undergoes a < 5 au-separation encounter with a star (of number density $0.1\,\mathrm{pc^{-3}}$) after on average 10^5 Gyr. The vast majority of ISOs we observe in the inner Solar system will not have had a close stellar encounter since they left their birth planetary systems.

1.5.2.3 Detection in Solar System

To be detected, ISOs must enter the Solar System. They do so on strongly hyperbolic orbits which, when discovered, clearly distinguish them from bound Solar System objects. The deflection of their trajectories by the Sun's gravity increases their

frequency in the inner Solar System, a process called gravitational focussing (Whipple 1975). Some approach the Sun and Earth sufficiently closely that the sunlight they reflect reaches a detectable magnitude, allowing them to be discovered by surveys.

Unlike in other disciplines of astronomy, in the Solar System objects move rapidly across the sky. To discover an object in the Solar System, a survey must therefore return to the same patch of sky and re-detect the object several times (a minimum of three; Gauss 1809), correctly link the detections as belonging to the same object and fit an orbit to them so the object can be found again later. This makes survey detection efficiency dependent on cadence, and makes estimation complex. Several works have predicted the number of ISOs expected to be observed by LSST to be ~ 10, with an order-of-magnitude level of uncertainty (Levine et al. 2021; Hoover et al. 2022; Marčeta and Seligman 2023), including Dorsey et al. (2025) to which I contributed the work of Chapter 4; see that chapter for a more in-depth discussion of ISO discovery in surveys. The number of anticipated ISO discoveries in LSST is uncertain due to both the size distribution and underlying number density of ISOs being undermined.

Most ISOs pass straight through the Solar system, having potentially undergone some processing from solar heating (Jewitt et al. 2020a), and rejoin the Galactic population.

1.5.3 ISOs as a Galactic Population

As the field develops, the study of ISOs is beginning to move on from just the characterisation of those we have found and the prediction of those we will find in the future. At a density of $\sim 0.1\,\mathrm{au}^{-3}$, ISOs are omnipresent, filling every corner of the Galaxy as part of the interstellar medium, participating in Galactic life and interacting with other Galactic populations by simple virtue of always being there.[11]

In a framework developed by Grishin et al. (2019), Pfalzner and Bannister (2019), Pfalzner et al. (2020, 2021a), and Moro-Martín and Norman (2022), ISOs present in molecular clouds follow their collapse and thus are present in protoplanetary

[11] To adapt a common myth about rats in cities, 'You're never more than 10^{12} ft away from an ISO!'

disks. Here they may act as seeds for rapid planet formation by providing accretion sites, clearing barriers to efficient growth.

Jennings et al. (2020) explore the gravitational interaction of ISOs with pulsars. They find that the a Ceres-mass ($10^{-4} M_{\oplus}$) ISO flyby at 1 au of a millisecond pulsar would introduce a detectable change in the pulse timing. With pulsar timing arrays such as NANOGrav (McLaughlin 2013), this presents the opportunity to detect and characterise the high end of the ISO mass distribution, as well as explore the spatial distribution of ISOs through the Galaxy, outside of the Solar neighbourhood.

Following the work of Belbruno et al. (2012) who explore the exchange of life-bearing material between planetary systems within an embedded star cluster and inspired by the discovery of 1I/'Oumaumua, Ginsburg et al. (2018) explored the possibility that panspermia, the transfer and seeding of life from one planet to another by material ejected in collisions, occurs on a Galactic scale, mediated by ISOs. Desch and Jackson (2022) argue that their N_2 ice fragment hypothesis for 1I represents a more feasible pathway to Galactic panspermia than a rocky asteroidal body, however both Cao et al. (2024) and Kipping (2025) find it extremely unlikely life on Earth, the only place life is known to exist, was seeded from the small number of ISO collisions which can have occurred before life is known to have emerged.

Finally, Lintott et al. (2022) link the composition distribution of ISOs in simulated galaxies to their star-formation histories. This work was the genesis of the main project of this thesis (Chapters 2–4). If the properties of the Galactic ISO population can be linked to properties of the wider Galaxy (its star formation history, dynamics, planetary architectures, etc.), characterised ISOs discovered in the inner Solar System can be used to make inferences about these properties of the wider Galaxy with an entirely different set of biases to traditional observational methods of studying them. In the next section I briefly describe how these inferences may be carried out.

1.6 A Note on Statistics

As hinted in footnote 6, throughout this thesis I take a Bayesian approach. This is grounded in the theorem of Bayes and Price (1763), that the posterior probability

of a hypothesis being true given some observed data $p(H_i \mid D)$ is proportional to both the likelihood of that data being observed assuming the hypothesis $p(D \mid H_i)$ and the prior probability of that hypothesis being true, based on empirical but external context. Formalised, the posterior probability is given by

$$p(H_i \mid D) = \frac{p(D \mid H_i)p(H_i)}{p(D)} = \frac{p(D \mid H_i)p(H_i)}{\sum_j p(D \mid H_j)p(H_j)} \tag{1.1}$$

where the final equality can be taken when all hypotheses H_j partition possibility space (i.e. one hypothesis is correct, but only one; they are mutually exclusive).

In fields where data is plentiful, sufficient data can be gathered until all but one[12] hypotheses can be rejected in a frequentist manner. This is most commonly done with the method of p values: assume a given hypothesis true, take data D, calculate the probability p , This can be thought of as limit of Bayesian with p as likelihood, with a small number of hypotheses, none of which deemed to have a negligible prior probability. Here gathering sufficient data to reject all but one means that the likelihood dominates shape of posterior distribution over hypotheses by determining all but one of them to be of negligible posterior. If after doing the analysis more than one hypothesis remains unrejected, or other hypotheses are proposed, gather more data.

Bayesian statistics comes with a different philosophy: we have a limited and fixed amount of data, and we wish to know what can be inferred from it. This is useful in the many low-data fields of astronomy, where our access to data is limited by the fact that there is only one sky and one Universe, and re-running the experiment takes 13.8 Gyr (Planck Collaboration et al. 2020).[13]

Over the course of this thesis I predict various distributions of ISOs that I expect to be observed. These predictions are made with the intention that they be compared to an observed sample of ISOs in order to make inferences about the models which went into producing them. This observed sample will likely be small, so here I describe how to do this in a Bayesian manner.

[12] or none, as 'all models are wrong' (Box 1976), but ideally one model always remains clearly more useful than the others.

[13] And just the first run has made a lot of people very angry and been widely regarded as a bad move (Adams 1980).

$f(x \mid \theta)$ may describe the predicted distribution of observable ISOs, including any observation biases, in any set of observable properties x, for example velocity, composition and age, with any set of model parameters θ, for example the metallicity dependence of ISO production tested in Chapter 2 or a choice of velocity distribution model such as those compared in §3.4.3. When normalised to 1, $f(x \mid \theta)$ is also the probability distribution for a randomly drawn ISO having the properties with a set of values x given the model parameters θ, so $p(x \mid \theta) = f(x \mid \theta)$. As the properties of ISOs entering Solar System are independent[14] , the probability of a sample of N ISOs having properties $x_1, \ldots, x_N$ is

$$p(x_1, \ldots, x_N \mid \theta) = \prod_i^N p(x_i \mid \theta) \tag{1.2}$$

In the language of Bayes' theorem, this is the likelihood of observing the N ISOs to have properties $x_1, \ldots, x_N$. This can be used in likelihood ratio tests to compare models, as in Chapter 3, where the distribution is the ISO velocity distribution and θ simply specifies the choice of velocity distribution model. In that section, using these functions I calculate what sample sizes of ISOs are required to generate likelihood ratios significantly different from unity, which would allow the velocity distributions models to be distinguished.

The ISO sample likelihood of Eq. 1.2 can be combined with priors on θ to form a posterior distribution on the model parameters:

$$p(\theta \mid x_1, \ldots, x_N) \propto p(\theta) \cdot \prod_i^N p(x_1, \ldots, x_N \mid \theta) \tag{1.3}$$

This posterior can be used to calculate estimates and confidence intervals for the values of the parameters θ. An example of this calculation is given in Chapter 2 to estimate the metallicity dependence of the number of ISOs produced by each star using the sample of known ISO compositions (i.e. only that of 2I/Borisov).

[14]This holds while the observation of one ISO does not affect the probability distribution of properties that may be observed in another. This will break down if surveys adapt their observing strategy in response to ISO discoveries as they happen. Alternatively if ISOs enter the Solar System as binaries, a possibility discussed in §5.4, their properties will not be independent.

1.7 Outline of Thesis

Over the last 75 years, the Galactic population of ISOs has been predicted by Oort (1950), calculated to be unobservably rarefied by Moro-Martín et al. (2009), discovered to have asteroidal members such as 1I which was unlike any object ever seen, then discovered to have cometary members such as 2I, which strongly matched the 1950s expectation for an ISO.

In just a few months the LSST survey will begin, which over the next ten years will increase the number of discovered ISOs by an order of magnitude, giving us a sample large enough and sufficiently well-characterised to being making confident inferences about the population. These ISOs will come to us from distant and possibly long-dead planetary systems, across the Galaxy and cosmic timespans stretching to well before the formation of our own Solar system. Tapping the vast wealth of information this Galactic ISO population contains requires understanding its Galactic context.

In this thesis I describe my work to predict the properties of the population of ISOs that the LSST will observe. In Chapter 2 I fit a model of the Milky Way to data from the APOGEE survey then combine this with a protoplanetary disk chemical model to predict the distribution of compositions of ISOs across the Milky Way disk (Hopkins et al. 2023). In Chapter 3 I debias data from the *Gaia* survey to estimate the chemodynamics of the solar neighbourhood stellar population, then from this predict the chemodynamical distribution of ISOs passing through the inner Solar System (Hopkins et al. 2025a). In Chapter 4 I describe the work I contributed to Dorsey et al. (2025): a novel and efficient method of sampling the distribution of orbits ISOs enter the Solar System on, for use in an LSST survey simulator. I also describe the results of Dorsey et al. (2025), including how the underlying size distribution affects the observed size distribution and the number of ISOs expected to be discovered. This work will allow the size distribution and number density of ISOs to be estimated incrementally from the LSST sample as they are discovered.

In Chapter 5 I describe my contributions to Pham et al. (2024), a study hypothesising that collisions between ISOs and neutron stars as a feasible source of

fast radio bursts (FRBs). I demonstrate that the expected observable rate of such collisions matches both the observed FRB rate and its trend with redshift, discuss possible correlations with host galaxy morphology, and compare the predictions of this hypothesis to other suggested sources of FRBs. Finally in Chapter 6 I use my model of the Milky Way from Chapter 2, which includes dead stars, to predict the distribution of black holes in the Galaxy.

The predictions of this thesis shall be compared to data from the LSST and other discoveries over the next few years and decades, and being privileged to live in a world of science with an ever-moving frontier, I look forward to finding out in what fascinating, informative and possibly downright unpredictable ways I am proven to be wrong.

Though here at journey's end I lie
in darkness buried deep,
beyond all towers strong and high,
beyond all mountains steep,
above all shadows rides the Sun
and Stars forever dwell:*
I will not say the Day is done,
nor bid the Stars farewell.

— Samwise Gamgee, *The Lord of the Rings*

2

Modelling the Galactic ISO Population with APOGEE

The work described in this chapter constitutes that published in Hopkins et al. (2023), the entirety of which I led.

2.1 Introduction

ISOs formed in a protoplanetary disk carry information about their home systems in their composition. The composition of a protoplanetary disk correlates with the elemental abundances of its central star, due to their formation from the same gas and dust in a molecular cloud core (Öberg and Bergin 2021). One can thus expect stars of different metallicities to produce ISOs of different compositions. The composition of this material varies with both time and position in the Galaxy as the Milky Way chemically evolves due to stellar nucleosynthesis, making the current Galactic ISO population sensitive to the entire history and evolution of the Milky Way over cosmic time (Lintott et al. 2022). Since the occurrence of planetesimal-scattering giant planets also has a metallicity dependence (Fischer and Valenti 2005), the relative occurrence of ISOs of different compositions will therefore carry information about the Galaxy's distribution of planetary architectures.

*incorrect, see Section 2.2.3.

In this chapter I develop predictions of this distribution of ISO compositions through a large swath of the Milky Way, including in the Solar neighbourhood. I do this using a model of the Galactic stellar population which I fit to data from the APOGEE red giant survey (Majewski et al. 2017), accounting for the survey selection function and interstellar dust extinction, described in Section 2.2. I then combine this model of the stellar population with a protoplanetary disk chemical model and assumptions of Galactic dynamics to predict the ISO population of the Galaxy, described in Section 2.3.

The results of this I describe in Section 2.4, where I detail predictions of the ISO water mass fraction distribution for ISOs in the Solar neighbourhood and in the wider Galactic population, for a principal and alternate assumption about the metallicity dependence of ISO production. Finally in Section 2.5 I discuss the possibility of using the measured composition distribution of ISOs to measure the radial mixing of ISOs relative to stars, and demonstrate the inference framework by using the measured composition of 2I to constrain the ISO production metallicity dependence.

2.2 APOGEE and Stellar Density Modelling

To predict the distribution of ISOs in the Milky Way, I first obtain the distribution of all stars throughout Galactic history over a large swath of the Galactic disk, which I model by fitting simple density profiles to debiased data from the APOGEE survey. While APOGEE's main sample is not representative of all extant stars, I can extrapolate from it to recover the total stellar population of the Milky Way. By design, the APOGEE main sample mainly contains red giants: stars in a relatively short-lived phase towards the end of their lives. Since each stellar generation forms stars with a range of masses (Chabrier 2003) and a corresponding range of lifespans, all but the newest stellar populations will have some stars currently in the red giant stage. This means multiple generations are represented in the APOGEE sample. I then extrapolate to the entire stellar population. This reconstruction is detailed in 2.2.3.

2.2.1 Observational Data: APOGEE

I use data from the APOGEE SDSS-IV Data Release 16 (Jönsson et al. 2020). APOGEE is a near-infrared, high-resolution ($R \sim 22\,500$) spectroscopic stellar survey used to estimate high-precision chemical abundances for a sample of over 200 000 Milky Way stars (Majewski et al. 2017). The survey's simple and well-characterised selection function, which randomly selects specified fractions of stars in different intervals of apparent magnitude and dereddened colour, is optimised to select red giants (Zasowski et al. 2013, 2017). As infrared bands suffer less from dust extinction than optical, the red giants selected are visible across the Galactic disk. The high-precision abundance measurements mean that I can identify monoabundance populations with very low levels of contamination by binning the APOGEE stars in [Fe/H] and [α/Fe] (Bovy et al. 2016b). Additionally, the well-characterised nature of the selection function means that it can easily be accounted for using the method of Bovy et al. (2016a), which I detail in the next section. This makes APOGEE an ideal choice for modelling the spatial and chemical distribution of the Milky Way's red giant population.

I obtain the chemical abundances, heliocentric distance and age of stars in APOGEE DR16. To obtain each star's abundances, I use the calibrated ASPCAP pipeline's (García Pérez et al. 2016) abundances of iron [Fe/H] and alpha elements [α/Fe], calculated from an average of the abundances of the elements O, Mg, Si, S, and Ca, after Bovy et al. (2016b). For each star's heliocentric distance and age, I use the `weighted_dist` and `age_lowess_correct` estimates, both of which use neural networks based on `AstroNN` (Leung and Bovy 2019a). `weighted_dist`, detailed in Leung and Bovy (2019b), is an inverse-variance weighted average of the distance estimate from the *Gaia* parallax measurement of the star (Gaia Collaboration et al. 2016) and a spectro-photometric distance estimate of the star from a neural network trained on 265 761 stars surveyed in common between APOGEE DR14 (Abolfathi et al. 2018; Holtzman et al. 2018) and *Gaia* DR2 (Gaia Collaboration et al. 2018). This results in a distance estimate more accurate than from parallax alone, which has large relative uncertainties for distant stars. `age_lowess_correct`, described in

Mackereth et al. (2019), is a measurement of the stellar age from a neural network trained on 6676 stars with both spectroscopic measurement by APOGEE DR14 and asteroseismic age measurement by the *Kepler* mission (Borucki et al. 2010), corrected for biases from the neural network with a LOWESS[1] fit (Savitzky and Golay 1964) to the $\mathrm{age_{out}}$–$\mathrm{age_{in}}$ relation. The age of a red giant can be estimated from its spectrum due to a causal relationship between their surface carbon and nitrogen abundances post first dredge-up and its main-sequence mass (Salaris et al. 2015; Martig et al. 2016), which defines the age range the star will be occupy the red giant stage. Due to a lack of stars with low metallicity in the training data, reliable ages aren't available for stars with $[\mathrm{Fe/H}] < -0.5$, so for these stars I must assume an age distribution, described in Sections 2.2.2 and 2.2.3.

The APOGEE DR16 "statistical sample" (the sample of stars for which the selection function can be reconstructed) contains 165,768 stars. However, this is partly made up of dwarfs, which have higher uncertainties in their atmospheric parameters and abundances. I therefore select for red giants with a subset of the statistical sample with a calibrated ASPCAP surface gravity of $1 \leq \log g < 3$. I additionally select only stars with fractional uncertainty in heliocentric distance D of less than 0.5. To restrict my sample to the Milky Way's disk, as opposed to the bulge or halo, I select stars with Galactocentric radii R between 4 kpc and 12 kpc and height above the disk z of -5 kpc to 5 kpc. This gives us a sample of 80 958 red giants.

2.2.2 Density Modelling of Red Giants across the Galaxy

To calculate the distribution of red giant stars in the Milky Way from the APOGEE data I use the method of Bovy et al. (2016a), as this accounts for both dust and the survey selection function simultaneously. In brief, assuming the stars observed in a survey are distributed independently in a space of some observables O (for example position, colour and magnitude, chemical abundances), then the positions of N stars in the space of observables $O_1, \ldots, O_N$ is a realization of a Poisson point process. A Poisson point process is a random distribution of points defined by a rate function

[1] LOcally WEighted Scatterplot Smoothing

$\lambda(O)$, such that the number of points in a given volume V in the space of the observables is a Poisson random variable with mean and variance equal to the integral of the rate function over that volume, $\int_V \lambda(O)\,\mathrm{d}O$. It follows that the probability of finding a point (i.e. an observed star) with observables in the infinitesimal volume δO is given by $\lambda(O)\,\delta O$, and the total number of points (i.e. stars observed) is a Poisson random variable with mean and variance $\Lambda = \int_V \lambda(O)\,\mathrm{d}O$. Since the rate function is equal to the rate of occurrence of observed stars, it can account for both the underlying true density of stars, as well as the effect of the survey selection function and dust which prevent all extant stars from being observed. If the rate function is modelled with $\lambda(O \mid \theta)$, where θ parametrises the model, then the likelihood of the model given N observed stars $O_1, \ldots, O_N$ is given by

$$\ln \mathcal{L}(\theta) = \sum_i \ln \lambda(O_i \mid \theta) - \int_V \lambda(O \mid \theta)\,\mathrm{d}O\,. \tag{2.1}$$

APOGEE has a selection function based on bins in dereddened colour and apparent magnitude, so Bovy et al. (2016a) define the effective selection function $\mathfrak{S}(\mathrm{field}, D)$, a convenient quantity equal to the fraction of a population's stars at each heliocentric distance D that will be spectroscopically observed in each of APOGEE's fields. This is calculated for each field by simulating a tracer sample of stars in the field at that distance, and calculating the fraction that would be observed, given a dust map and the survey selection function in dereddened colour and apparent magnitude. I evaluate this for each monoabundance population in each field at a range of heliocentric distances D and ages τ. This allows us to treat stars as only having three observables: the field they appear in, their distance from the Sun D, and their age τ. I used the effective selection function implementation in the `apogee`[2] package (Bovy 2016; Bovy et al. 2016a). I obtained the tracer population by sampling PARSEC stellar model isochrones (Bressan et al. 2012; Marigo et al. 2017) at a range of ages with a Kroupa initial mass function with a minimum mass of $0.08 M_\odot$ (Kroupa 2001), cut to $1 \leq \log g < 3$ to match the APOGEE red giant sample to which it was being fit. For a dust map I used a

[2] https://github.com/jobovy/apogee

combination of Drimmel et al. (2003), Marshall et al. (2006) and Green et al. (2019), combined with the package `mwdust`[3] (Bovy et al. 2016a).

Following Bovy et al. (2016b), I separate the red giant sample into monoabundance populations by binning the stars in [Fe/H] and [α/Fe], then fit a separate number density model n_{giants} to each monoabundance population. The density model I chose to fit to each monoabundance population was a simple axisymmetric exponential in Galactocentric radius R and height above the plane of the disk z,

$$n_{\text{giants}}(R, z \mid \text{logA}, a_R, a_z) = \exp(\text{logA} - a_R(R - R_0) - a_z|z|)\,\text{kpc}^{-3}\,, \tag{2.2}$$

parameterised by an amplitude logA and two scale parameters a_R and a_z. $R_0 = 8.1\,\text{kpc}$ is the radial distance of the Sun from the Galactic centre (GRAVITY Collaboration et al. 2018)[4]. For each star I calculate R and z from the angular coordinates of the field pointing and distance from the Sun using the Astropy coordinates package (Astropy Collaboration et al. 2013, 2018, 2022). Whereas Bovy et al. (2016b) fit only the spatial distribution of each MAP using red clump stars, which act as standard candles with no age dependence to their color and luminosity, I expand on their method to simultaneously fit the age distribution of each MAP of my red giant sample. I assumed each the age distribution of each MAP to be a normal distribution with mean τ_0 and variance $1/\omega$,

$$g(\tau \mid \tau_0, \omega) = \sqrt{\frac{\omega}{2\pi}} \exp\left(-\frac{\omega}{2}(\tau - \tau_0)^2\right)\,, \tag{2.3}$$

a form justified as monoabundance populations have relatively narrow distributions in age (Lian et al. 2022b).

To calculate the rate function $\lambda(\text{field}, D, \tau)$ for each monoabundance population, the number density of red giants needs to be multiplied a Jacobian factor $|J(\text{field}, D)| = \Omega_{\text{field}} D^2$ to convert it from a 3-D density in Cartesian coordinates to a 1-D density in D. Multiplying by the age distribution gives the combined

[3] https://github.com/jobovy/mwdust

[4] Since I carried out the work of this chapter, Leung et al. (2023) was published which includes a comparison of many measurements of R_0, placing its value at $(8.2 \pm 0.1)\,\text{kpc}$. This discrepancy does not significantly affect the results of this chapter.

underlying distribution in field, distance D and age τ. The observed distribution is then found by multiplying this underlying distribution by the effective selection function $\mathfrak{S}(\text{field}, D, \tau)$. Thus the rate function for each monoabundance population is given by

$$\begin{aligned}\lambda(\text{field}, D, \tau \mid \text{logA}, a_R, a_z, \tau_0, \omega) = n_{\text{giants}}(R, z \mid \text{logA}, a_R, a_z) \cdot g(\tau \mid \tau_0, \omega) \\ \cdot |J(\text{field}, D)| \cdot \mathfrak{S}(\text{field}, D, \tau)\,.\end{aligned} \tag{2.4}$$

This particular form for the density profile has the advantage that the Poisson point process likelihood takes the tractable form

$$\begin{aligned}\ln \mathcal{L}(\text{logA}, a_R, a_z, \tau_0, \omega) = \text{const} + N\Big(\text{logA} - a_R\langle R - R_0\rangle - a_z\langle|z|\rangle \\ + \frac{\ln\omega}{2} - \frac{\omega}{2}\left(\langle\tau^2\rangle - 2\tau_0\langle\tau\rangle + \tau_0^2\right)\Big) \\ - \sum_{\text{field}} \int\int \lambda(\text{field}, D \mid \text{logA}, a_R, a_z, \tau_0, \omega)\,\mathrm{d}D\,\mathrm{d}\tau\,,\end{aligned} \tag{2.5}$$

where the sum over every star in the monoabundance population in Eq. 2.1 is reduced to a linear combination of the parameters with aggregates of the data in the monoabundance population being fitted: N as the number of stars observed, $\langle R\rangle$ and $\langle|z|\rangle$ as the mean coordinate values, and $\langle\tau\rangle$ and $\langle\tau^2\rangle$ as the mean age and age squared. To build my model of the Milky Way disk between $R = 4\,\text{kpc} - 12\,\text{kpc}$ and $|z| = 0 - 5\,\text{kpc}$, I found a best-fit model for each monoabundance population by maximising this likelihood with respect to logA, a_R, a_z, τ_0, and ω, visually checking each fit to ensure the global maximum had been found. The best-fit values for each monoabundance population are plotted in Figure 2.1.

Reliable `age_lowess_correct` estimates are not available for stars with [Fe/H] < -0.5, so for these monoabundance populations I fit only for logA, a_R and a_z. I use an effective selection function dependent only on field and D, calculated assuming a uniform age distribution. While a uniform age distribution is an inaccurate description of a monoabundance population, it is a non-informative assumption that ensures that the effective selection function is never zero where a star may actually be observed. On testing, I found that the effective selection function did not vary strongly with the age distribution assumed. Even then, as discussed

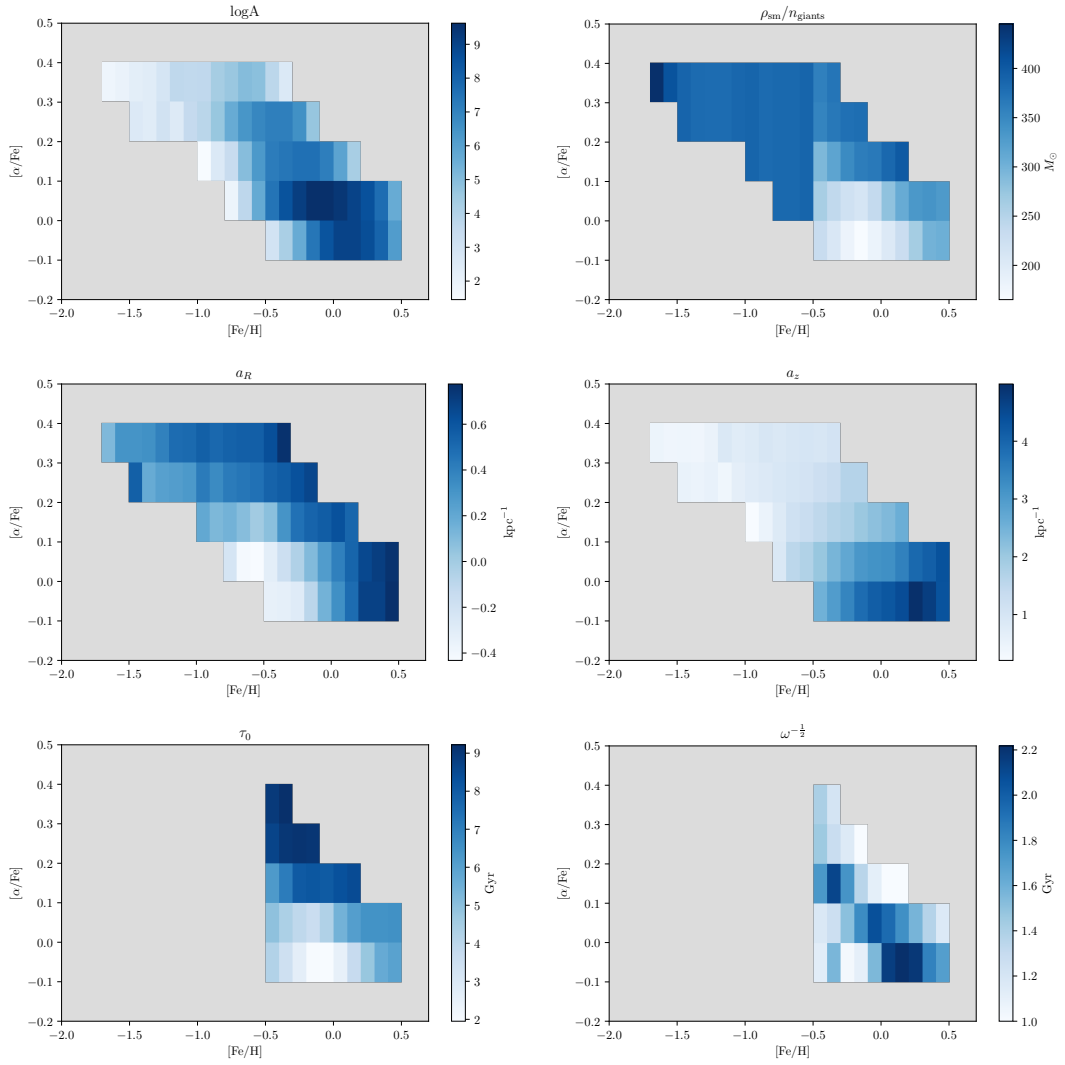

Figure 2.1: The best-fit values of the density modelling parameters for each monoabundance population with 20 or more observed stars, and $\rho_{\rm sm}/n_{\rm giants}$, the ratio between the *sine morte* stellar mass density and the red giant number density, explained in section 2.2.3.

in the section below, in my model stars with metallicity [Fe/H] < -0.5 do not contribute a significant number of ISOs, making my conclusions independent of the age distribution assumed for these stars.

The two main distinct chemodynamical populations of the Milky Way are clearly shown in my model (Fig. 2.1): The young, high [Fe/H], low [α/Fe] monoabundance populations have the low vertical scale lengths and high radial scale lengths which form the thin disk, whereas the old low [Fe/H], high [α/Fe] monoabundance populations have the opposite trend in scale lengths, forming the thick

disk (Mashonkina et al. 2019).

This approach gives us simple but accurate models of the trends of the Milky Way disk's stellar population in this range of R. These results agree with the results of Bovy et al. (2016b) which also models monoabundance populations in APOGEE, fitting more complex models to only stars in the red clump, using their highly consistent absolute magnitudes as an accurate distance measurement.

2.2.3 The *Sine Morte* Stellar Population

Having obtained a model for the distribution of red giants in the Milky Way, I then infer the distribution of all stars throughout Galactic history. As described later in Section 2.3.2, I assume the majority of ISOs form at the start of their parent star's life and then outlive their parent star. Under this constraint, the population of currently living stars is too limited to use to predict the ISO population. Instead, one must consider what the stellar population would be at the present time if stars did not die, but instead continued to orbit around the Milky Way indefinitely while being subjected to the same dynamical effects that affected both their longer-lived companion stars and the ISOs which they had released onto similar orbits. I introduce this as the *sine morte*[5] stellar population.

First, I calculate the *sine morte* number density of stars in each monoabundance population, from the red giant number density. For this, I use the same PARSEC stellar model isochrones and Kroupa initial mass function with a minimum mass of $0.08 M_\odot$ as in Section 2.2. Using the isochrones with metallicities corresponding to each monoabundance population, weighted by the fitted age distribution $g(\tau \mid \tau_0, \omega)$ for that monoabundance population, I calculate $N_{\text{giants}}/N_{\text{sm}}$: the fraction of all stars ever created that are currently in the red giant phase, which is again defined by $1 \leq \log g < 3$. Dividing the number density of giants by this fraction gives us the *sine morte* stellar number density. This assumes that the age distribution of each monoabundance population does not vary significantly across the Milky Way disk, which is reasonable for the range of R and z I am considering (Lian et al. 2022b).

[5]Latin for "without death", ['siːne 'mɔrte] IPA pronunciation, or 'seen-ay mort-ay'.

Next, I calculate the *sine morte* stellar mass density by multiplying the *sine morte* stellar number density by the average star's initial mass, $\langle M_{\rm int} \rangle$. By definition, the average mass of stars in the *sine morte* population is the average initial mass, which is only dependent on the initial mass function. Thus I calculate $\langle M_{\rm int} \rangle$ from the same Kroupa IMF, finding a value of $0.59 M_\odot$. All combined, the *sine morte* stellar mass density is given by

$$\rho_{\rm sm}(\mathbf{x}) = \frac{\langle M_{\rm int} \rangle}{N_{\rm giants}/N_{\rm sm}} \cdot n_{\rm giants}(\mathbf{x}) \,. \tag{2.6}$$

The difference between the two populations at the position of the Sun is illustrated in Fig. 2.2; though similar, there are subtle differences largely caused by the fact that the distribution of ages changes as a function of [Fe/H], as shown in Fig. 2.1. The ratio between the *sine morte* stellar mass density and the red giant number density is plotted in the top right panel in Fig. 2.1.

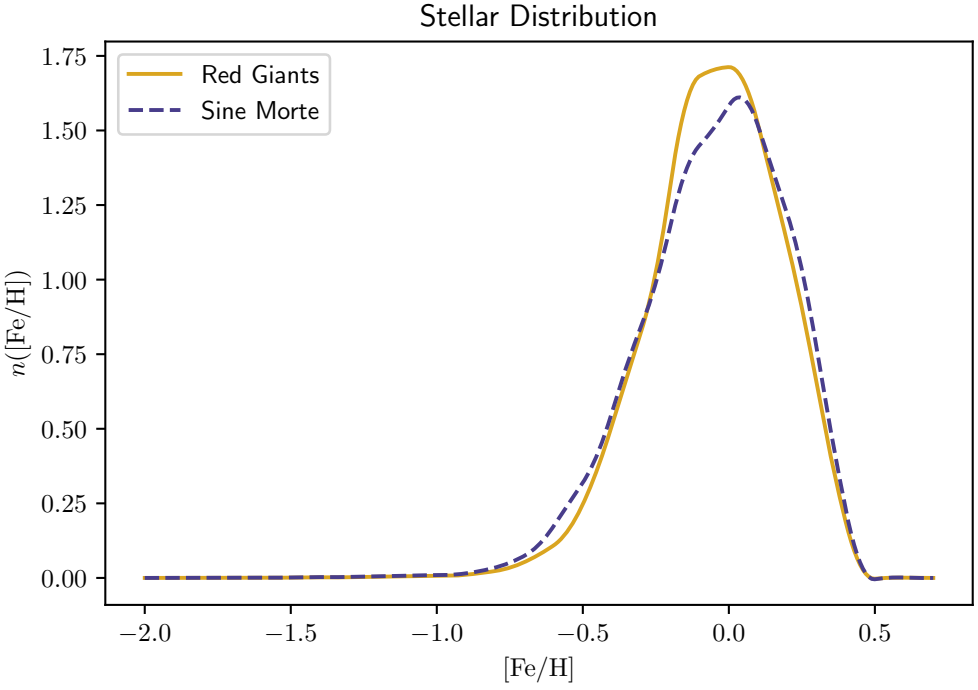

Figure 2.2: Comparison of the [Fe/H] distribution of red giants and the [Fe/H] distribution of the *sine morte* stellar population around the Sun, both normalised. Though similar, there are subtle differences largely caused by the fact that the distribution of ages changes slightly as a function of [Fe/H], as shown in Fig. 2.1.

For the monoabundance populations with [Fe/H] < -0.5, without reliable age measurements, I calculate an upper limit for the *sine morte* mass density. I assume an old age distribution, with mean $\tau_0 = 12\,\mathrm{Gyr}$ and standard deviation $\omega^{-\frac{1}{2}} = 1\,\mathrm{Gyr}$, which minimises $N_{\mathrm{giants}}/N_{\mathrm{sm}}$. Even with this upper limit, below I find that stars with [Fe/H] < -0.5 contribute a very small number of ISOs, making my conclusions independent of this approximation.

The chemical model I use in Section 2.3.1 to link the composition of ISOs to the composition of stars depends only on stellar metallicity [Fe/H], so when I evaluate the model I sum the *sine morte* distribution over the bins in [α/Fe] to get a distribution in only [Fe/H] bins. To ensure accurately fitted models, I include only monoabundance populations with 20 or more observed stars. I then smooth this binned distribution by taking the derivative of a spline fit to the cumulative distribution, knotted at the edges of the bins. Plotted in Fig. 2.3 is the *sine morte* metallicity distribution $\rho_{\mathrm{sm}}([\mathrm{Fe/H}])$ evaluated at the position of the Sun ($R = 8.1\,\mathrm{kpc}$, $z = 0.021\,\mathrm{kpc}$, GRAVITY Collaboration et al. (2018) and Bennett and Bovy (2019)), and integrated over the broader $R = 4\,\mathrm{kpc} - 12\,\mathrm{kpc}$ and $|z| = 0 - 5\,\mathrm{kpc}$ range of the Galactic disk I am modelling.

2.3 Predicting the Interstellar Object Distribution

In the previous section, I calculated the *sine morte* stellar population of the Milky Way from the APOGEE survey. In this section I describe how to predict an example physical property of the Galactic ISO population — the ISO water mass fraction distribution — from this stellar population.

2.3.1 Protoplanetary Disk Model

I make the foundational assertion that all ISOs I consider form as planetesimals in a protoplanetary disk (‘Oumuamua ISSI Team et al. 2019). A protoplanetary disk has, to first order, the same composition as the star it forms around, since they both form from the same molecular cloud core. Under this assumption, Bitsch

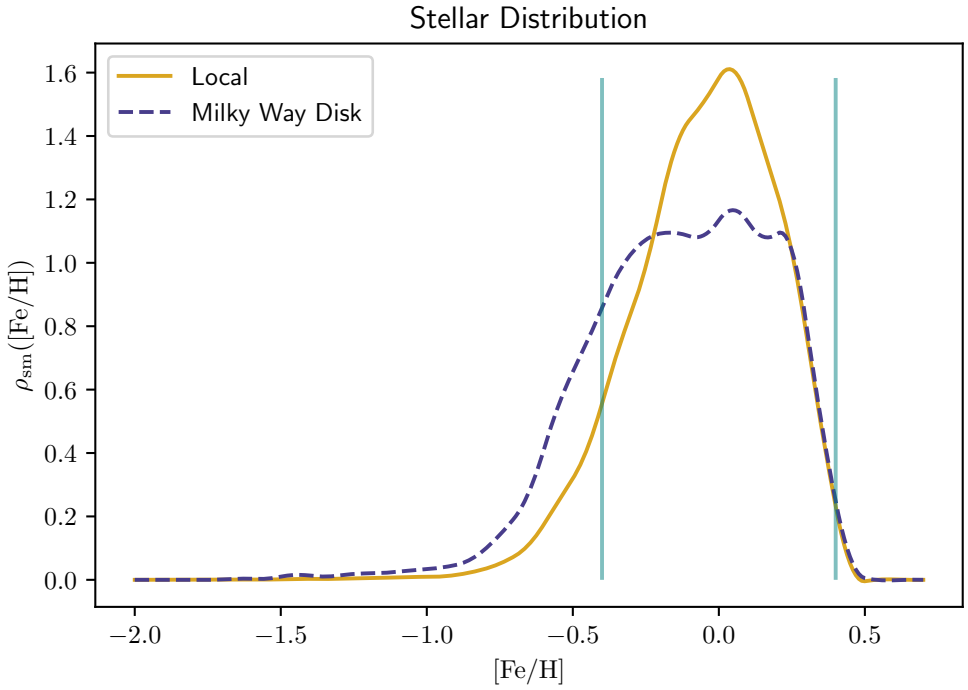

Figure 2.3: The normalised mass-weighted *sine morte* stellar metallicity distribution, evaluated at the position of the Sun and integrated over the range of the Milky Way disk I am modelling. Vertical lines show the range in [Fe/H] for which I model variations in the water mass fraction f_{H_2O} of ISOs

and Battistini (2020) predict the composition of planetesimals formed around stars of different metallicities. They do this for stars with metallicities in the range $-0.4 \leq [\text{Fe/H}] \leq 0.4$, using the average elemental composition of stars at each value of [Fe/H] in the GALAH DR2 (Buder et al. 2018), and for planetesimals that form both interior and exterior to the water ice line: the inner edge of the region of the protoplanetary disk where it is cool enough to form water ice. I assume that each star in the *sine morte* population produces only ISOs with their composition set by the Bitsch and Battistini (2020) formula for that metallicity, exterior to the water ice line, as plotted in Fig. 2.4. While in reality stars will each produce a distribution of ISOs that formed at different positions in their protoplanetary disk and thus have a range of compositions, this simplification of only modelling planetesimals which form exterior to the water ice line is justified by the proportionally greater reservoir of snowline-exterior planetesimals, and the higher efficiencies of formation mechanisms

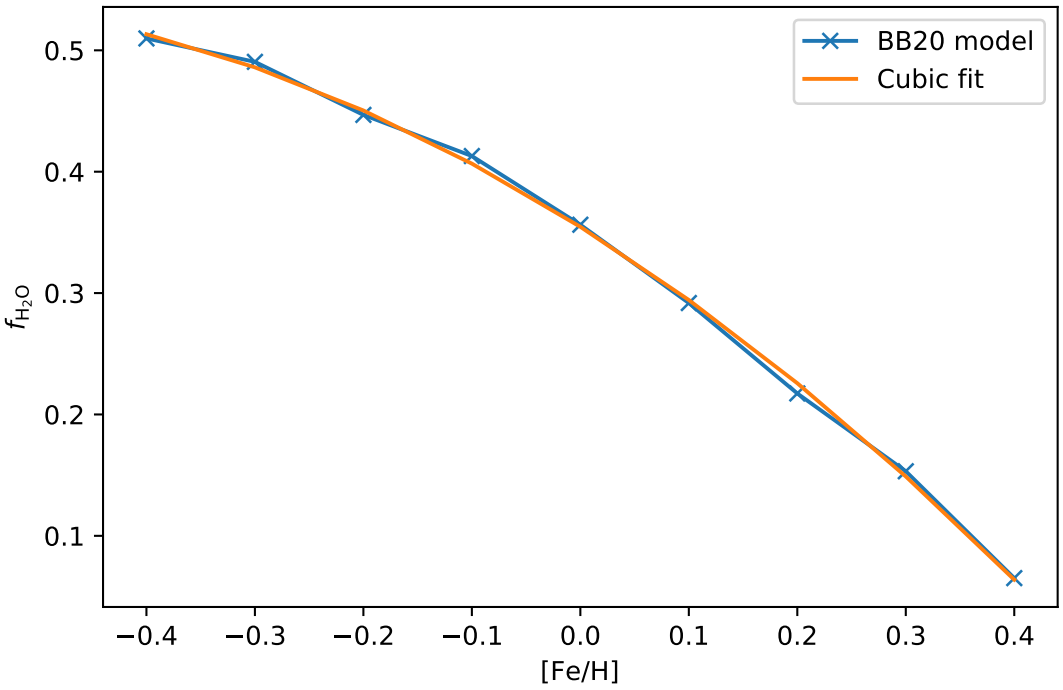

Figure 2.4: The relation between parent-star metallicity and ISO water mass fraction derived from the model of Bitsch and Battistini (2020). The water fraction decreases with metallicity due to the increased prevalence of more-reactive carbon which forms CO_2, taking up oxygen.

dynamically stripping them into the interstellar population (Fitzsimmons et al. 2023). In the Solar System, the vast majority of Oort cloud objects are ice-rich (Meech et al. 2016); therefore both these and the majority of ISOs produced by the Solar System must have formed outside of the water ice line (Filacchione et al. 2022). Additionally, planetesimals beyond the water ice line are more loosely bound to their parent stars, so will be more easily ejected (e.g. Moro-Martín (2018)).

I focus on the mass fraction of water, f_{H_2O}, as this varies significantly and decreases monotonically with [Fe/H] in the models of Bitsch and Battistini (2020). To obtain a smooth map from [Fe/H] to f_{H_2O}, I fit a third-order polynomial to the water ice mass fraction data points in figure 10 of Bitsch and Battistini (2020). For metallicities outside the range of $-0.4 \leq$ [Fe/H] ≤ 0.4 I assume that the relationship between f_{H_2O} and [Fe/H] continues to be monotonic, with f_{H_2O} remaining high beyond the low [Fe/H] limit and remaining low beyond the high [Fe/H] limit:

allowing us to track the fraction of ISOs with high, low, and intermediate water mass fraction. This range corresponds to $0.07 \leq f_{H_2O} \leq 0.51$ in water mass fraction.

I assume that every star produces ISOs, and the number of ISOs produced by each star depends on its mass and metallicity. Lu et al. (2020a) argue that the mass of planet-forming material in a protoplanetary disk is proportional to both the mass of the host star mass M_* and its metal mass fraction Z, which is well approximated by $Z_\odot 10^{[Fe/H]}$ at small values ($Z_\odot = 0.0153$; Caffau et al. 2011). In the absence of confirmed and comprehensive knowledge of ISO formation mechanisms, I use this as a reasonable proxy for the number of ISOs produced by each star. However, the number of ISOs produced by a star may not be simply proportional to the mass of planet-forming material, because ISO production also requires the ejection of planetesimals. As discussed in §1.1.1, one major ISO ejection pathway is scattering by giant planets, the occurrence of which has its own metallicity dependence (Osborn and Bayliss 2020), meaning the metallicity dependence of ISO production could be complex.

I assume the number of ISOs produced by each star is proportional to its mass, while assuming the dependence of ISO production on metallicity can be modelled as a power law: thus the number of ISOs produced is proportional to $M_* \cdot 10^{\beta[Fe/H]}$. Here $\beta = 1$ corresponds to the simple assumption that the number of ISOs produced is proportional to the mass of planet-forming material. $\beta = 0$ corresponds to no metallicity dependence at all. However, I expect $\beta > 0$: planetesimals require some fraction of dust and ice in order to exist, so some positive correlation is expected. I do not model the constant of proportionality here, as this depends on the size distribution of ISOs, which remains observationally unconstrained with only two ISOs (‘Oumuamua ISSI Team et al. 2019; Jewitt and Seligman 2023). I predict only the normalised distribution of ISO water mass fractions.

2.3.2 Predicting the ISO Population From the Stellar Population

Since the majority of ISOs are expected to be ejected by dynamical processes within several hundred Myr of a star's formation (Pfalzner and Bannister 2019; Fitzsimmons et al. 2023), I assume that the birth of a star and release of its ISOs are contemporaneous, and omit accounting for any delay. A fraction of a planetary system's bound planetesimals will become unbound later in a system's life, whether from its Oort cloud's continuous interaction with the Galactic environment, or in post-main-sequence escape (Veras et al. 2011, 2014; Levine et al. 2023); for simplicity I omit this smaller population here. As Oort cloud comets, which also occupy an interstellar environment (Kaib and Volk 2022), do not exhibit substantive erosion after 4.5 Gyr (Stern and Shull 1988), I continue with the expectation that ISO erosional processes are broadly similar to those of Solar System comets (e.g. Guilbert-Lepoutre et al. 2015). This implies ISOs from stars prior to the Sun will outlive their parent stars. I thus use the *sine morte* stellar distribution established in Section 2.2.3. For assessing the water mass fraction of the resulting population, I assume processing in the interstellar medium has a negligible effect[6], and that ISOs broadly have the water mass fraction of their source planetesimal populations.

To link the spatial distribution of stars throughout the Galaxy to the ISOs they produced, I need to model their combined Galactic dynamics. ISOs are not expected to remain near to their parent stars on Gyr timescales, and stars do die. However, it is helpful to consider what the behaviour of the ISO population is in the case that neither of these are true. If ISOs did remain near their parent stars and both ISOs and stars existed for an infinite length of time, the number density distribution of ISOs with a given water mass fraction f_{H_2O} and position in the Galaxy $\mathbf{x}$ in the present day, denoted $n_{ISO}(\mathbf{x}, f_{H_2O})$, would be equal to the number of ISOs produced by stars currently at the same position and of the corresponding

[6]While this is valid for water, it may not hold for other species; e.g. Seligman et al. (2022) suggest that processing in the interstellar medium will remove CO and CO_2 relative to H_2O.

metallicity [Fe/H]. Under the model of Section 2.3.1, the number of ISOs produced by a star of mass M_* and metallicity [Fe/H] is proportional to $M_* \cdot 10^{\beta[\mathrm{Fe/H}]}$, thus

$$n_{\mathrm{ISO}}(\mathbf{x}, f_{\mathrm{H_2O}} \mid \beta) \propto 10^{\beta[\mathrm{Fe/H}]} \cdot \frac{\mathrm{d}[\mathrm{Fe/H}]}{\mathrm{d}f_{\mathrm{H_2O}}} \cdot \rho(\mathbf{x}, [\mathrm{Fe/H}]) \tag{2.7}$$

where $\rho(\mathbf{x}, [\mathrm{Fe/H}])$ is the mass density distribution of stars at position $\mathbf{x}$ with the metallicity [Fe/H] corresponding to the ISO water mass fraction $f_{\mathrm{H_2O}}$, and $\mathrm{d}[\mathrm{Fe/H}]/\,\mathrm{d}f_{\mathrm{H_2O}}$ is the gradient of the relationship between [Fe/H] and $f_{\mathrm{H_2O}}$ described in Section 2.3.1.

The fact that stars do in fact die is then corrected for by replacing $\rho(\mathbf{x}, [\mathrm{Fe/H}])$ in this equation with $\rho_{\mathrm{sm}}(\mathbf{x}, [\mathrm{Fe/H}])$, the *sine morte* stellar mass density introduced in Section 2.2.3. Correcting for the fact that ISOs disperse from near their parent stars is more complex, so I proceed with some simplifying assumptions. Once ejected, unless its resultant velocity exceeds the Galactic escape velocity, an ISO will orbit the Galactic centre, as stars do. I assume ISOs are ejected relatively slowly from their parent planetary systems compared to the stellar velocity dispersion. This is justified assuming ejection velocities $< 10\,\mathrm{km\,s^{-1}}$, the maximum ejection velocity from a planetary system under an expected suite of scattering mechanisms (Pfalzner et al. 2021b; Fitzsimmons et al. 2023; Albrow et al. 2024), and the velocity dispersions of stars $\gtrsim 20\,\mathrm{km\,s^{-1}}$ measured in the Solar Neighbourhood (Anguiano et al. 2020). Stars form on near-circular orbits around the Galactic centre (Frankel et al. 2020), so a cloud of recently ejected ISOs will all have similar orbits to their parent star: nearly circular with similar ranges of oscillation in Galactocentric R and z. However, the slight differences in their orbits will give the ISOs different orbital periods around the Galactic centre, meaning they will disperse along their similar near-circular orbital paths. Therefore, though ISOs do not stay near their parent star, I assume here that they only disperse in the azimuthal direction, and remain in the same R and z range as their parent star. This assumption is backed up by the recent work of Forbes et al. (2024), which explores the development of tidal streams of ISOs extending around the Galaxy from their parent stars. Under

this assumption equation 2.7 still holds if the stellar density model is axisymmetric, depending only on R and z, as does ours:

$$n_{\mathrm{ISO}}(R, z, f_{\mathrm{H_2O}} \mid \beta) \propto 10^{\beta[\mathrm{Fe/H}]} \cdot \frac{\mathrm{d[Fe/H]}}{\mathrm{d}f_{\mathrm{H_2O}}} \cdot \rho_{\mathrm{sm}}(R, z, [\mathrm{Fe/H}]) \tag{2.8}$$

Orbits around the Galactic centre can evolve with time, due to the influence of perturbing potentials such as spiral arms, the bar and molecular clouds. These effects can cause both dynamical 'heating', an increase in the size of radial and vertical excursions from a circular orbit, and 'migration', changes to the radius of an orbit while it remains nearly circular (Sellwood and Binney 2002). I introduced Eq. 2.8 with the assumption that an ISO will stay in the same range of R and z as its parent star. Due to their azimuthal separation, the star and ISOs will experience slightly different perturbing potentials, causing their orbits to evolve adjacently but independently. However, if the Galactic stellar and ISO distributions are sufficiently axisymmetric, perturbations will consistently change together both the orbits of stars and the orbits of a corresponding number of ISOs. Thus, Eq. 2.8 holds for my model.

In this work I predict the distribution of ISOs in $f_{\mathrm{H_2O}}$ both at particular values of R and z and integrated over the whole Milky Way. Since I do not model the total number of ISOs, I remove the need for the constant of proportionality in Eq. 2.8 by normalising each n_{ISO} distribution I calculate with

$$p(f_{\mathrm{H_2O}} \mid \beta) = \frac{n_{\mathrm{ISO}}(f_{\mathrm{H_2O}} \mid \beta)}{\int n_{\mathrm{ISO}}(f_{\mathrm{H_2O}} \mid \beta)\, \mathrm{d}f_{\mathrm{H_2O}}}\,. \tag{2.9}$$

This gives us the distribution of ISOs within the bounds of the protoplanetary disk chemical model: $0.07 \leq f_{\mathrm{H_2O}} \leq 0.51$. Outside of this range, I can calculate the fraction of ISOs with $f_{\mathrm{H_2O}} \leq 0.07$ and $f_{\mathrm{H_2O}} \geq 0.51$, by assuming that the relation between [Fe/H] and $f_{\mathrm{H_2O}}$ remains monotonic. Thus, all stars with $[\mathrm{Fe/H}] \leq -0.4$ contribute ISOs with $f_{\mathrm{H_2O}} \geq 0.51$, and all stars with $[\mathrm{Fe/H}] \geq 0.4$ contribute ISOs with $f_{\mathrm{H_2O}} \leq 0.07$.

2.4 Results

In this section I demonstrate the prediction framework of section 2.3 by making two different predictions. I demonstrate two different example values for a stellar metallicity dependence for ISO production, β, with $\beta = 1$ for my principal prediction and $\beta = 0$ as an alternate prediction.

2.4.1 Principal Prediction: $\beta = 1$

First, I predict the distribution of ISOs assuming that the number produced by each star is proportional to the star's metal mass fraction Z, by setting $\beta = 1$ in equation 2.8. As described in section 2.3.1, in the absence of concrete knowledge of ISO formation mechanisms this is a reasonable value to assume, and thus I consider this my principal prediction.

	Fraction of ISOs in each f_{H_2O} range	
ISO f_{H_2O} range	Solar Neighbourhood	Milky Way Disk
0.00–0.07	0.017	0.024
0.07–0.51	0.955	0.915
0.51–	0.027	0.061

Table 2.1: Primary prediction for the fraction of ISOs in each f_{H_2O} range evaluated at the position of the Sun and integrated over whole Milky Way, with $\beta = 1$.

Table 2.1 lists the the fraction of ISOs within and outside either end of the Bitsch and Battistini (2020) protoplanetary disk chemical model f_{H_2O} range, $0.07 \leq f_{H_2O} \leq 0.51$. I assess both the distribution of ISOs at the position of the Sun, at $R = 8.1\,\mathrm{kpc}$, $z = 0.021\,\mathrm{kpc}$ (GRAVITY Collaboration et al. 2018; Bennett and Bovy 2019), and the distribution of ISOs integrated over the region of the Milky Way disk I am modelling. In both cases, the vast majority of ISOs lie within the range of the model. The significant mass of stars beyond the lower [Fe/H] limit of the $\rho_{sm}([Fe/H])$ distribution in Fig. 2.3, both at the position of the Sun and over the whole Milky Way disk, do not contribute significantly to the fractions of ISOs in the high f_{H_2O} range. This is because of the exponential dependence of the number of ISOs produced by each star on [Fe/H] in Eq. 2.8.

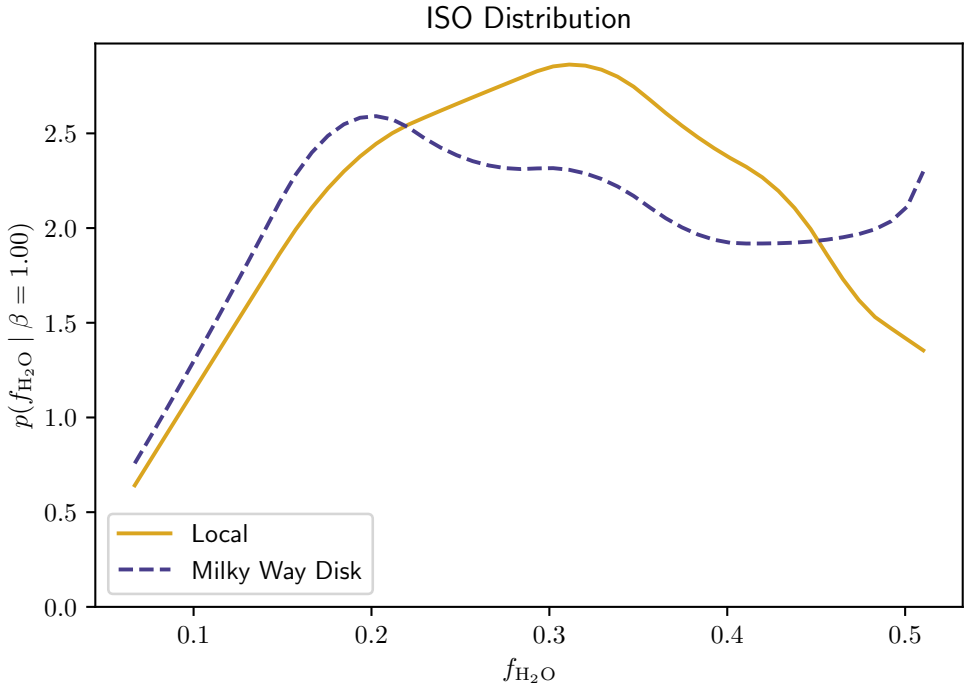

Figure 2.5: Primary prediction for the distribution of ISO water mass fractions, evaluated at the position of the Sun and integrated over the Milky Way disk, for $\beta = 1$.

Within the range of the chemical model, I can plot the distribution function of the ISO water mass fractions. Figure 2.5 shows both the population of ISOs around the Sun and over the whole Milky Way. The different shapes of the two metallicity distribution functions in Figure 2.3 is also apparent here, as the wider Milky Way metallicity distribution function results in a wider ISO water mass fraction distribution.

The distributions of ISOs around the Sun and averaged over the Milky Way disk are remarkably similar. I explore this in Figure 2.6, through the *sine morte* stellar mass [Fe/H] distribution and the ISO f_{H_2O} distribution within the range of the chemical model at a range of values of R, integrated over z. Also plotted are the median values of [Fe/H] and f_{H_2O} at each value of R. Clear in the left-hand panel of Fig. 2.6 is the well-studied Galactic metallicity gradient (Cheng et al. 2012), and in the right-hand panel is a corresponding gradient in ISO water mass fraction. Since the composition of ISOs depends on the chemical makeup of the stars that they form around, I expect trends in the chemical abundances of stars to be accompanied by

equivalent trends in the compositions of ISOs. Figure 2.6 also shows why the Solar neighbourhood distributions are similar to the whole-Galaxy integrated distributions in Figures 2.3 and 2.5: The Solar neighbourhood happens to be at an intermediate value of R (8.1 kpc), where both the stellar [Fe/H] distribution and therefore the ISO f_{H_2O} distributions are approximately midway between the high and low extremes.

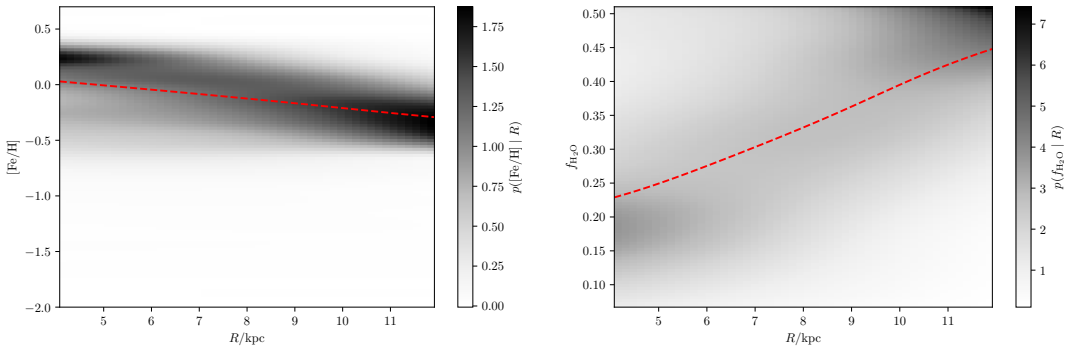

Figure 2.6: *sine morte* stellar mass distributions (left) and ISO water mass fraction distributions (right), integrated over z, at each distance to the Galactic Centre R. Both distributions are normalised such that at each value of R the integral over [Fe/H] or f_{H_2O} is unity. Dashed lines show the median value of each distribution at each R.

In these plots, I have normalised the distributions in [Fe/H] and f_{H_2O} such that at each value of R the integral over [Fe/H] or f_{H_2O} is unity. However, it is worth noting that my model implies the densities of both the stellar and ISO populations will decrease with distance from the Galactic centre. The exponential stellar density profile is well established (Jurić et al. 2008). Here I predict that the Galactic ISO population density profile will decrease faster than that of the stars: due to the metallicity dependence of the number of ISOs produced by each star, the higher-metallicity stars in the inner disk will produce more ISOs per unit of stellar mass than the lower-metallicity stars of the outer disk.

2.4.2 Alternate Prediction: $\beta = 0$

Setting $\beta = 1$ is just a choice in a basic and observationally unconstrained model. Therefore, I explore how changing its value affects the predicted ISO distribution. Lintott et al. (2022) predicted the ISO populations of galaxies from the EAGLE hydrodynamical simulation (Schaye et al. 2015) using the same protoplanetary disk

chemical model (from Bitsch and Battistini 2020) to map stellar metallicities [Fe/H] to ISO water mass fractions f_{H_2O}. However, Lintott et al. (2022) assumed that the number of ISOs produced by each star was independent of the star's metallicity. This is equivalent to setting $\beta = 0$ in Eq. 2.8 in this work, and I use this to make my alternate prediction. The resulting water mass fraction distributions for ISOs at the position of the Sun and integrated over the whole Milky Way are plotted in Figure 2.7 and tabulated in Table 2.2.

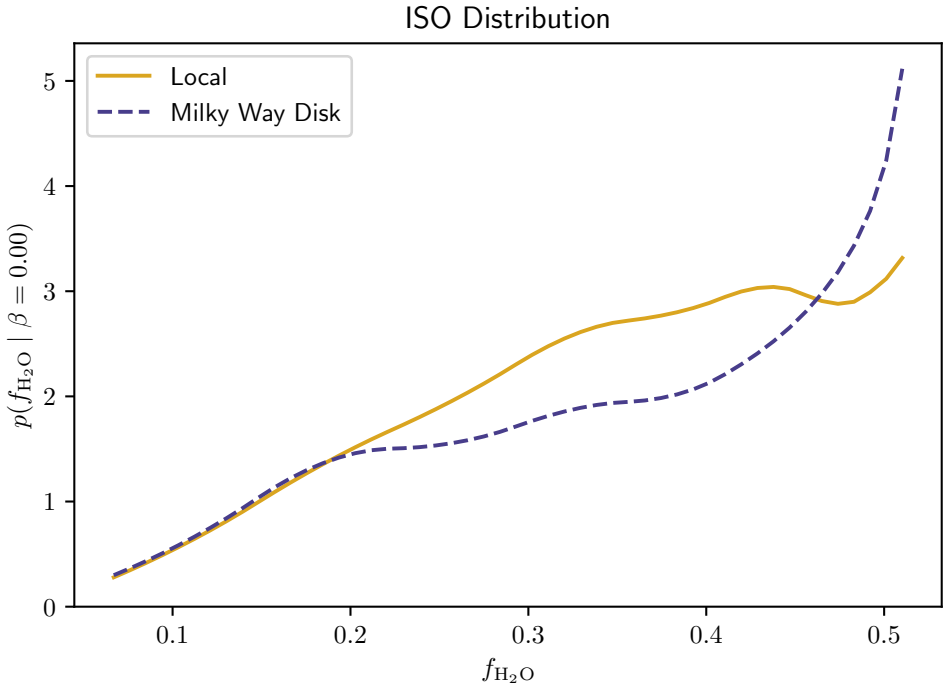

Figure 2.7: Alternate prediction for the distribution of ISO water mass fractions, evaluated at the position of the Sun and integrated over the Milky Way disk with $\beta = 0$: assuming the number of ISOs produced by each star is independent of the star's metallicity.

	Fraction of ISOs in each f_{H_2O} range	
ISO f_{H_2O} range	Solar Neighbourhood	Milky Way Disk
0.00–0.07	0.007	0.009
0.07–0.51	0.903	0.798
0.51–	0.090	0.194

Table 2.2: Alternate prediction for fraction of ISOs in each f_{H_2O} range, evaluated at the position of the Sun and integrated over the whole Milky Way with $\beta = 0$: assuming the number of ISOs produced by each star is independent of the star's metallicity.

Assuming $\beta = 0$ causes the ISO distribution to be more weighted towards a higher water mass fraction. These high water mass fraction ISOs come from low metallicity stars, which in this scenario no longer have their contributions to the ISO population suppressed by the exponential dependence on [Fe/H]. This means that the low metallicity tails of the $\rho_{\rm sm}([{\rm Fe/H}])$ distributions in Figure 2.3 now contribute a significant number of ISOs with $0.51 < f_{\rm H_2O}$: almost 20% when averaged over the Milky Way disk. A comparison of these results to those of Lintott et al. (2022) is discussed in section 2.5.1.

2.5 Discussion

2.5.1 Comparison to Previous Work

Lintott et al. (2022) made a prediction of the ISO population of a simulated Milky Way-like galaxy from the EAGLE hydrodynamical cosmological simulation (Schaye et al. 2015; Mackereth et al. 2018), using a model equivalent to that of this work with $\beta = 0$. Whereas I predict a single-peaked $f_{\rm H_2O}$ distribution, they predicted an ISO distribution with a significant number of ISOs with water mass fraction both below and above the range of the protoplanetary disk model, which they interpret as a bimodal distribution in ISO composition.

There are expected reasons for the difference between the prediction here, based on the observed Milky Way stellar population, and the prediction by Lintott et al. (2022) based on the simulated EAGLE galaxy. The EAGLE galaxy has a much wider [Fe/H] distribution than the Milky Way, with many more stars outside of the [Fe/H] range of the protoplanetary disk model. As a smoothed particle hydrodynamics simulation, EAGLE is susceptible to producing galaxies with [Fe/H] distributions wider than those observed in nature, due to underestimating metal mixing between particles (Wiersma et al. 2009). Therefore the results of this chapter, based on the observed stellar population of the Milky Way, give a much more accurate prediction for the Milky Way's population of ISOs.

2.5.2 Distinguishing Local and Galactic Populations of ISOs

The results of Section 2.4.1 show that the well-studied metallicity gradient of the Milky Way has a corresponding ISO composition gradient, with ISOs generally having a higher water mass fraction at larger Galactocentric radii. Although I can only observe the compositions of ISOs which pass through the inner Solar System, it is still instructive to model how the distribution of ISOs varies across a wider portion of the Galactic disk. This is because I have made assumptions about the Galactic dynamics of ISOs, under which the distribution of ISOs at a point in the Galaxy corresponds to the distribution of stars at that same point. If these assumptions break down, then the particular way in which they break down will affect the population of ISOs detectable in the Solar System in a related, calculable way.

For example, radial migration, caused by the non-axisymmetric potential of spiral arms, flattens the Milky Way metallicity gradient by blurring the metallicity distribution in the radial direction (Vickers et al. 2021). This widens the stellar metallicity distribution around the Sun as stars migrate in from the metal-poor outer disk and out from metal-rich inner disk. However ISOs may be less susceptible to radial migration if they have more random motion than stars on average (Daniel and Wyse 2015), introduced by their ejection. The stars currently in the Solar neighbourhood may thus have a wider range of Galactocentric radii of origin than the ISOs. This would make the distribution of observable ISO compositions narrower than would be predicted from the distribution of stars.

2.5.3 An Estimation of the ISO Production Metallicity Dependence

The two different predictions made in Section 2.4 demonstrate that the Galactic population of ISOs is sensitive to small differences in the processes that affect their formation and evolution. This means that if models of these processes can be combined to make accurate predictions of the ISO population, then the framework described in Section 1.6 can be used to make inferences about those processes.

In particular, the predictions of sections 2.4.1 and 2.4.2 show that the ISO distribution around the Sun is sensitive to the metallicity dependence of the number of ISOs produced by each star, β. These two predictions can then be compared to a sample of ISOs by calculating the likelihood of each of these predictions producing the observed distribution of water mass fractions, such as for the ISOs expected to be found by the Legacy Survey of Space and Time (LSST) of the Vera C. Rubin Observatory. For a more general result, this likelihood can be combined with a prior on β and Bayes' theorem to calculate a posterior distribution for β.

Though the work of this Chapter has been carried out in expectation of a larger sample of ISOs being known in the future, there is already a preliminary estimate of the ISO water mass fraction distribution: the water mass fraction of 2I/Borisov. Due to the unknown composition of 1I/'Oumuamua, this is the only ISO composition estimate possible. I adopt a value of $f_{H_2O} = 0.3$, after that of Seligman et al. (2022) inferred from the production rates of 2I's coma. However, this value is more useful for demonstrative purposes than as a finely constrained estimate; estimating a comet's bulk composition from the composition of its coma is challenging. Additionally, Seligman et al. (2022) note that the primoridial compositions of interstellar comets calculated from production rates observed in the Solar system could be affected by preferential desorbtion of CO and CO_2 relative to H_2O in the interstellar medium.

With this observed distribution of f_{H_2O} I can calculate a posterior distribution for β. I use my model for the distribution of ISOs around the Sun, and taking a uniform prior on β means that the posterior is simply proportional to the likelihood, equal to the value of the f_{H_2O} distribution. For $f_{H_2O} = 0.3$ this posterior is maximized by a value of $\beta = 1.33$. The distribution of ISOs at this value is listed and plotted in Table 2.3 and Figure 2.8. The symmetric 90% confidence limit for this estimation of β is $\beta \in (-1.3, 7.2)$. This is of course an absurdly wide interval for a power-law index, and contains physically implausible negative values. The physically implausible values could be removed from the confidence interval by using a physically motivated prior on β — but with one known value of f_{H_2O} this would make the posterior dominated by the prior. Using the larger sample of ISOs that

the LSST is expected to find (Chapter 4) will much better constrain the posterior for β and other parameters used in models with this framework.

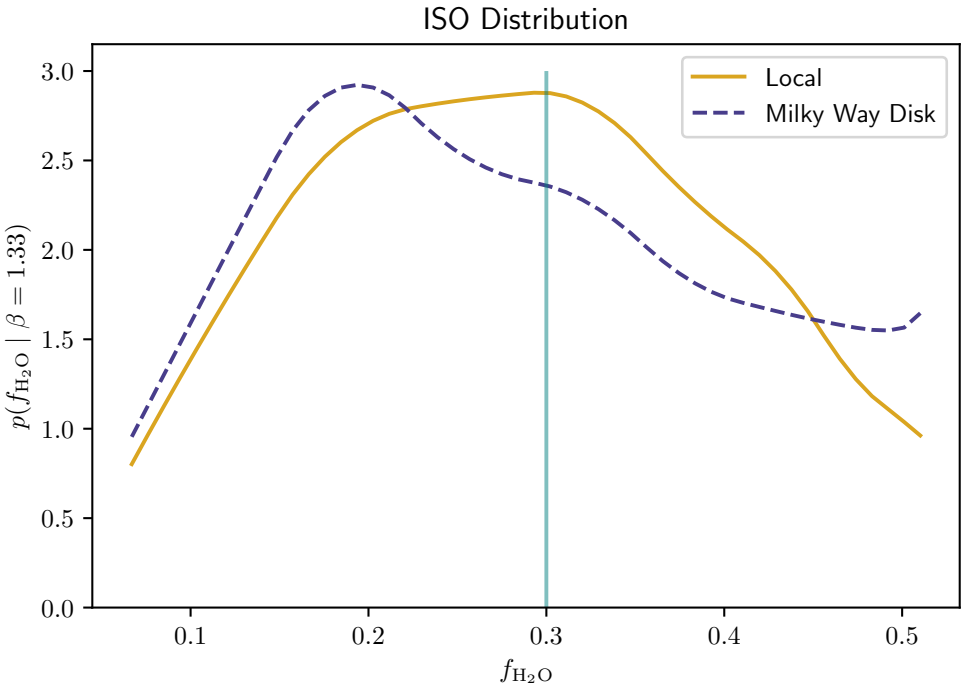

Figure 2.8: Distribution of ISO water mass fractions, evaluated at the position of the Sun and integrated over the Milky Way disk, with maximum *a posteriori* estimate of $\beta = 1.33$. At $f_{H_2O} = 0.3$ a vertical line marks the measured water mass fraction of 2I/Borisov.

	Fraction of ISOs in each f_{H_2O} range	
ISO f_{H_2O} range	Solar Neighbourhood	Milky Way Disk
0.00–0.07	0.022	0.031
0.07–0.51	0.960	0.930
0.51–	0.018	0.040

Table 2.3: Predicted fraction of ISOs in each f_{H_2O} range, evaluated at the position of the Sun and integrated over the Milky Way dist, with maximum *a posteriori* estimate of $\beta = 1.33$.

2.5.4 Selection Effects

It should be noted that the predictions in this work ignore some specific effects which will influence the population of ISOs I expect to be observable from the Earth.

The predictions in Section 2.4 are the distribution of ISOs in a smooth Galaxy-wide distribution, evaluated at the location of the Solar System. Gravitational focussing by the Sun will increase the density of ISOs in the inner Solar System in a velocity-dependent manner (e.g. Engelhardt et al. 2017; Forbes and Loeb 2019; Dehnen et al. 2022), and therefore also in a composition-dependent manner. This composition dependence is due to the fact that I expect compositionally and dynamically distinct populations of ISOs to come from the chemo-dynamically distinct stellar populations in the Milky Way thin and thick disks (c.f. Eubanks et al. 2021). The correlation between velocity and composition however is included in the model of Chapter 3; there for example in Fig 3.6 (Composition) the composition distribution for ISOs with perihelion $< 5\,\mathrm{au}$ includes more low $f_{\mathrm{H_2O}}$ objects.

Additionally, the Pan-STARRS near-Earth object survey (Chambers et al. 2016) that detected 1I/'Oumuamua, the observations of individual astronomers such as Gennadiy Borisov who discovered 2I/Borisov, and the LSST which will discover tens more ISOs: all have highly non-trivial selection functions. Since in order to be discovered an ISO needs to be detected in multiple observations which can be linked as the same object (e.g. Meech et al. 2017; Schwamb et al. 2023), these selection functions are dependent on ISO size, approach velocity, perihelion, and composition. Composition has a direct link to the detectability of ISOs, as 2I-sized and cometary ISOs will be more likely to be detected, as they will form a coma as they approach the Sun. These selection effects will need to be accurately accounted for, in order to draw accurate inferences from the LSST ISO sample, and I describe my work towards this in Chapter 4.

2.6 Summary

In advance of the LSST I lay out a framework to predict the Galactic distribution of ISOs using the stellar population of the Milky Way. Using the method of Bovy et al. (2016a), I fit simple density models to a sample of red giants in APOGEE binned in [Fe/H] and [α/Fe], and use these to evaluate the *sine morte* metallicity distribution of stars throughout the Galaxy's integrated history, across the Galactic

disk. Under the assumption that the spatial distribution of a population of ISOs will be the same as the *sine morte* distribution of stars which formed them, I use the protoplanetary disk model of Bitsch and Battistini (2020) to map the metallicity distribution of stars to the distribution of ISO water mass fractions. Localising my model to the Solar neighbourhood, I predict that 95% of ISOs around the Sun have water mass fraction $f_{\mathrm{H_2O}}$ between 0.07 and 0.51, with a peak around 0.35.

By considering the distribution of ISOs over the Galactic disk, I show that the well-studied Milky Way metallicity gradient has an equivalent gradient in ISO composition, with the median ISO water mass fraction increasing with distance from the Galactic Centre as the median stellar metallicity decreases. This causes the ISO water mass fraction distribution averaged over the Milky Way disk to be wider that the distribution around the Sun. Since I also predict higher-metallicity stars produce more ISOs than lower-metallicity stars, the Milky Way metallicity gradient implies that the radial ISO density profile is steeper than the exponential radial stellar density profile, making ISOs much more common in the inner Galactic disk than in the outer disk.

To demonstrate the use of these predictions for making inferences about the processes which affect the ISOs population, I use the composition measurement of 2I/Borisov to calculate a maximum *a posteriori* estimate for the power law slope of the ISO production metallicity dependence, β, to be 1.33, with a symmetric 90% confidence interval of $(-1.3, 7.2)$.

Encoded in the population of ISOs we will observe is a wealth of information about processes through Galactic history, from the evolution of the Milky Way to planet formation. The framework set out in this work is a novel approach that will allow us to appreciate how these treasures can further my understanding on both planetary and Galactic scales.

In the next two chapters I build on this work. I add ISO velocities and predictions of the chemodynamical distribution of the Galactic ISO population in Chapter 3, then in Chapter 4 I describe my contribution to the work of Dorsey et al. (2025), which predicts the selection biases that wll be present in the LSST ISO sample.

I
I am the two
I am you too
I am the stream

I am wind
I am rain
I am photon
I am wave

I am Gaiaaaaaaaaaaaaaaaaaaaaaaaaaaaaaaaaaaaaaaaaaaaaaaaaaaaaaaaaaaaaaaaaaaaaaaaaaaaaaaaaaaaaaaaaaaaaaaaaaaaaa
— King Gizzard & the Lizard Wizard

3

Interstellar Object Chemodynamics with Gaia

The work described in this chapter constitutes that published in Hopkins et al. (2025a), the entirety of which I led.

3.1 Introduction

The stellar population of the solar neighbourhood is highly complex. Its velocity distribution is highly non-Gaussian, with large overdensities called moving groups, known since Eddington (1906) and well-studied since *Hipparcos* (Dehnen 1998; Skuljan et al. 1999). These moving groups are not coeval (Nordström et al. 2004; Bensby et al. 2007; Famaey et al. 2008; Antoja et al. 2008), so while originally thought to be dispersed star clusters, they are now understood to be temporary and Galaxy-spanning structures, sculpted by resonances with the Galaxy's spiral arms and bar, which themselves may be transient (Quillen et al. 2011; Ramos et al. 2018; Antoja et al. 2018; Michtchenko et al. 2018; Hunt et al. 2018, 2019; Trick et al. 2021; Lucchini et al. 2023). The local stellar population also shows strong chemodynamical correlations: relationships between velocity and chemical composition (Bovy et al. 2012b, 2016b), and between velocity and age (Nordström et al. 2004).

As a product of the stellar population, the Galactic ISO population will inherit this complex nature. However, previous works model the ISO velocity distribution as a simple multivariate Gaussian (Whipple 1975; Sekanina 1976; McGlynn and Chapman 1989; Stern 1990; Cook et al. 2016; Engelhardt et al. 2017; Seligman and Laughlin 2018; Forbes and Loeb 2019; Marčeta and Novaković 2020; Hoover et al. 2022; Marčeta 2023; Marčeta and Seligman 2023). Additionally, no study yet accounts for the correlations of velocity with chemical composition which the ISOs will also inherit from their parent stars. Accurately modelling the chemodynamical distribution of the local ISO population is highly important: The velocity distribution of ISOs passing through the inner Solar System affects their detectability, something I investigate further in Chapter 4, and as a consequence it affects estimates of the total Galactic population size (Do et al. 2018), and thus inference on the various ISO production mechanisms (Moro-Martín et al. 2009). The breadth of the ISO velocity distribution also limits the potential for encounter and sampling visits to ISOs by spacecraft, which have finite Δv (Moore et al. 2021; Jones et al. 2024). Finally, the placement of discovered ISOs in the chemodynamical parameter space allows inferences to be made about their origins, and thus the processes such as planet formation and Galactic dynamics on which the Galactic ISO population depends.

In this chapter, I model the chemodynamics of the population of ISOs passing through the inner Solar System: its joint distribution in velocity, chemical composition and age. The prediction I produce forms the current iteration of the Ōtautahi–Oxford model, used in other works such as Forbes et al. (2024) and Dorsey et al. (2025). I do this by debiasing stellar data from *Gaia* DR3 (Gaia Collaboration et al. 2016, 2023) to build a model of the local stellar population within 200 pc of the Solar System. As in the previous chapter, I then combine this with the protoplanetary disk chemical model of Bitsch and Battistini (2020) which connects the chemical compositions of ISOs to the metallicities of their parent stars to predict the chemodynamical distribution of the background population of ISOs in the solar neighbourhood. Finally, while accounting for gravitational focussing I predict the properties of the ISO population streaming through the inner Solar System.

I predict that the velocity distribution of ISOs is richly featured, with the velocity of an ISO correlating with the metallicity and age of its origin star, and therefore its own composition and age. I show that these correlations can be used to make inferences about individual ISOs' composition and age based on their velocity alone, and demonstrate this with the two known ISOs. Finally I calculate the sample sizes needed to distinguish between my predictions and the smooth Gaussian distributions used in previous works to model the ISO velocity distribution.

3.2 Method

3.2.1 The Dataset

In Chapter 2 I used positions and elemental abundances of stars from APOGEE (Jönsson et al. 2020) for modelling the ISO spatial distribution over a large swath of the Galactic disk; in this chapter my focus is instead the velocity distribution in the solar neighbourhood, so I use data from the *Gaia* survey Data Release 3 (DR3) (Gaia Collaboration et al. 2016, 2018). This space-based observatory measured high-precision astrometry and astrophysical parameters for stars across the entire sky, making it the ideal choice for modelling the local stellar velocity distribution.

The dataset I use in this chapter is a subset of the stars in *Gaia* DR3 in the solar neighbourhood which have high-precision measurements of velocity, metallicity, and age. Obtaining this dataset requires making cuts and excluding stars without the full complement of required measurements; as a result this dataset is subject to selection bias. I describe how I account for the selection bias introduced by these cuts in order to estimate the true underlying stellar population in the next section (§3.2.2).

I define the solar neighbourhood as a sphere around the Solar System out to the somewhat arbitrary distance of 200 pc, similar in scale to the distances used by Antoja et al. (2018) and Recio-Blanco et al. (2023), so I take stars with *Gaia* trigonometric parallax ≥ 5 mas.[1] To ensure these parallaxes are accurate,

[1] N.B. Due to a parallax bias of size $\sim 10\,\mu$as (Lindegren et al. 2021) this will not correspond to exactly 200 pc.

I require `parallax_over_error` > 10, and in order to calculate the 3D velocities of each star, I require a radial velocity to have been measured and have an error of less than $5\,\mathrm{km\,s^{-1}}$.

For physical properties, I require the availability of GSP-Spec[2] metallicity [M/H] and GSP-Spec-based FLAME[3] ages, both of which are measured using data from the Radial Velocity Spectrometer (RVS; Cropper et al. 2018): [M/H] is measured by fitting RVS spectra to synthetic spectra from a five-parameter stellar atmosphere model (Recio-Blanco et al. 2023), and GSP-Spec-based FLAME age is calculated from these atmospheric parameters and isochrone fitting (Fouesneau et al. 2023). Comparing to literature values, GSP-Spec [M/H] estimates show no bias and a dispersion of 0.13 dex (Recio-Blanco et al. 2023), while FLAME ages have mean biases and dispersions of only 0.1 to 0.3 Gyr and 0.25 Gyr respectively (Fouesneau et al. 2023). To ensure accurate ages, I remove giants from the sample by requiring `flags_flame_spec` $= 0$ (Creevey and Lebreton 2022; Creevey et al. 2023; Fouesneau et al. 2023)[4].

These measurements have the highest accuracy available, but are only present for bright stars: the cuts described above result in a maximum magnitude of $G \simeq 14$. In the next section I describe how the selection effects these cuts introduce are accounted for. This yields a sample of 201 863 observed living stars. Though *Gaia* does detect white dwarfs (e.g. Gentile Fusillo et al. 2021; Jiménez-Esteban et al. 2023), it does not measure their age or composition, so I do not include them here.

3.2.2 Estimating the Selection Function

Gaia, like any survey, is subject to selection effects: it does not observe all stars, does not make every measurement for each of the stars it observes, and does not choose stars to make measurements for in an unbiased way. The cuts I make to produce a subsample of solar neighbourhood stars with high-precision velocities, metallicities and ages introduce additional selection biases. Thus in order to reconstruct the true

[2]General Stellar Parametrizer from Spectroscopy
[3]Final Luminosity Age Mass Estimator
[4]The *Gaia* archive ADQL query to retrieve this dataset can be found in Appendix A

underlying stellar population from my dataset, the selection function needs to be estimated. The selection function is equal to the fraction of stars from the underlying true population included in the dataset, as a function of the properties of the stars.

In this work I calculate two selection functions the first of which is the survey selection function (SSF). This is the probability of an individual star being included in the dataset, as a function of its apparent magnitude, colour and on-sky position. These are the quantities on which the probability of inclusion explicitly depends. The SSF can be estimated directly from the *Gaia* catalogue, but as explained in Sec. 3.2.3 cannot be used to debias the dataset.

Therefore using stellar population models I recast the SSF into an effective selection function (ESF), the fraction of a stellar population included in my dataset as a function of the stellar population's metallicity, age, distance and on-sky position.

First I estimate the SSF. I use the methods of Cantat-Gaudin et al. (2023) and Castro-Ginard et al. (2023), who estimate the SSF of *Gaia* DR3 empirically as a function of apparent magnitude, colour, and on-sky position. In general, this method would first require the catalogue completeness to be estimated. However, Cantat-Gaudin et al. (2023) find that the *Gaia* catalogue is 100% complete across the sky for the apparent magnitude range of my dataset ($G \leq 14$). This makes estimating the SSF more simple, as I can assume every star in the underlying true population brighter than $G = 14$ is recorded in the *Gaia* catalogue.

I can thus use the method of Castro-Ginard et al. (2023) to estimate the SSF as the fraction of the *Gaia* catalogue included in my dataset at each apparent magnitude, colour and on-sky position. Castro-Ginard et al. (2023) find that the SSF for their dataset, stars that have an RVS radial velocity measurement, depends on G magnitude, $G - G_{\rm RP}$ colour and on-sky position. Since my dataset is defined with cuts on quantities computed from the output of the RVS, I follow Castro-Ginard et al. (2023) in assuming that the SSF for my dataset depends only on magnitude, colour and on-sky position too. The method of Castro-Ginard et al. (2023) calls for binning in magnitude, colour and on-sky position (using HEALPix[5]; Górski et al.

[5]Hierarchical Equal Area isoLatitude Pixelation

2005), then within each bin counting the number *Gaia* catalogue stars (n) and the subset of these that are in the dataset (k).[6] The SSF is then estimated in each bin with $(k+1)/(n+2)$, with an uncertainty of $\sqrt{(k+1)(n-k+1)/(n+2)^2(n+3)}$.

The bins I use have widths in colour and magnitude of $\Delta G = 1$ and $\Delta(G-G_{\rm RP}) = 0.2$, and I bin the on-sky positions with HEALPix level 2. These bins have a larger width than the binning of Castro-Ginard et al. (2023); as my subsample is smaller, requiring more measured quantities and therefore more cuts, I use broader bins to ensure a sufficiently high k in each bin to retain statistical quality. For this same purpose, I follow Castro-Ginard et al. (2023) by grouping the Galactic polar caps (Galactic latitudes $|b| > 30\,\deg$) into one bin. To ensure uniformity across the sky and a low fractional uncertainty in the effective selection function described below, I set the SSF equal to zero in all colour-magnitude bins with any on-sky bin where $k < 2$. This does not affect any colour-magnitude bins where a significant number of stars are observed, retaining 98% of the stars in the dataset. This gives us the SSF in apparent magnitude, colour and sky position, plotted in 3.1.

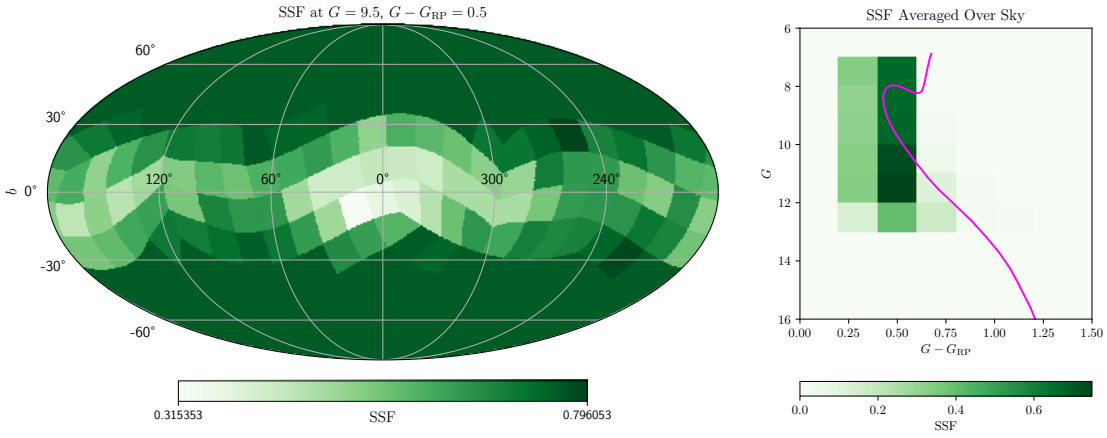

Figure 3.1: The SSF, the fraction of stars included in my dataset at each apparent magnitude G, colour $G - G_{\rm RP}$, and on-sky position. On the left is plotted the SSF at $G = 9.5$, $G - G_{\rm RP} = 0.5$ as a function of on-sky position in Galactic coordinates; the reduced SSF along the plane of the Galaxy is due to the higher number of background sources. On the right is plotted the SSF averaged over the sky ias a function of colour and magnitude, with an example isochrone ([M/H] = 0.05, age = 4.5 Gyr, $D = 102.5\,$pc) as used for calculating the ESF plotted in fuchsia.

[6] I list the Gaia archive ADQL queries that calculate and retrieve the values of k and n for each bin in Appendix A

From this SSF I estimate the ESF: the fraction of stars in the underlying true stellar population included in my dataset as a function of metallicity, age, distance, and on-sky position. I combine the PARSEC stellar model isochrones (Bressan et al. 2012; Marigo et al. 2017) weighted with a Kroupa IMF (Kroupa 2001)[7] to simulate the colour and magnitude distributions of populations of stars along with given metallicities, ages and distances. One of these isochrones is plotted as example on the right-hand side of Figure 3.1. When converting between absolute and apparent magnitudes I do not account for dust extinction, as within 200 pc of the Solar System this is limited to 1 mag at most in the G band (Green et al. 2019; Lallement et al. 2022).

These colour and magnitude distributions can be integrated with the SSF, a function of colour and magnitude, to estimate the fraction of each simulated stellar population that would be included in my dataset. I use isochrones with metallicities between -1.45 and 0.65 spaced by 0.1 and ages from 0.5 Gyr to 13.5 Gyr spaced by 1 Gyr; with these I estimate the ESF in bins in metallicity and age centred on each of these isochrones, calculated for distances from 2.5 pc to 197.5 pc spaced by 5 pc, in each on-sky position bin. These are plotted in Figure 3.2.

Features of the ESF that can be seen in Fig. 3.2 include the decrease in ESF at high metallicities and ages due to these stellar populations being redder and further from the regions of high SSF in colour-magnitude space (Fig. 3.1). For a similar reason, the ESF drops to zero at $D \lesssim 25$ pc because these stellar populations have sufficiently low G to fall entirely outside the region of non-zero SSF. Finally the ESF is reduced along the plane of the Milky Way, similar to the SSF.

As I argued in Chapter 2, since Oort cloud comets have survived 4.5 Gyr in an interstellar environment with little erosion (Guilbert-Lepoutre et al. 2015), ISOs will also largely remain intact and outlive their parent stars. Therefore, in

[7]To quantify how changing the IMF used to calculate the ESF affects my results, I also calculated an alternative ESF using the log-normal IMF of Chabrier (2003). Since my results consist of relative distributions and not absolute values, to compare the two ESFs I scale them to have the same mean value, then calculate the mean fractional difference between the two. I find this to be only 0.8% therefore the choice of IMF does not significantly affect my results. I use only the Kroupa-based ESF for the rest of this work.

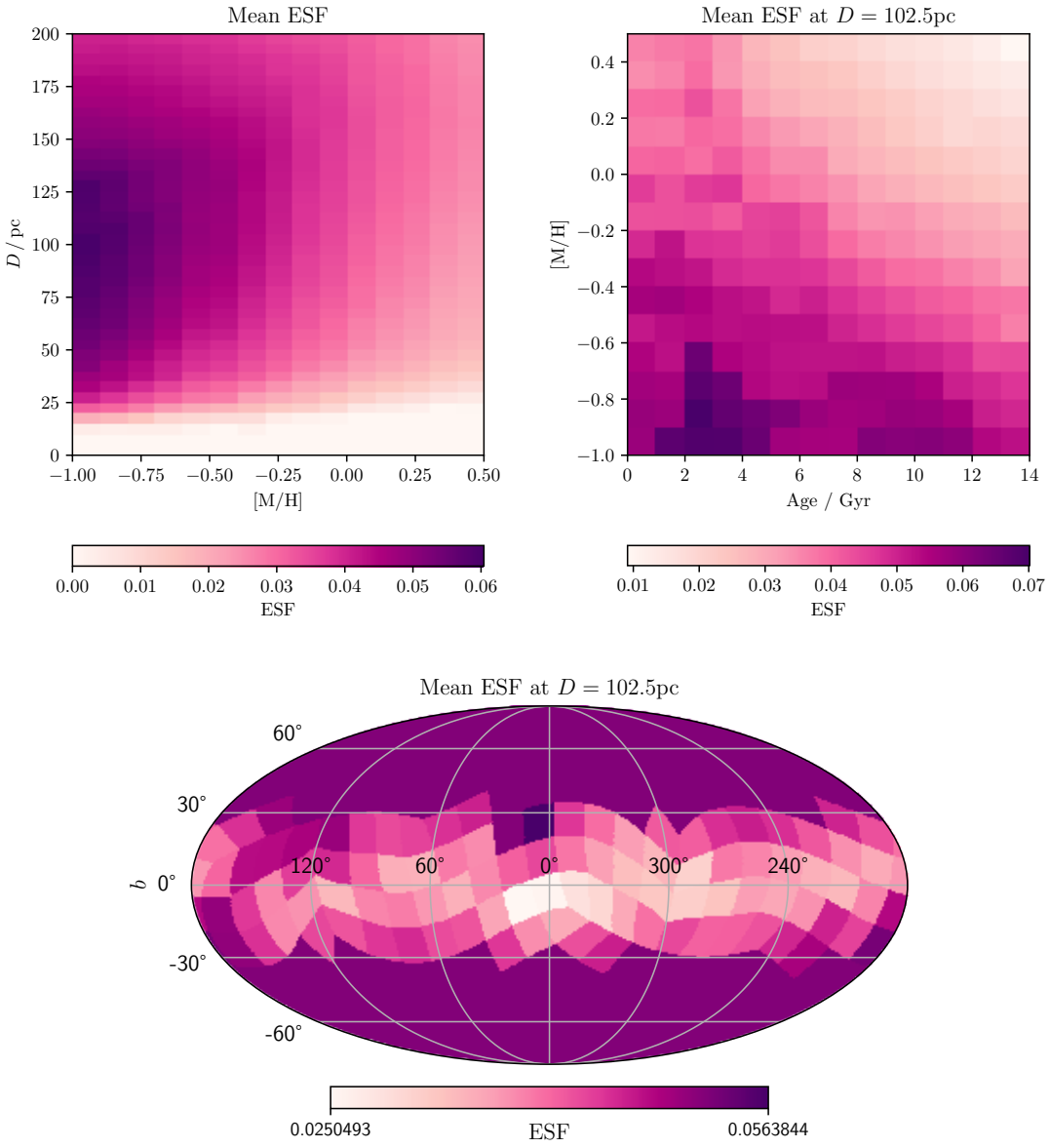

Figure 3.2: The ESF, the fraction of stars in the *sine morte* population included in my dataset at each metallicity [M/H], age, distance D and on-sky position. Top left: the ESF averaged over age and on-sky position as a function of [M/H] and D. Top right: the ESF at $D = 102.5\,\mathrm{pc}$ averaged over on-sky position as a function of [M/H] and age. Bottom: The ESF at $D = 102.5\,\mathrm{pc}$ averaged over [M/H] and age as a function of on-sky position in Galactic coordinates.

order to predict the ISO population, I must once again estimate the *sine morte* stellar population: what the stellar population would be without stellar death. Conveniently, this can be done while debiasing my dataset by treating stellar death as a selection effect removing stars from the observable population[8]. When calculating the ESF as described above, I compute and use the fraction of all stars ever formed in each simulated population, rather than the fraction of stars currently living. Thus, the ESF is the fraction of the *sine morte* stellar population at each metallicity, age, distance and on-sky position included in my dataset, and by debiasing my dataset with this ESF I recover the *sine morte* stellar population.

3.2.3 Debiasing the Dataset

Each star in my dataset has a measured velocity, metallicity, age, distance (via parallax) and on-sky position. It is useful to consider this dataset as a series of points in this parameter space of observables, as throughout the rest of this thesis I will estimate different stellar and ISO populations in and around the Solar System as discrete distributions by applying different sets of weights to these points.

For now, I estimate the solar neighbourhood *sine morte* stellar population by debiasing the dataset. The ESF is equal to the fraction of the *sine morte* population included in the dataset at each metallicity, age, distance and on-sky position. Thus the value of 1/ESF, evaluated at the metallicity, age, distance and on-sky position of a star in the dataset, is equal to the number of stars with the same properties in the *sine morte* population represented by that one star in the dataset. Thus, I can estimate the *sine morte* stellar population by reweighting each star in my dataset by its value of 1/ESF. The median value of ESF evaluated at each of the stars in my dataset is 1/22.5, meaning the median star in the dataset represents 22.5 stars in the solar neighbourhood *sine morte* population.[9]

[8] *For dead men, as you know, tell no tales* — Saadi Shirazi (translated by E. G. Browne; Pilmer 1937)

[9] If this selection fraction seems low, remember that this is the fraction of all stars ever born in a stellar population which are currently alive and have accurate measurements of velocity, metallicity, and age, passing each of the cuts in §3.2.1. Additional sanity check: if the $\sim 2 \times 10^5$ stars in the dataset each represent ~ 20 stars within a spherical volume of $4\pi(200\,\mathrm{pc})^3/3 \simeq 3 \times 10^7\,\mathrm{pc}^3$, this implies a stellar density of $\sim 0.1\,\mathrm{pc}^{-3}$, a good approximation to the true value (Bovy 2017).

The reason the SSF cannot be used to debias my dataset is that the SSF is non-zero only in a narrow colour range ($0.2 \leq G-G_{RP} < 0.6$, see Fig. 3.1), so cannot account for the contributions of stars outside of this range. Conversely, the ESF remains non-zero across almost all of parameter space, meaning the entire stellar population within 200 pc can be reconstructed as all populations are represented by at least a fraction of their stars in the *Gaia* sample and thus their contributions can be accounted for. The only exceptions to this are in bins at distances closer than 25 pc, so to ensure uniformity I cut the few stars with observed parallax > 40 mas. This leaves a final data sample of 201 426 stars, points in the parameter space of observables that when weighted by 1/ESF estimates the local *sine morte* population.

3.2.4 The Local *Sine Morte* Stellar Distribution

In the above sections I described how I estimated the solar neighbourhood *sine morte* stellar population as a discrete distribution of the stars in my *Gaia* DR3 dataset, reweighted by 1/ESF. This distribution in velocity, age and metallicity is plotted in Figure 3.3.

In Fig. 3.3 (In-Plane Velocity and Out-of-Plane Velocity) the velocity distribution is plotted in its right-handed Cartesian components relative to the Solar System barycentre velocity: U towards the Galactic Centre, V in the direction of Galactic rotation, and W out of the plane of the Galaxy. Immediately obvious is the rich structure in the stellar velocity distribution: the moving groups and branches (compare to Fig. 5 of Antoja et al. 2008, for identification). As described in Sec. 3.1, these overdensities are caused by resonances with the Galactic spiral arms and bar carving out furrows in the velocity distribution, and are not dispersed clusters. There is less structure in the W distribution than the U and V distribution. With a yellow square I mark the local standard of rest (LSR; Schönrich et al. 2010), the velocity that a star on a circular orbit at the distance of the Solar System from the Galactic centre would have in a azimuthally-smoothed approximation to the Galactic potential.

I measure an age distribution for the solar neighbourhood plotted in Fig. 3.3 (Age) that is similar to that of Nordström et al. (2004). I also recover a known feature of

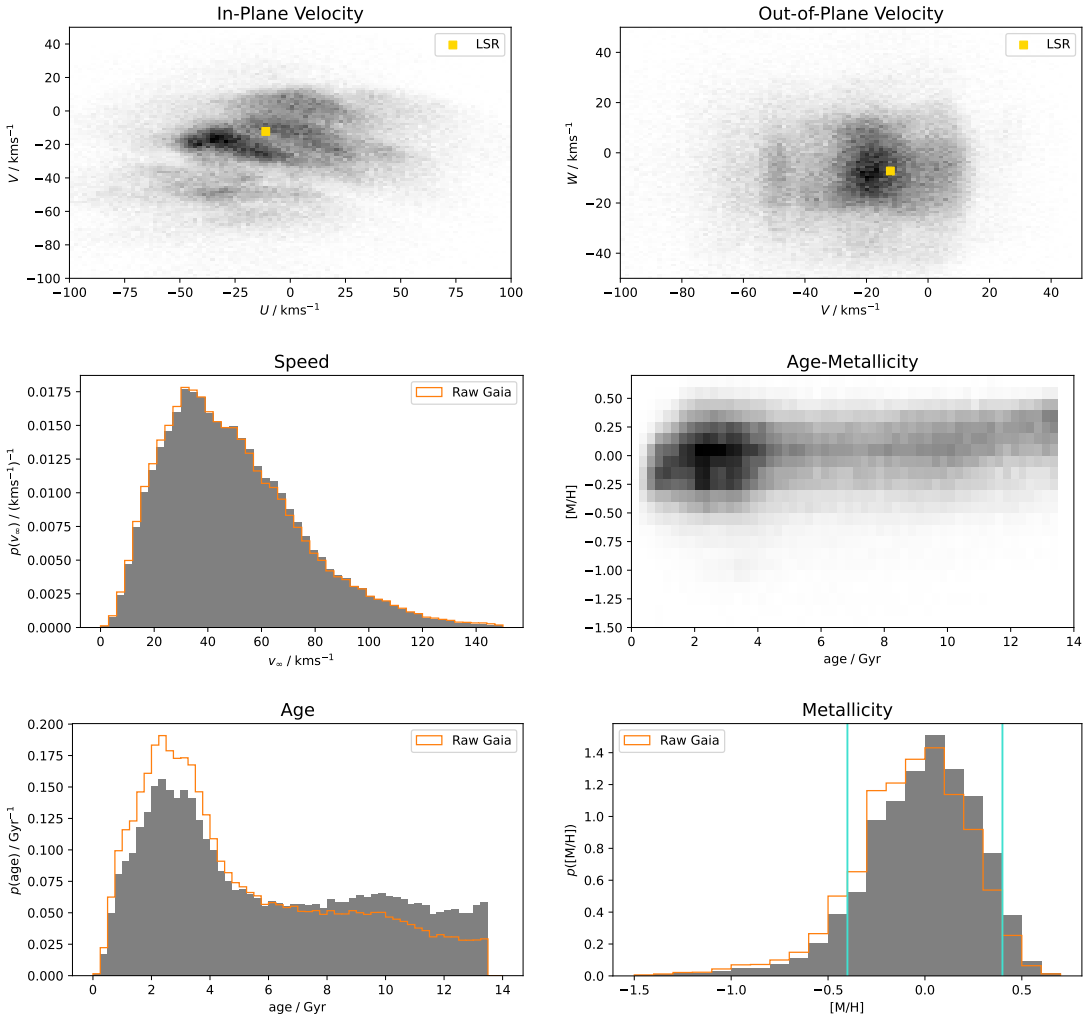

Figure 3.3: Distributions of the *sine morte* stellar population in velocity, age and [M/H]. U, V and W are the Cartesian components of stellar velocity in the Galactic frame, relative to the Solar System barycentre: U points towards the Galactic centre, V points in the direction of motion around the Galactic centre, and W points out of the Galactic plane. Both 1D and 2D histograms are normalised to integrate to unity. In orange unfilled histograms I have also plotted the distribution of the raw *Gaia* dataset, without accounting for selection effects or stellar death, for comparison. The vertical lines on the [M/H] distribution are the limits of the protoplanetary disk chemical model.

the stellar population of the solar neighbourhood: the flat age-metallicity relation described in §1.5.1, with a large scatter in metallicity at all ages, meaning stars of all metallicities are found at all ages (Fig. 3.3, Age-Metallicity). As noted in §1.5.1 this feature is surprising, as one would expect stellar nucleosynthesis and feedback to cause the metallicity of stars to increase over time and thus decrease with age, however it is attested in many surveys of stars (Edvardsson et al. 1993;

Haywood et al. 2013) as well as surveys of white dwarfs (Rebassa-Mansergas et al. 2021). The reason for the solar neighbourhood's flat age-metallicity relation is debated, with explanations including an inside-out formation of the Galactic disk with radial migration (Sellwood and Binney 2002; Schönrich and Binney 2009a), and a two-phase formation of the Galactic disk (Haywood et al. 2013).

3.2.5 Predicting the Interstellar Object Population

To predict the solar neighbourhood ISO distribution from the stellar distribution, I use a similar model and set of assumptions to Chapter 2. In that chapter I argued that the ISO spatial distribution would be similar to that of the *sine morte* stellar distribution, even though ISOs do not stay near their parent stars. The assumptions of the model are thus:

- The ejection of ISOs is slow ($\lesssim 10\,\mathrm{km\,s^{-1}}$, Hands et al. 2019; Pfalzner et al. 2021b; Albrow et al. 2024) relative to the orbital speed of stars around the Galactic centre ($220\,\mathrm{km\,s^{-1}}$, Bovy et al. 2012a). This means ejected ISOs are placed onto similar orbits to those of their parent stars, but with small velocity differences that cause them to disperse along these shared orbits and form kpc-scale streams (Forbes et al. 2024).

- However, the width of the stellar velocity distribution ($\sim 50\,\mathrm{km\,s^{-1}}$, Fig. 3.3) is significantly greater than the ISO ejection speed, meaning the stellar population mixes around the Galaxy far faster than ISOs disperse away from their parent stars. This means the stellar and ISO populations will mix at approximately the same rate.[10]

- Stars and ISOs are equally affected by the perturbing potentials which evolve their orbits, because compared to the spiral arms, bar and giant molecular

[10]This mixing is very well demonstrated by the video showing the orbits of a selection of stars from the Gaia Catalogue of Nearby Stars at https://www.cosmos.esa.int/web/gaia/edr3-gcns.

clouds, both stars and ISOs have equally negligible masses.[11] This means the orbits of stars and ISOs evolve at the same rate.

Taken together these mean that the population of ISOs on a given orbit can be predicted from the stellar population on that same orbit. Equivalently in my small solar neighbourhood volume, the population of ISOs with a given velocity can be predicted from the stellar population with that same velocity. Though these stars are largely not the parents of the ISOs passing through the Solar System, both are being sourced from the same parent stellar populations. Thus similarly to how we reweighted the *Gaia* dataset to estimate the solar neighbourhood *sine morte* stellar population, we can reweight the dataset again to predict the solar neighbourhood ISO population.

As argued in Chapter 2, since ISOs are expected to outlive their parent stars it is the *sine morte* stellar population on which the ISO population depends. Additionally since the vast majority of ISOs are expected to be released within several hundred Myr of a star's formation (Pfalzner and Bannister 2019; Lisse et al. 2022; Fitzsimmons et al. 2023), a delay significantly less than the average age of stars in the solar neighbourhood, I assume this offset is negligible and do not account for it.

As in Section 2.3.1, I map stellar metallicities to ISO compositions using a model based on the relationship of Bitsch and Battistini (2020) between a planetesimal's

[11] Two extended asides concerning these perturbing potentials: Firstly, I strongly expect the ISO velocity distribution to have the same pattern of moving groups and gaps as the stellar distribution. As discussed in Section 3.1 these are caused by the Galactic spiral and bar potentials clearing regions of velocity space corresponding to resonant orbits. Because individual stars and ISOs have masses equally negligible compared to the mass of the spiral arms or bar, resonances will affect the orbital distribution of ISOs equally to that of stars. Additionally, the spiral and bar may be transient on timescales of $\sim 100\,\mathrm{Myr}$ (Baba 2015), short compared to the lifetimes of both stars and ISOs. Though ejection from their parent systems could initially place ISOs on resonant orbits, the transient nature of the bar and spiral mean that the pattern of moving groups is continuously changing and the gaps between moving groups are continuously being cleared of both stars and ISOs equally. Secondly, dynamical heating will occur at the same rate for stars and ISOs as this is caused by interactions with giant molecular clouds (Gustafsson et al. 2016), compared to which both stars and ISOs again have negligible mass. Close encounters with individual stars don't contribute to the evolution of the orbits of either stars or ISOs as these are incredibly rare: stars and ISOs will undergo the same rate of close encounters with individual stars, and the timescale for an object with a speed of $50\,\mathrm{km\,s^{-1}}$ undergoing a 5 au-separation encounter with stars of density $0.1\,\mathrm{pc^{-3}}$ is $10^5\,\mathrm{Gyr}$. For a population of age $\sim 10\,\mathrm{Gyr}$, I would expect only 0.01% of ISOs (and stars) to have undergone such a close encounter. This is contrary to the claim of Feng and Jones (2018) that ISOs are rapidly scattered out of the Milky Way by close encounters with stars.

water mass fraction f_{H_2O} with their parent star's metallicity, assuming the dominant source of ISOs is the outer regions of protoplanetary disks (Fitzsimmons et al. 2023). Though the relation in Bitsch and Battistini (2020) correlates f_{H_2O} with [Fe/H], the relative abundance of iron specifically, this is well approximated by *Gaia*'s overall metallicity [M/H] for the thin-disk, non-alpha-enhanced majority of stars in the solar neighbourhood (Salaris and Cassisi 2005). This model predicts that the water mass fraction of planetesimals decreases with increasing metallicity within the range of validity, $-0.4 \leq [M/H] \leq 0.4$, corresponding to $0.07 \leq f_{H_2O} \leq 0.51$. Outside of this range, I assume that the relationship between f_{H_2O} and [M/H] continues to be monotonic, with f_{H_2O} remaining high beyond the low [M/H] limit and remaining low beyond the high [M/H] limit, as in Chapter 2, however in this Chapter I reproduce the result of Chapter 2 that the majority of ISOs lie within this range. I map the stellar metallicity of each star in my *Gaia* dataset to the corresponding ISO water mass fraction f_{H_2O}.

Since the mass of planetesimal-forming metals in a protoplanetary disk appears proportional to the metal fraction of its central star (e.g. Lu et al. 2020a), I assume that the number of ISOs produced by a star of a given metallicity [M/H] is proportional to $10^{[M/H]}$. I explored the sensitivity of the ISO population to the metallicity-dependence relationship in Sec. 2.4.2 showing that if there were no metallicity dependence, more high-f_{H_2O} ISOs would be present. As in Chapter 2 I am not concerned here with the absolute number of ISOs as this is highly unconstrained; instead I focus on the relative distribution of ISOs in velocity, composition and age. Thus to predict the distribution of ISO population from the *sine morte* population I additionally reweight the dataset points by a factor of $10^{[M/H]}$, as listed in Table 3.1. This distribution is plotted in Fig. 3.4.

3.2.6 Within the Solar System: The Volume Sampling Rate and Gravitational Focussing

The distribution of ISOs in the solar neighbourhood predicted in the previous section is different to the distribution of ISOs that is observable from our place in

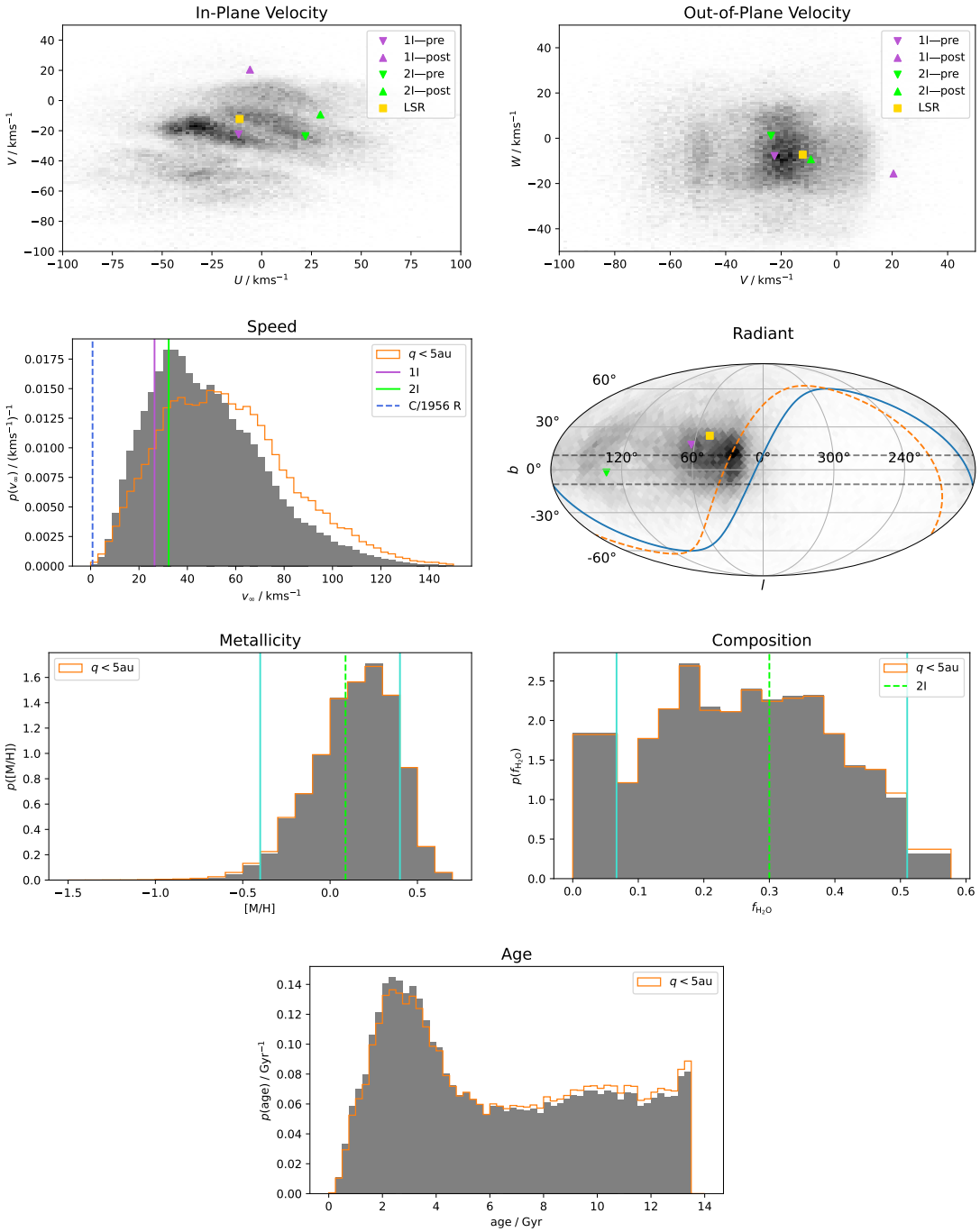

Figure 3.4: The solar neighbourhood ISO distribution, without including the volume sampling rate. The distribution of $q < 5\,\mathrm{au}$ ISOs of Figure 3.6 is included as an orange outline on the 1-D histograms for comparison—there is very little difference apart from the speed distribution.

the inner Solar System. ISO-detecting surveys such as Pan-STARRS (Chambers et al. 2016) and LSST have lifetimes significantly longer than the typical durations for which ISOs are visible: 1I and 2I spent only 2 months and 3 years respectively brighter than 24 mag, the LSST single-exposure r-band point source depth (Ivezić et al. 2019). Thus the population of ISOs close enough to be observed at any time is constantly being refreshed. This refreshing effect (previously discussed in Stern 1990; Moro-Martín et al. 2009) means that the distribution of ISOs that are observable is the distribution of those streaming through the inner Solar System, not the distribution of the static population in the solar neighbourhood of §3.2.5.

To model the observable population, I consider the distribution of the flux of ISOs through the Solar System on orbits with perihelia less than some value q. Being a flux, this distribution is proportional to relative speed $v_\infty = \sqrt{U^2 + V^2 + W^2}$, as faster ISOs flow into the observable volume at a proportionally higher rate. This flux is also proportional to the cross-sectional area $\sigma(q, v_\infty)$ for ISOs reaching perihelia less than q. This cross-sectional area is equal to the circular area πB^2 for the impact parameter B of an ISO with perihelion q and speed v_∞, related by $B = q\sqrt{1 + 2GM_\odot/qv_\infty^2}$ (see §4.3.2 for derivation). The increase of the cross section σ at low v_∞ at fixed q is called gravitational focussing (Whipple 1975; Seligman and Laughlin 2018; Forbes and Loeb 2019). These effects are combined in the volume sampling rate:

$$\gamma(q, v_\infty) = v_\infty \sigma = v_\infty \pi q^2 \left(1 + \frac{2GM_\odot}{qv_\infty^2}\right) \tag{3.1}$$

The volume sampling rate is plotted in Fig. 3.5, scaled by $1/\pi q^2$, the geometric cross section. Multiplying the velocity distribution of ISOs in the solar neighbourhood by $\gamma(q, v_\infty)$ gives the flux of ISOs with perihelion less than q into the Solar System. Modelling the observable population by this streaming population with some cutoff in perihelion is a simplification that ignores the distribution of sizes and thus maximum observable distances ISOs can have, however I tackle this problem more completely in Chapter 4.

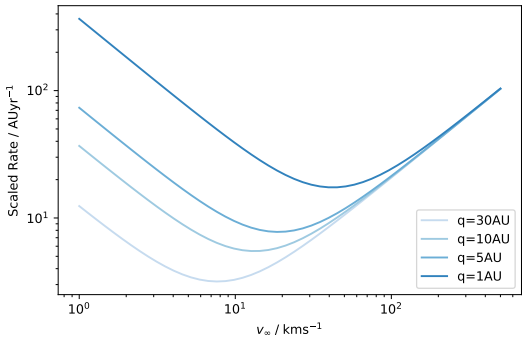

Figure 3.5: Volume sampling rate scaled by $1/\pi q^2$ for different perihelia q. This is the combination of gravitational focussing, which increases the sampling rate of low relative speed ISOs, and the "refresh rate" effect, where faster ISOs are sampled at proportionally higher rates.

Though the volume sampling rate becomes proportional to v_∞^{-1} at low speeds, it is unnecessary to apply a cutoff or gravitational softening. This is because the velocity distribution remains integrable due to the v_∞^2 Jacobian factor that arises from the velocity distribution being three-dimensional. Thus the one-dimensional speed distribution (Fig. 3.6, Speed) becomes proportional to v_∞ at small speeds, and does not diverge. I find adding a gravitational softening parameter $\phi = 2\,\mathrm{km\,s^{-1}}$ (as done by Seligman and Laughlin 2018) does not significantly change the likelihoods calculated in §3.4.3 or any other of my results.

To predict the distribution of the flux of ISOs into the Solar System, similar to Sections 3.2.3 and 3.2.5 I yet again reweight the dataset; here I add a factor of $\gamma(q, v_\infty)$ to the solar neighbourhood ISO distribution, principally with $q = 5\,\mathrm{au}$ as this is the distance at which cometary objects can be detected and characterised. The weights applied to the raw *Gaia* samples to get each distribution are summarised in Table 3.1.

3.2.7 Known Objects

My comparison sample is the two currently known macroscopic interstellar objects: 1I/'Oumuamua and 2I/Borisov. For a more comprehensive description of their observation and characterisation, see §1.2 and §1.3

Distribution	Weight
Raw *Gaia* Dataset	1
Sine Morte Stars	$\frac{1}{\mathrm{ESF}}$
Solar Neighbourhood ISOs	$\frac{10^{[\mathrm{M/H}]}}{\mathrm{ESF}}$
$q < 5\,\mathrm{au}$ ISOs	$\frac{10^{[\mathrm{M/H}]} \cdot \gamma(5\,\mathrm{au}, v_\infty)}{\mathrm{ESF}}$

Table 3.1: Summary of weights given to *Gaia* dataset to estimate different stellar and ISO distributions. The effective selection function (ESF) is a function of each *Gaia* sample's distance, age, metallicity and on-sky position.

Both known ISOs were measured for sufficiently long arcs that their original orbits are well constrained; Bailer-Jones et al. (2018) and Bailer-Jones et al. (2020) additionally integrate the orbits of 1I and 2I respectively with a selection of non-gravitational acceleration models to estimate each pre-encounter velocity and their uncertainties. For both objects the differences in the pre-encounter velocities between the different non-gravitational acceleration models are negligible, so for 1I I choose the $2k = 2$ solution of Bailer-Jones et al. (2018) and for 2I I choose solution 47 of Bailer-Jones et al. (2020). For the post-encounter asymptotic velocity, I use the full observed arc orbits of JPL Horizons[12].

3.3 Results

3.3.1 Interstellar Object Distribution

Figure 3.6 shows the predicted distribution of $q \leq 5\,\mathrm{au}$ ISOs entering the Solar System in two-dimensional velocity, speed, on-sky radiant, composition, source stellar metallicity and age. I have chosen to focus my discussion on the distributions of $q \leq 5\,\mathrm{au}$ ISOs as this is indicative of the distance at which cometary objects can

[12]Solar System Dynamics. (Downloaded 2023-12-20). 1I: https://ssd.jpl.nasa.gov/tools/sbdb_lookup.html#/?sstr=1I, solution as of 2018-Jun-26 12:17:57; 2I: https://ssd.jpl.nasa.gov/tools/sbdb_lookup.html#/?sstr=2I, solution as of 2020-Aug-21 09:32:58.

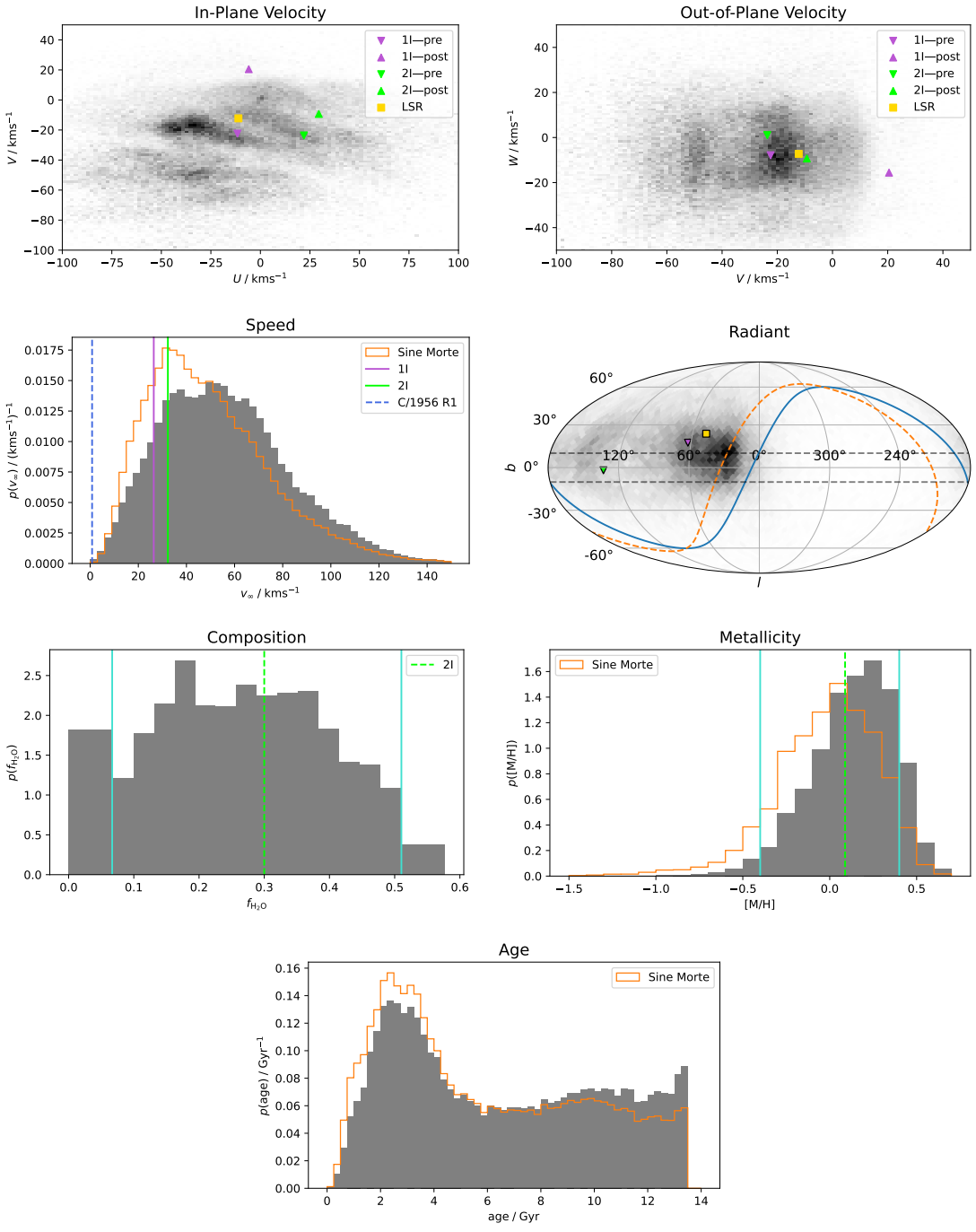

Figure 3.6: Predicted distributions of ISOs with $q < 5\,\mathrm{au}$ in velocity, on-sky radiant, composition proxied by water mass fraction $f_{\mathrm{H_2O}}$, parent-star metallicity and age, analogous to Fig. 3.3. On the radiant plot the ecliptic plane is marked in solid blue, the celestial equator is marked in dashed orange, and dashed horizontal lines encapsulate the $b = \pm 10°$ region of high stellar density along the Galactic plane. Orange unfilled histograms plot the distribution of the *sine morte* stellar population for comparison.

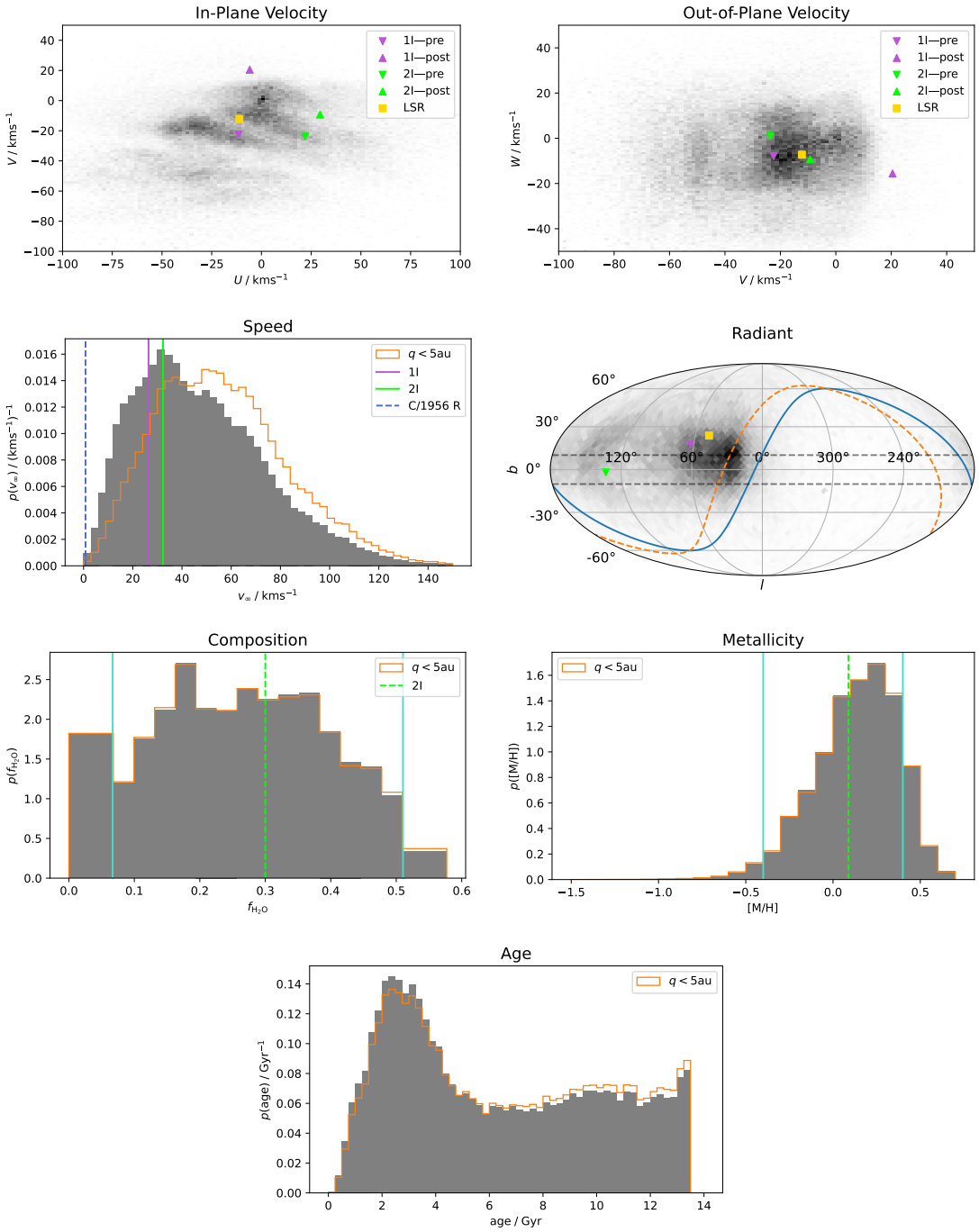

Figure 3.7: Same as Fig. 3.6 but for ISOs with $q < 1$ au, with orange unfilled histograms plot the distribution of the $q < 5$ au ISO population for comparison.

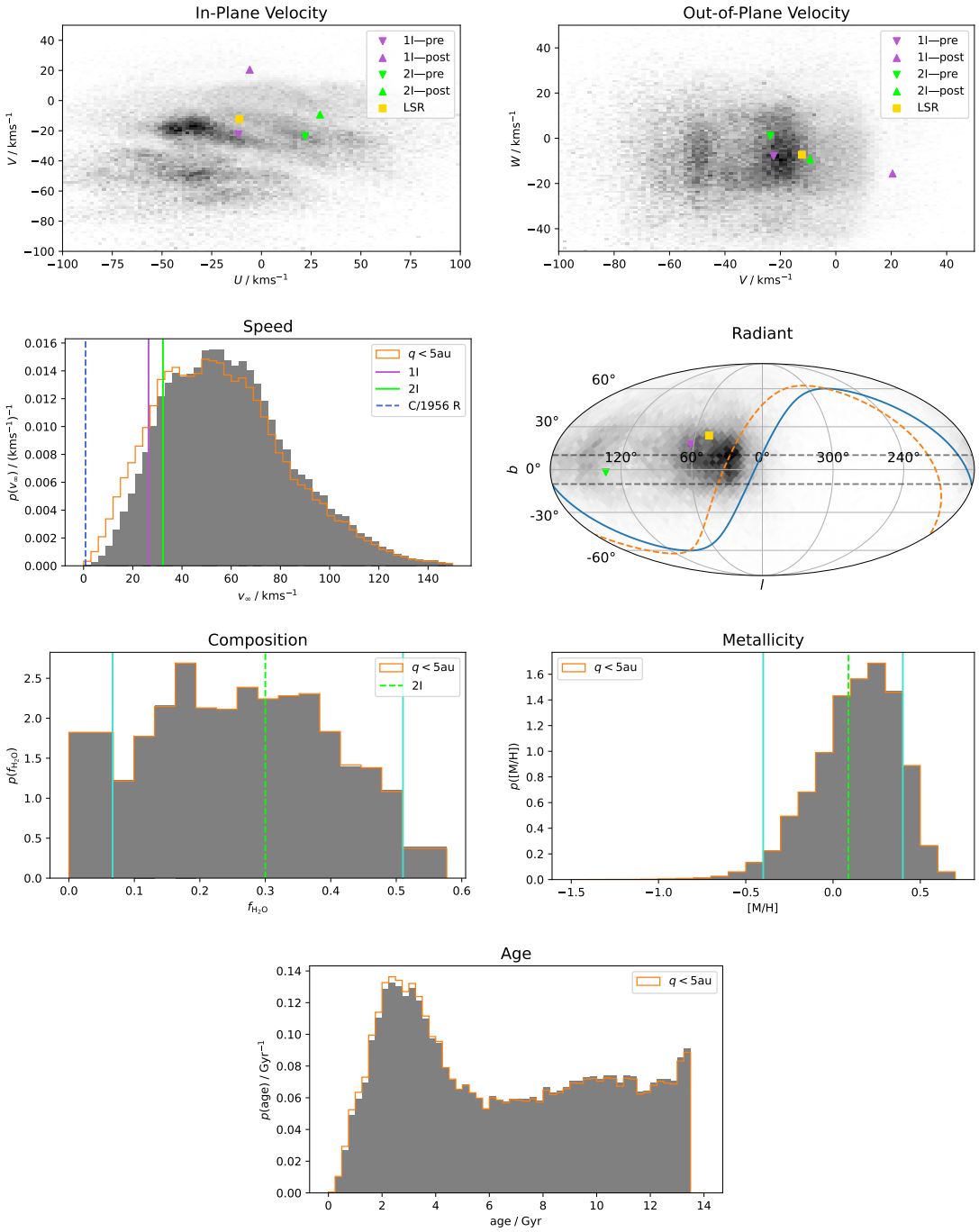

Figure 3.8: Same as Fig. 3.6 but for ISOs with $q < 30\,\mathrm{au}$, with orange unfilled histograms plot the distribution of the $q < 5\,\mathrm{au}$ ISO population for comparison.

be detected and characterised, for comparison however I also plot the distributions of ISOs with $q \leq 1\,\mathrm{au}$ in Figure 3.7 and $q \leq 1\,\mathrm{au}$ in Figure 3.7.

I first consider the velocity distribution of ISOs in their Cartesian components U, V and W in two two-dimensional histograms (Figure 3.6, In-Plane Velocity and Out-of-Plane Velocity). As expected given that stars are the progenitors, under my model in §3.2.5 the ISO velocity distribution shows the same moving groups and branches as the stellar distribution of Figure 3.3. Many ISOs will have pre-encounter velocities in these structures: I predict 18% of ISOs passing through the inner Solar System will originate in the largest of these, the Hyades-Pleiades branch[13]. However, the ISOs display an additional peak at the Solar System barycentre velocity $(U, V, W = 0, 0, 0)$ when compared to the stellar distribution due to gravitational focussing, discussed in §3.2.6 and illustrated in Fig. 3.5. Comparing to Figures 3.7 and 3.8, the effect of gravitational focussing becomes more pronounced as the perihelion cut decreases; by $q = 30$ au, there is effectively no gravitational focussing. As in Fig. 3.3, I mark with a yellow square the local standard of rest (LSR; Schönrich et al. 2010), the indicative velocity of a star on a circular orbit in a theoretical azimuthally-smoothed Galactic potential at the distance from the Galactic centre of the Sun.

To compare this predicted population with the known sample of detected interstellar objects, I indicate in Figure 3.6 the Cartesian component velocities of 1I/'Oumuamua and 2I/Borisov both before and after their perturbing interaction with the Solar System (Section 3.2.7): 1I is marked in purple and 2I in green. The pre-encounter velocities are directly comparable to my predicted population; the post-encounter velocities are to illustrate the effects of the only two measured ISO gravitational interactions with the Sun. Both known ISOs' pre-encounter velocities are entirely typical for the population, occurring in regions of velocity space with relative ISO abundance. This places both ISOs within moving groups in velocity space; I discuss the implications of this in §3.4.1.

I next consider the asymptotic speed v_∞ distribution of ISOs. Fig. 3.7 (Speed), for $q < 1\,\mathrm{au}$ ISOs, can be directly compared to the speed distribution predicted

[13]defined here with boundaries $V < -5\,\mathrm{km\,s^{-1}}$, $U > -55\,\mathrm{km\,s^{-1}}$, $V > -35\,\mathrm{km\,s^{-1}} - 0.2U$, and $V < -25\,\mathrm{km\,s^{-1}} - 0.6U$, following Fig. 5 of Antoja et al. (2008).

by Eubanks et al. (2021); they are similar, with my prediction of a median v_∞ of $45\,\mathrm{km\,s^{-1}}$ for $q < 1\,\mathrm{au}$ ISOs being slightly higher than Eubanks et al. (2021)'s $38\,\mathrm{km\,s^{-1}}$. This difference is due to my model weighting the ISO contribution of stars proportionally to their metal fraction (Sec. 3.2.5). Figures 3.7 and 3.8 (Speed) show the effect of sequentially less gravitational focussing for $q < 55\,\mathrm{au}$ and $q < 530\,\mathrm{au}$ respectively. Each of these distributions are shifted to higher values of v_∞, with the median v_∞ of $q < 55\,\mathrm{au}$ ISOs being $55\,\mathrm{km\,s^{-1}}$.

I mark the asymptotic speeds of 1I, 2I, and an example hyperbolic Solar System comet C/1956 R1 (Arend–Roland) on Figure 3.6 (Speed). Long-period comets are regularly discovered on weakly hyperbolic orbits but are not thought to be interstellar, instead originating in the weakly-bound Oort Cloud and being perturbed by gravitational interaction with the giant planets onto unbound orbits. Some of these hyperbolic comets without an obvious prior interaction with a giant planet have been considered as potential interstellar objects, including C/1956 R1 (Sekanina 1968), however I can use my predicted v_∞ distribution to demonstrate that this is unlikely. While the asymptotic speeds of 1I and 2I are clearly feasibly drawn from the distribution plotted in Figure 3.6 (Speed), my predicted distribution gives a p-value of 10^{-5} for an ISO having a speed relative to the Sun lower than that of C/1956 R1, making this comet's Solar System origin significantly preferred. This reproduces a result of Whipple (1975)[14], who gave an analytic expression for this probability assuming a Gaussian velocity distribution and determined its value to lie in the range 2×10^{-7} – 1×10^{-4}.

The radiant is the direction of approach of an ISO on its way into the Solar System, and is equal to the angular direction of its velocity vector relative to the Sun. This is plotted in Galactic longitude and latitude l and b in Fig. 3.6 (Radiant). Due to the motion of the Sun relative to the average stellar velocity, the predicted radiant distribution clusters near the Solar apex, marked here by the same yellow square, as expected (e.g. McGlynn and Chapman 1989; Stern 1990; Seligman and Laughlin 2018). This is computed as the direction of the velocity vector of the

[14]this work refers to C/1956 R1 as 1957 III.

Sun relative to the LSR of Schönrich et al. (2010). Since gravitational focussing increases the rate of ISOs that have velocities similar to that of the Sun entering the inner Solar System in an isotropic manner, it has the effect of decreasing the proportion of ISOs with radiants near the apex.

I can now consider the physical properties of the ISOs themselves. Here my example property, as in Chapter 2, is ISO water mass fraction f_{H_2O}. It should be noted that this distribution is for ISOs which formed outside the water ice line only, however as discussed in §3.2.5 I expect this to be true for most ISOs. The distribution of water mass fraction of the ISOs entering the inner Solar System within the range of the Bitsch and Battistini (2020) chemical model is shown in Figure 3.6 (Composition). The overall distribution is broad, and matches my predictions using APOGEE data in Chapter 2. For reference, the inferred water mass fraction of 2I/Borisov, the only ISO with this property somewhat constrained from production rates, is marked by a vertical green line (Seligman et al. 2022). I discuss composition further in §3.3.2.

The age distribution of ISOs entering the inner Solar System (Figure 3.6, Age) is very similar to that of the *sine morte* stellar population. There are a couple of effects which could cause these to differ, however neither end up having a large effect. Firstly, stars are observed to show a correlation between their ages and velocity dispersions (e.g. Nordström et al. 2004) and a similar correlation in ISOs would cause older, faster moving ISOs to cross the Solar System more often and be more-highly-weighted by the volume sampling rate (Eq. 3.1), shifting the ISO distribution towards higher ages. This does occur and can be seen in Fig. 3.4 (Age), though the effect is small. Secondly, as discussed in §3.2.4, the solar neighbourhood has a flat age-metallicity relation meaning that even if ISO production correlates with metallicity as I assume, there are high-metallicity, high-ISO-production stars at all ages and the ISO and stellar age distributions will remain very similar. ISOs of all ages are passing through the Solar System: while there is a peak at 3 Gyr, I predict the ISO age distribution will be sampled quite evenly from stars across the age of the Galaxy.

Finally, I also include the distribution of the metallicities of the parent stars of the ISOs entering the inner Solar System (Figure 3.6, Metallicity). This tends towards higher metallicities than the overall stellar distribution. This outcome is due to the metallicity dependence that I apply to my ISO production (§3.2.5): since in my model higher [M/H] stars produce more ISOs, more ISOs come from higher [M/H] stars. On this distribution I have plotted the value of [M/H] corresponding to 2I's water mass fraction of 0.3, showing that for this physical property value, 2I would have come in my model from a star of metallicity [M/H] ≈ 0.1.

I can also now see the stellar origin of the ISOs on either side of the range of the planetesimal composition model. Though I cannot measure the distribution of ISOs in f_{H_2O} outside of the boundaries of the chemical model (marked by vertical turquoise lines), I can still quantify the fraction of ISOs on either side. I show the contribution to the distribution below the range in a bin covering $f_{H_2O} = 0$ to the lower limit $f_{H_2O} = 0.07$, and above the range in a bin of the same width ($f_{H_2O} = 0.51$ to $f_{H_2O} = 0.58$). The bin above the range of the chemical model has a low density, showing the f_{H_2O} distribution only extends a little above the range that I can measure. On the other hand, the bin below the lower limit of the chemical model has a high density, meaning the composition distribution must have a second peak in this bin, even if it is outside of the range of my model. A tiny number of ISOs come from stars with metallicities below the lower limit, whereas a more significant number come from stars with metallicities above the upper limit. As in the principal prediction in Chapter 2, extremely metal-poor stars contribute almost no ISOs to the Solar System neighbourhood.

3.3.2 Chemodynamics

Stars in the Milky Way exhibit correlations between composition and dynamics, so I expect ISOs with varied compositions to also have different velocity and age distributions. As noted in §1.5.1, the Galactic stellar population is loosely grouped into a high-metallicity, low-velocity-dispersion, low-age 'thin disk' and a low-metallicity, high-velocity-dispersion, high-age 'thick disk' (Recio-Blanco et al. 2014). To explore

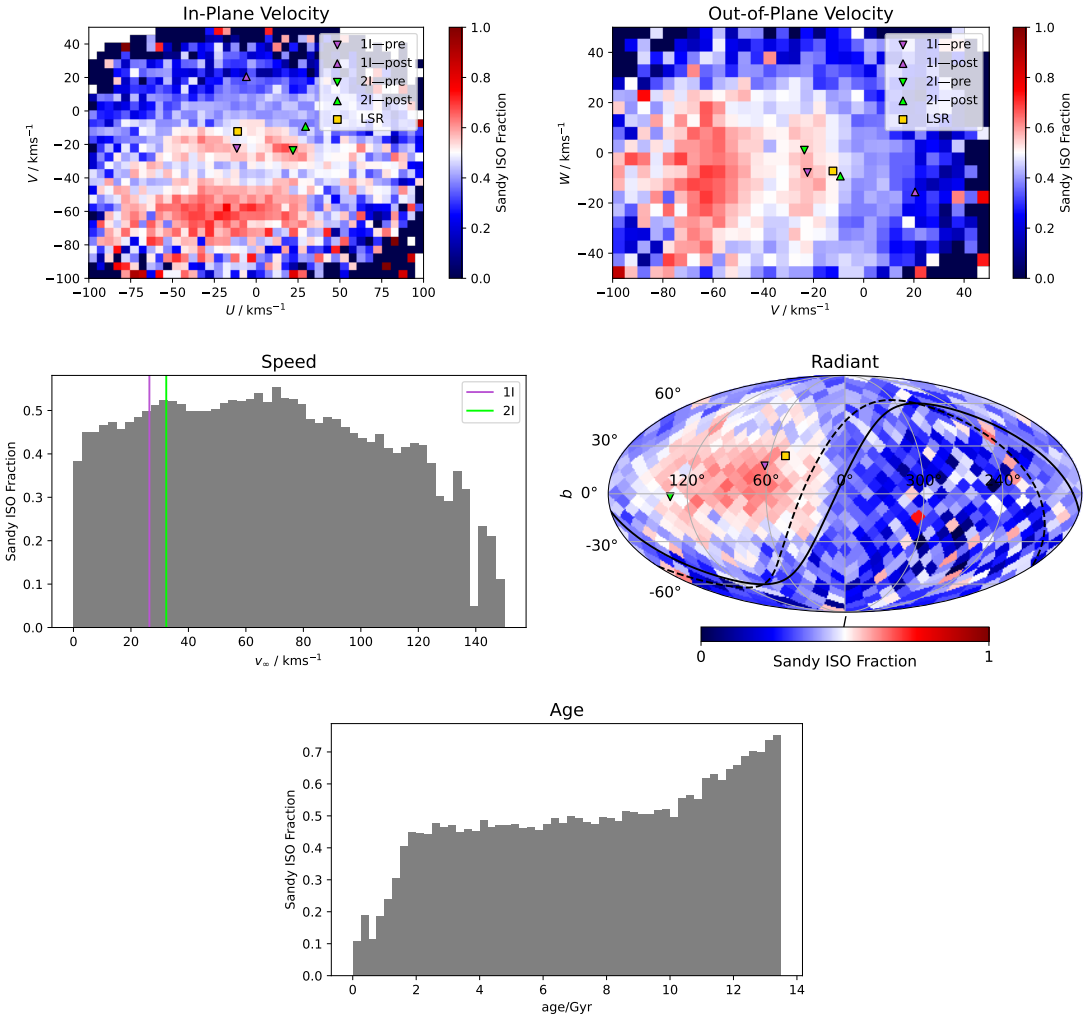

Figure 3.9: Fraction of $q < 5$ au ISOs at each velocity, radiant and age that are 'sandy' ($f_{H_2O} < 0.25$). Sandy ISOs form the majority in moving groups and low V, and at higher ages.

these correlations in the ISO population, I split my predicted ISO distribution in half by water mass fraction, relative to the median $f_{H_2O} = 0.25$. For ease of reading, I term these two groups 'sandy' ($f_{H_2O} < 0.25$) and 'frosty' ($f_{H_2O} > 0.25$).

Since ISO water mass fraction decreases monotonically with parent star metallicity, frosty ISOs originate from *low* metallicity stars, with [M/H] < 0.16, and sandy ISOs originate from *high* metallicity stars, with [M/H] > 0.16. For example, 2I would fall in the $f_{H_2O} > 0.25$ frosty group. The plots in Fig. 3.9 show the fraction of ISOs at each velocity, radiant and age that are sandy. Notably sandy ISOs, like the high metallicity stars they originate from, are preferentially found in the

moving groups (compare Fig. 3.6 and Fig. 3.9, In-Plane Velocity) with the sandy ISO fraction greater than 0.5 signifying that they make up the majority.

Conversely, frosty ISOs are much more continuously distributed, and are in the majority at higher speeds relative to the Sun. This difference is most clear in the radiant plot, which shows that the majority of ISOs entering the inner Solar System near the Solar apex will be sandy, whereas ISOs on other trajectories will be predominately frosty. Additionally, the age distribution changes between the two populations, with the sandy distribution being weighted towards older ISOs than the frosty population. This is a product of the presence of old high-metallicity stars in the solar neighbourhood (see Fig. 3.3, Age-Metallicity). Less notably, both sandy and frosty ISOs are found at all values of v_∞, with a slight preference for frosty ISOs at higher speeds.

3.4 Discussion

The correlations I show in §3.3 in my chemodynamical distribution mean that substantial information about the origin of an ISO can be inferred from its velocity alone. The conditional distribution of ISO compositions, parent-star metallicities and ages depends on the given velocity. That is, even if I only know the velocity of an ISO, I can still calculate the probability distribution its composition, parent-star metallicity and age must have been drawn from. These correlations will allow us to make inferences about partially characterized ISOs found in future surveys. My approach could also be used to constrain the origin of more exotic ISOs found in future: if an object were not described well by my current chemical model, e.g. an icy fractal aggregate (Moro-Martín 2019), I can still use my distribution to constrain the metallicity of its home star.

Velocity is one of the first parameters that can be measured for a new-found small body: for an ISO, with its comparatively high velocity relative to Solar System objects, it is quantifiable with a relatively short orbital arc, e.g. 4-7 days for LSST (Cook et al. 2016). The *Gaia*-based v_∞ distribution I present in Fig. 3.6 can be used for testing both future ISO discoveries and known Solar System comets that

have been hypothesised to have interstellar origins (e.g. as with C/1956 R1 in §3.3). From Fig. 3.6, the uncertainties on the velocities of discovered ISOs will need to be $\lesssim 5$ km/s for their velocity distribution identification to be crisp, as this is approximately the scale of the moving groups.

Perhaps the most striking feature of my results is that local ISOs are indeed coming from stars of all ages in the Galaxy, counter to several claims made in the wake of the discovery of 1I/'Oumuamua which I discuss in Sec. 3.4.1. This wide age distribution is a natural outcome, given the wide stellar age distribution and the fact that ISOs outlast stars. This is due to radial migration; stars currently in the solar neighbourhood have origins over a large range in Galactic radius (Sellwood and Binney 2002; Lian et al. 2022a). Stars mix even faster azimuthally, as discussed in §3.2.5. This means stars that happen to currently be nearby have in fact been sourced from all over the Galactic disk.

The result is that the population of stars and therefore ISOs currently near the Sun at any particular velocity is a dynamic mix of many different populations, sourced from all ages and a large swath of the disk. There are however correlations, for instance younger stars which have more circular orbits on average (Nordström et al. 2004) are more affected by resonances (Daniel and Wyse 2015), and so end up in moving groups more frequently. Unlike in purely stellar studies, in addition to remote observational study with telescopes ISOs have the potential for ground truth by spacecraft visits, such as with *Comet Interceptor* (Jones et al. 2024). My prediction of the broad age spread of ISOs would be testable with detailed isotopic ratios and compositions obtained by sample return missions either from the comae (e.g. *Stardust*, Brownlee et al. 2003) or surface (e.g. *Hayabusa*, Fujiwara et al. 2006).

3.4.1 Origins of the Two Known ISOs

As seen in Fig. 3.6, the pre-encounter velocities of 1I and 2I both lie within the boundaries of particular overdensities in velocity space, called moving groups. These overdensities are caused by resonances with the Galaxy's transient spiral arms and

bar clearing gaps in the U—V plane (Skuljan et al. 1999), local manifestation of kpc-scale Galactic dynamical structures (Ramos et al. 2018).

The overdensity 1I/'Oumuamua's velocity resided in is called the Pleiades moving group (Zhao et al. 2009), part of the Hyades-Pleiades branch (Skuljan et al. 1999), named after the Pleiades open cluster (M45) that it contains. The Pleiades *moving group* is distinct from the Pleiades *open cluster*, so to avoid confusion, I use the te reo Māori name for the open cluster: Matariki (Mātāmua 2020). The age distribution of members of the Pleiades moving group is non-coeval (Antoja et al. 2008): this crucial point means that the overdensity in velocity space we observe here is not just the dispersal of Matariki, which is made up of recently-formed, coeval stars. Additionally, Heyl et al. (2022) counts only ~ 1500 members of Matariki including escapees, but Lucchini et al. (2023) find $\sim 150\,000$ stars belonging to the Pleiades moving group. 1I/'Oumuamua's pre-encounter velocity made it a member of of the Pleiades moving group, but this does not imply formation around a star in Matariki, or at a star of one of the other young stellar associations that happen to be currently nearby and have similar velocity. I emphasize this distinction because a nearby origin for 1I has been erroneously claimed by numerous works, e.g. Gaidos (2018), Feng and Jones (2018) and Hsieh et al. (2021) resulting in the pervasive perception that the 1I or the majority of ISOs are expected to have formed around nearby stars, appearing in reviews such as Jewitt and Seligman (2023).

1I/'Oumuamua's pre-encounter velocity lies relatively near the local standard of rest (LSR), within $\sim 10\,\mathrm{km\,s^{-1}}$, with only 2% of my predicted ISO distribution having a velocity closer than this. However, Fig. 3.6 (In-Plane Velocity) shows that the exact velocity of the LSR is not a preferred point in the local velocity distribution. In particular, the structure of the branches mean there is a natural gap between the LSR and 1I/'Oumuamua's velocity. It is therefore not appropriate to attribute significance to the proximity of 1I to the LSR as though the velocity distribution were a Gaussian centered on the LSR. I predict that as the sample of known ISOs increases, until 50 ISOs are known it is most likely that 1I/'Oumuamua will remain the closest to the LSR.

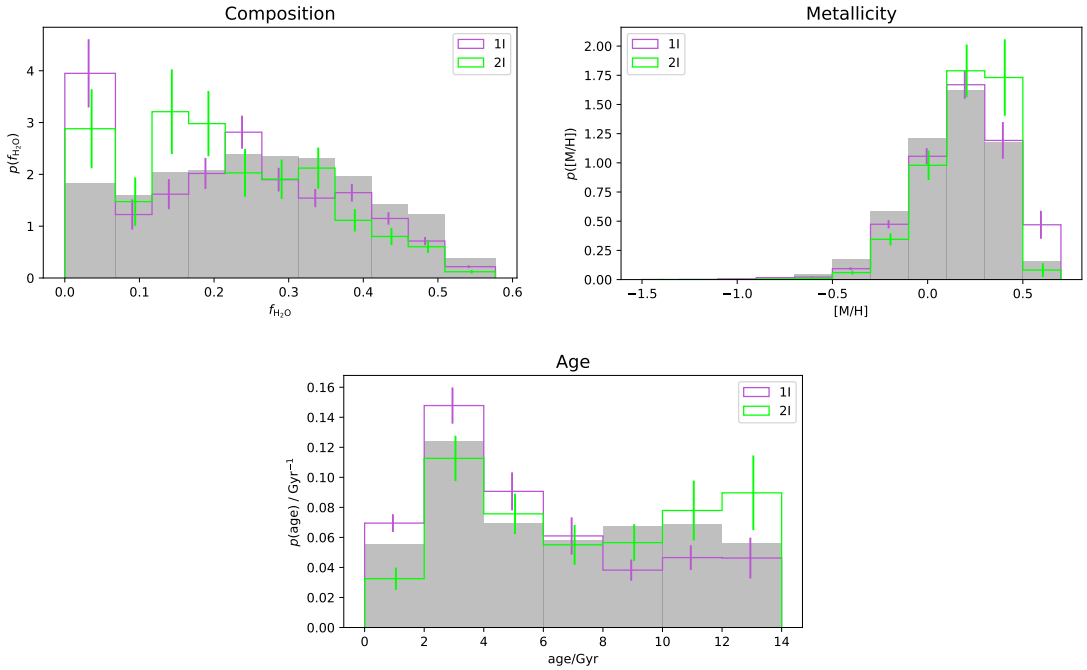

Figure 3.10: Predicted distribution of ISOs with similar velocity to 1I and 2I in composition, age and [M/H]. For comparison, the overall ISO population distribution in Fig. 3.6 is also shown, in grey.

2I/Borisov was a member of the Coma Berenices moving group (See Fig. 5 of Antoja et al. 2008) before its Solar encounter. This moving group is named after but distinct from the constellation Coma Berenices. Similarly, it does not represent the origin of 2I, only a transient location in velocity space caused by the clearing of gaps by orbital resonances with the transient spiral and bar potentials.

3.4.2 Inference from Velocity

I can use the correlations of an ISO's other properties with velocity to make inferences about the distributions that an ISO's composition, parent-star metallicity and age must be drawn from. For ISOs discovered in the future, this means inferences can be made about their other properties based only on their velocity, which is easiest to constrain. Here I explore what can be inferred about 1I and 2I based only on their velocities.

I do this by evaluating the composition, parent-star metallicity and age distribution of 1I and 2I using only points in the *Gaia* dataset with velocities within

$5\,\mathrm{km\,s^{-1}}$ of each ISO's pre-encounter velocity; these are plotted in Figure 3.10. Setting $5\,\mathrm{km\,s^{-1}}$ is a relatively arbitrary bound that provides a suitably large restricted sample (793 observed stars for 1I and 255 observed stars for 2I); since it is smaller than the overall sample, to ensure the differences in the histograms are significant, I calculate error bars for the value of the distribution in each bin. As this is a weighted sum, the variance in the estimated distribution is equal to the sum of the squared weights in each bin.

As a method of estimating the age distribution, this is similar to the approach used by Almeida-Fernandes and Rocha-Pinto (2018a), who inferred a confidence interval on the age of 1I from its velocity using a model of the stellar age-velocity distribution. They estimate 1I's age as 200 Myr–450 Myr. However, their analysis uses a smooth Gaussian distribution for the stellar velocity distribution, which Fig. 3.6 shows is not representative, and their result is dependent on the model used for the age-velocity dispersion relation.

My method however uses the actual measured age distribution of stars with similar velocities to the ISO being considered. As noted in Section 3.2.1, these ages are measured in the *Gaia* FLAME pipeline by fitting isochrone stellar models to atmospheric parameters derived from the measured RVS spectra. In comparison to literature ages Fouesneau et al. (2023) finds FLAME ages to have mean biases of only 0.1 Gyr to 0.3 Gyr and dispersions of 0.25 Gyr, however determining ages by isochrone fitting can be prone to bias (Nordström et al. 2004). Additionally, my distributions in Fig 3.10 are from samples with a large extent in space (a sphere of radius 200 pc). In future, more accurate predictions of the known ISOs' distributions could be achieved by using observed stars with both similar velocity and position.

I find that at the velocities of both 1I and 2I there are ISOs with a wide range of ages and compositions, and the distributions for both generally follow those of the overall population. This is due to the mixing described above: at any particular velocity there are stars with a wide range of ages and metallicities. However, the correlations with velocity cause some notable differences. Chemically, the distributions for both ISOs are shifted towards lower $f_{\mathrm{H_2O}}$ and higher parent-star

metallicities. In age, the distribution for both ISOs is broad, but 1I is shifted towards lower values, and 2I towards higher values. This is expected from the relative speeds of 1I and 2I to the LSR given that younger stars have generally lower velocity dispersions than older, but it is important to note that stars of all ages can be found at the velocities of both ISOs. This is backed up by previous studies showing that the Pleiades moving group is made up of stars of all Galactic ages (Famaey et al. 2008; Antoja et al. 2008). Thus these results suggest that 1I is not necessarily young.

3.4.3 Model Testing by Future Surveys Such as LSST

The LSST is going to find a large sample of ISOs, although the exact number has a large uncertainty, discussed further in Chapter 4. Here I explore the ability of the LSST ISO sample to test models by predicting the number of ISO discovereies required to distinguish models of velocity distribution. Note that I am not yet incorporating the actual on-sky performance of LSST or any other survey; surveys provide actual detections with a complex efficiency function, the modelling of which I discuss in Chapter 4.

I compare a series of models: my Gaia model, and the Schwarzschild velocity distributions fit to M-, G- and OB-type giant stars used by Hoover et al. (2022) and (Marčeta 2023). The Schwarzschild distribution is a multivariate Gaussian velocity distribution inclined in the U-V plane by vertex deviation angle l_v; the parameters used by Hoover et al. (2022) and Marčeta (2023) are listed in table 10.3 of Binney and Merrifield (1998), copied from Delhaye (1965) but ultimately sourced from Parenago (1951). As discussed in Section 3.1, it has been known for a quarter century that the stellar velocity distribution is poorly described by a Gaussian. Thus I expect my distribution, drawn directly from the latest data, to be a much more accurate description of the ISO velocity distribution compared to those of Hoover et al. (2022) and Marčeta (2023). I calculate the number of ISOs needed to be observed in order to distinguish the realistic, featured velocity distribution I predict from a smooth Gaussian.

As described in §1.6, a predicted distribution of interstellar objects can be used as a likelihood function to perform inference. I calculate the likelihood function for the Gaussian velocity distributions with a $q \leq 5\,\mathrm{au}$ volume sampling rate by normalising the product of the Gaussian probability density function and the volume sampling rate of Eq. 3.1. I estimate the likelihood function of my *Gaia* model with a k-nearest neighbours method, based on that of Zhao and Lai (2020): at each given velocity I sum the normalised $q < 5\,\mathrm{au}$ ISO weights of the 99 nearest neighbouring points in my Gaia dataset, divided by the volume of a sphere in velocity space with radius out to the 100th nearest neighbour. Slices though the resulting likelihood function are shown in Fig. 3.11; they match the 2D histograms of Fig. 3.6 as expected.

For a given sample of observed ISOs, the likelihood of different velocity distribution models producing the observed velocities can be calculated and compared to determine the more-likely model. I draw samples of size N from each model velocity distribution, then calculate the log likelihood of each sample being drawn from each other model. Repeating this with new samples, I calculate the mean and standard deviation of the log likelihood of each sample being drawn from each model. A sample should have the largest log likelihood with the true model it was drawn from, and lower likelihoods with the alternate models. Large discrepancies between the true and alternate models will allow the alternate models to be rejected. I calculate the significance of each discrepancy for each sample size N and list them in Table 3.2. This is equivalent to a series of relative likelihood tests (Akaike 1974).

Positing that most realistic distribution of ISOs is what I have predicted, I focus on the significances of the *Gaia* model samples relative to the other models. I find that at $N = 50$, a 3σ discrepancy with the OB-type Schwarzschild distribution is detectable. This is because this distribution has the lowest velocity dispersions, far lower than those of the overall stellar population, making it the most different to my *Gaia* sample. Dropping the sample to $N = 20$ still reaches a discrepancy of significance 2σ to the OB-type model. At a larger but still reasonable sample size of $N = 100$, the discrepancy between my *Gaia* sample and the OB-type model exceeds the 5σ level. The G-type model reaches 2σ at $N = 50$. The discrepancy between my

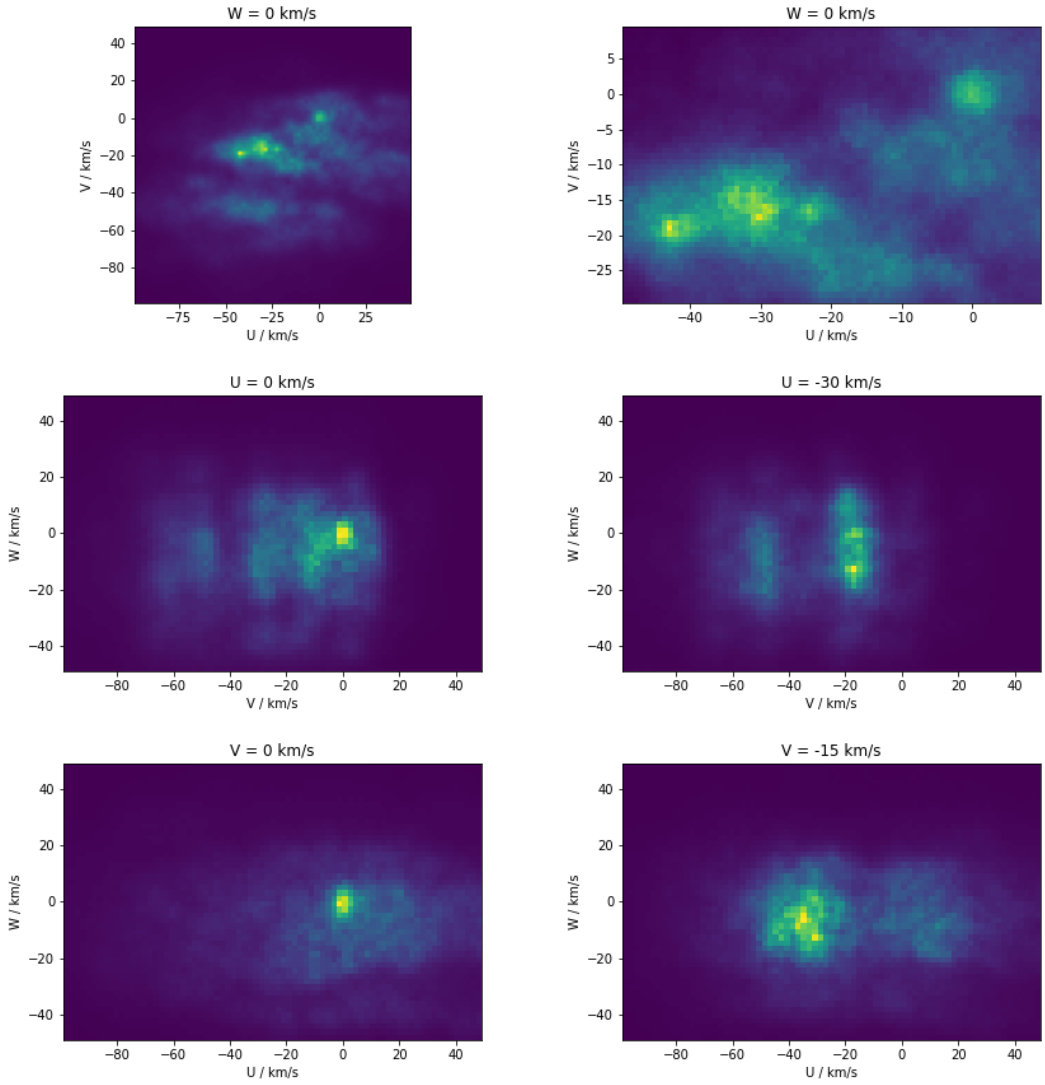

Figure 3.11: Slices through the continuous 3D velocity distribution of $q < 5\,\mathrm{au}$ ISOs, calculated with the kNN method described in the text. Slices through the Sun's velocity $(U, V, W = 0, 0, 0)$ show a peak caused by gravitational focussing not present in other slices.

Gaia sample and the M-type model is the lowest of the three Schwarzschild models because this model has the largest velocity dispersions, and is the closest match to my *Gaia* distribution. To reach a 2σ level discrepancy between the featured *Gaia* model and the M-type Schwarzschild model, I need a sample size of $N = 350$ ISOs.

This shows that a moderate-scale sample of ISOs, such as expected from LSST (see Chapter 4), will distinguish between velocity models. Indeed, it shows a need for a broad slate of theoretical models exploring the full range of production

mechanisms for ISOs, which make testable predictions.

3.5 Conclusion

I have used chemodynamical measurements of nearby stars with *Gaia*, accounting for the survey's selection function and stellar death, to build the first high-resolution model of the *sine morte* stellar population in the solar neighbourhood. I then combine this with models of how the Galactic ISO population relates to its parent stellar population, as in Chapter 2, and a protoplanetary disk chemical model assuming ISOs are largely sourced from outside the water ice line. From this, I make a novel prediction of the chemodynamics of the ISOs passing through the Solar System: their joint distribution in velocity, chemical composition and age.

This model predicts that the ISO velocity distribution is highly structured into moving groups, like the stellar velocity distribution, and that low-$f_{\mathrm{H_2O}}$ ISOs reside mainly in moving groups. This chemodynamic variation also causes a correlation with radiant, as ISOs approaching the Sun from a direction near the Solar apex have lower water mass fractions.

The current observed ISOs are typical of the predicted population. Both 1I and 2I belong to moving groups that are the transient products of resonances with the Galactic potential. I find that the pre-encounter velocity of 1I/'Oumuamua belongs to the Pleiades moving group (there is no preferred origin in the open cluster Matariki, M45), while 2I/Borisov belongs to the Coma Berenices moving group. 1I/'Oumuamua is typical, rather than unusual: the Hyades-Pleiades branch from which it came will be the source of 18% of the $q < 5\,\mathrm{au}$ ISOs passing through the inner Solar System. The correlations between velocity and other properties mean I can use the velocities of the known ISOs to predict the distributions their ages and compositions must have been drawn from. I find that the composition distributions of both 1I and 2I are weighted towards lower values of $f_{\mathrm{H_2O}}$ and higher parent-star metallicities compared towards the overall population. The age distribution for 1I is shifted slightly towards younger values and for 2I is shifted towards older values; this is expected from the correlation of stellar velocity

dispersion with age. However, I find that both ISOs share their velocities with stars of all ages, so they could have any age.

Finally, I find that in addition to being complex and featured, my prediction will be distinguishable from smooth Gaussian velocity distributions, e.g. those fit to M-, G- and OB-type giant stars used by Hoover et al. (2022) and Marčeta (2023). Using relative likelihood tests I calculate that with a sample of 50 ISOs drawn from my predicted distribution, the OB-type giant velocity distribution for ISOs could be ruled out to a 3σ level. This significance rises to 5σ with a sample of 100 ISOs. This method can be generalised to compare any models.

Almost all the ISOs we will see will have come to us from across the Galaxy and across cosmic time. The upcoming LSST ISO sample thus holds the possibility of independently testing both the universality of planetesimal formation theories such as the streaming instability, and the current understanding of Galactic star-formation history. It will be up to the creation of theoretical models for planetesimal and ISO formation building on those presented here, a more detailed understanding of the nuances of ISO dynamics in the Galaxy, and the exquisite detection capabilities of the surveys of the 2020s and 2030s to bring this promise to reality.

Sample size	Sample model	Mean ± std of log likelihood with comparison model				Relative significance (σ)			
		Gaia	M	G	OB	Gaia	M	G	OB
N=50	Gaia	-14.0 ± 0.2	-14.4 ± 0.4	-14.9 ± 0.7	-21.8 ± 2.2	**0.0**	**0.7**	**1.3**	**3.5**
N=50	M	-14.0 ± 0.1	-13.8 ± 0.2	-14.0 ± 0.3	-18.5 ± 1.1	0.8	0.0	0.8	4.4
N=50	G	-13.6 ± 0.1	-13.4 ± 0.1	-13.3 ± 0.2	-15.6 ± 0.7	1.6	0.8	0.0	3.2
N=50	OB	-12.9 ± 0.1	-12.7 ± 0.0	-12.2 ± 0.1	-11.4 ± 0.2	7.8	7.6	4.7	0.0
N=100	*Gaia*	-14.0 ± 0.1	-14.3 ± 0.3	-14.9 ± 0.4	-21.5 ± 1.4	**0.0**	**1.0**	**1.9**	**5.2**
N=100	M	-14.0 ± 0.1	-13.8 ± 0.1	-14.1 ± 0.2	-18.4 ± 0.7	1.1	0.0	1.2	6.3
N=100	G	-13.6 ± 0.1	-13.4 ± 0.1	-13.3 ± 0.1	-15.6 ± 0.5	2.3	1.1	0.0	4.5
N=100	OB	-12.9 ± 0.1	-12.7 ± 0.0	-12.2 ± 0.0	-11.4 ± 0.1	12.0	11.3	7.1	0.0
N=150	*Gaia*	-14.0 ± 0.1	-14.4 ± 0.2	-14.9 ± 0.4	-21.6 ± 1.2	**0.0**	**1.2**	**2.2**	**6.2**
N=150	M	-14.0 ± 0.1	-13.8 ± 0.1	-14.0 ± 0.2	-18.4 ± 0.6	1.3	0.0	1.5	8.1
N=150	G	-13.6 ± 0.1	-13.4 ± 0.1	-13.2 ± 0.1	-15.5 ± 0.4	3.2	1.6	0.0	6.0
N=150	OB	-12.9 ± 0.0	-12.7 ± 0.0	-12.2 ± 0.0	-11.4 ± 0.1	15.7	14.7	9.4	0.0

Table 3.2: Details of distinguishing models. Most relevant is the sigma values of my *Gaia* model relative to the other models, as this is what I posit as the intrinsic population, so these are marked in bold.

Swiftly I shrivel at the thought of God,
At Nature and its wonders, Time and Space and Death,
But that I, turning, call to thee O soul, thou actual Me,
And lo, thou gently masterest the orbs,
Thou matest Time, smilest content at Death,
And fillest, swellest full the vastnesses of Space.

Greater than stars or suns,
Bounding O soul thou journeyest forth.

— Ralph Vaughan Williams, *A Sea Symphony*
from Walt Whitman, *Leaves of Grass*

4 Simulating Interstellar Objects in the Solar System

The work described in this chapter constitutes part of that published in Dorsey et al. (2025). My contribution was the development of the novel orbit sampling method described below, which allowed a sufficiently large number of ISO discoveries to be simulated to allow meaningful inferences to be made.

4.1 Introduction

The Legacy Survey of Space and Time (LSST) has discovering ISOs as one of its stated mission goals (LSST Science Collaboration et al. 2009; Ivezić et al. 2019). The sample of ISOs it finds will be subject to selection biases and understanding these biases will be necessary to make reconstruct the number density and properties of the underlying population. Modelling the survey section biases, as in Dorsey et al. (2025), is also required to compare predictions of the ISO population, including those that I have made in Chapters 2 and 3, to what is observed.

In Section 4.2 I detail the necessary context to understand both the necessity and workings of my novel orbit sampling method, which I lay out in Section 4.3. Finally, in Section 4.4 I briefly describe the results of Dorsey et al. (2025) which my method enabled.

4.2 Context

4.2.1 Solar System Object Magnitudes

Solar System objects largely do not emit their own visible light[1], and thus are observable with optical telescopes only from the Sun's light that they reflect. This means the radiant flux of a non-cometary Solar System object observed from the Earth is subject to two inverse-square laws: one with respect to the distance of the object from the Sun (r_h), and the other with respect to the distance of the Earth from the object (Δ). Small Solar System objects are generally unresolved, and the radiant flux observed from Earth also depends on the angle at which they are illuminated by the Sun relative to the observer. This is called the phase angle α_{phase}, and is equal to the angle subtended by the Sun-Earth line at the object being observed. Its effect on the radiant flux observed is quantified by the phase function $\Phi(\alpha_{\text{phase}})$, the fractional reduction in flux relative to the flux at opposition ($\alpha_{\text{phase}} = 0$), such that $\Phi(0) = 1$. Thus the radiant V-band flux of a non-cometary Solar System object is given by

$$F_V \propto \frac{1}{r_h^2} \cdot \frac{1}{\Delta^2} \cdot \Phi(\alpha_{\text{phase}}) \tag{4.1}$$

and by setting a constant of proportionality $10^{-\frac{2}{5}H}$ we get an object's apparent visual magnitude as

$$m_V = H + 5\log_{10}\left(\frac{r_h}{(1\,\text{au})}\right) + 5\log_{10}\left(\frac{\Delta}{(1\,\text{au})}\right) - \frac{5}{2}\log_{10}\Phi(\alpha_{\text{phase}})\,. \tag{4.2}$$

The quantity H is called the (V-band) absolute magnitude of the body, in analogy to that of a star. The absolute magnitude is related to the physical size and albedo of the reflecting surface of the object by

$$H = (\text{constant}) - \frac{5}{2}\log D^2 A_g\,, \tag{4.3}$$

for an approximately spherical body with diameter D and geometric albedo A_g, the ratio of the flux from the body at opposition to that of an idealized flat,

[1] Exceptions include aurorae, airglow, artificial light, and the Sun itself.

fully reflecting, diffusely-scattering disk with the same cross-section. The absolute magnitude can be measured for any object with known orbit and photometry[2], whereas its diameter is degenerate with albedo, therefore requiring additional infrared data to measure (Reddy et al. 2012). Thus, H is often treated as a proxy for object size, though it should be noted that, being a magnitude, a larger value of H corresponds to a smaller diameter. The term 'size distribution' can refer to either the distribution of objects in H or D (e.g. as in Engelhardt et al. 2017), however inferring the D distribution from the observed H distribution requires either knowledge or assumptions about the albedos of the bodies in question. Throughout this chapter I will work exclusively with absolute magnitudes H.

There are other effects which change the apparent magnitude of an object. Firstly, since the geometric albedo of a small body and spectral luminosity of the Sun illuminating them vary with photometric band, Solar System small bodies have colours defined similarly to those of stars by the differences in apparent magnitudes between different photometric bands. Though the colours of ISOs and their effects on detectability are studied in Dorsey et al. (2025), this is not relevant to my work in this chapter. Secondly, deviations from spherical shapes introduce a varying apparent magnitude as a varying reflecting cross-section is presented to the observer as the object rotates. This was a major effect for 1I'Oumuamua, which had an extreme axis ratio (Mashchenko 2019). Thirdly, fast-moving objects near the Earth can have high non-sidereal rates of on-sky motion (up to $\sim 1''\mathrm{s}^{-1}$) causing them to form a streak over the exposure time of an image. This increases their effective magnitude, decreasing detectability, in an effect called trailing loss. Finally, this formulation applies to non-cometary bodies, which I consider exclusively in this chapter; comets form an extended dust coma and tail which significantly increases their visibility but is difficult to model. All of these effects are discussed in detail in Dorsey et al. (2025), to which the interested reader is directed.

[2]By either fitting or assuming the form of its phase function, unless it is observed at opposition.

4.2.2 Size Distributions

Small body populations in the Solar System have a range of size distributions, which contain information about the formation and evolution of the population. These size distributions are generally complex, with for example the asteroid belt showing bumps (Bottke et al. 2005) and TNOs showing a break between two power laws with different indices (Lawler et al. 2018). In this work however, as in Dorsey et al. (2025), I model the H distribution of ISOs as a single power law with slope α:

$$\frac{\mathrm{d}n}{\mathrm{d}H} = n_{22} \cdot \alpha \ln(10) \cdot 10^{\alpha(H-22)} \tag{4.4}$$

Due to the complexity of the size distributions of Solar System populations, my co-authors and I are aware that this choice of a single power law to model the ISO H distribution is a reductive approximation. However, since the formation and evolution of ISOs across the Galaxy is completely unconstrained, choosing a simple power law with the slope as a free parameter means our results are broadly applicable.

This distribution is normalised such that

$$\int_{-\infty}^{22} \frac{\mathrm{d}n}{\mathrm{d}H} \mathrm{d}H = n_{22}\,,$$

where n_{22} is the underlying number density of ISOs in the Solar neighbourhood, away from the gravitational focussing effect of the Sun, for ISOs with $H < 22$, the approximate absolute magnitude of 1I/'Oumuamua (Meech et al. 2017). I make this choice because the number density of ISOs in the Solar neighbourhood is inferred by Do et al. (2018) from the detection of 1I/'Oumuamua in the Pan-STARRS survey (Chambers et al. 2016). Being a Poisson statistic with only one observation this value has a large uncertainty (Flekkøy and Toussaint 2023), however for almost all of this work and Dorsey et al. (2025) my co-authors and I are only concerned with the relative distributions of ISOs, not absolute numbers. The only section in which the value of n_{22} matters is where I estimate the number of ISOs that the LSST will discover, described in this chapter in Section 4.4, where I take a value of $n_{22} = 0.1\,\mathrm{au}^{-3}$, based on Do et al. (2018). The detection of 2I/Borisov

cannot be used to further constrain the density of ISOs because it was found outside of a well-characterised survey.

As noted in 4.2.1, the absolute magnitude distribution of Eq. 4.4 can be related to an equivalent diameter distribution with Eq. 4.3 by assuming a constant value of albedo, such that $\mathrm{d}H \propto \mathrm{d}D/D$. Thus observed absolute magnitude distribution slopes are often quoted in terms of the slope of the equivalent diameter distribution q_s, such that

$$\frac{\mathrm{d}n}{\mathrm{d}D} \propto D^{-q_s}\,, \quad q_s = 5\alpha + 1\,. \tag{4.5}$$

4.2.3 Observable Spheres

For a given survey, a set of Solar System objects with a range of values of H has a heliocentric distance $r_h = r_{\mathrm{obs}}$ beyond which even the largest objects in the population ($H = H_{\mathrm{min}}$) are not observable at any point on their orbits because they never reach a sufficiently low magnitude (the survey single-exposure depth m_{depth}). The volume within this distance is called the observable sphere, and r_{obs} can be calculated using Eq. 4.2 by finding the maximum radius for which $m \leq m_{\mathrm{depth}}$. For a given heliocentric distance the magnitude of a Solar System object is minimized when at opposition such that $\Delta = (r_h - 1\,\mathrm{au})$ and $\alpha_{\mathrm{phase}} = 0$, and substituting this into Eq. 4.2 gives

$$\frac{r_{\mathrm{obs}}}{(1\,\mathrm{au})} = \frac{1}{2}\left(1 + \sqrt{1 + 4 \times 10^{(m_{\mathrm{depth}} - H_{\mathrm{min}})/5}}\right). \tag{4.6}$$

For modelling ISOs in the LSST in Dorsey et al. (2025) we chose a value of $m_{\mathrm{depth}} = 25$. This is based on the five-sigma point source single-image depth for the deepest LSST filter, which is g (Bianco et al. 2022).

4.3 Orbit Sampling

4.3.1 Introduction to the Problem

To simulate the discovery of ISOs, a realistic population of ISOs in the inner Solar System must be modelled. This is a complex problem, as the Solar System's gravity

deflects the paths of ISOs, increasing their number density in the inner Solar System in a non-trivial and velocity-dependent way, a process called gravitational focussing (see Sec. 3.2.6 and Sec. 4.3.5). Additionally, a sufficiently large population of ISO discoveries needs to be simulated in order to achieve low Poisson errors when estimating quantities such as the fraction of ISOs simulated that are discovered.

Many previous works (e.g. Cook et al. 2016; Engelhardt et al. 2017; Seligman and Laughlin 2018; Hoover et al. 2022) account for gravitational focusing numerically by generating a large number of ISOs with velocities drawn from the background distribution, unperturbed and unfocused, and positions drawn homogeneously from a volume around the Solar System significantly larger than the observable sphere, such that focussing effects are negligible. These ISOs are then propagated along their trajectories under the gravitational influence of the Solar System to produce a population of orbits. From this large number of simulated ISOs, analysis is then only carried out on the tiny fraction that enter the observable sphere. For example, in order to simulate a sample of $\sim 10^6$ ISOs for study within an $r_{\mathrm{obs}} = 50\,\mathrm{au}$ observable sphere for Engelhardt et al. (2017), $\sim 1.7 \times 10^9$ positions and velocities had to be sampled and propagated. Using this method to generate a sufficiently large sample of observable ISOs to achieve low Poisson errors is inefficient and computationally expensive.

Improving on this, Marčeta (2023) developed the "probabilistic method" of directly and analytically sampling the positions and velocities of ISOs within a sphere around the Sun, automatically accounting for gravitational focusing. This is very elegant and significantly more efficient than the numerical method described above, however it only produces a sample of ISO positions and velocities within the sphere at a given single moment in time. This means that the sphere from which ISOs are sampled must be larger than the observable sphere to include ISOs which will enter the observable sphere over the course of the survey, and again only the minority of simulated ISOs that enter the observable sphere contribute to the analysis. This is inefficient, and means constraints must be placed on the ISOs simulated. Marčeta and Seligman (2023) sampled ISOs from a sphere with a radius 30 au to

populate a observable sphere with a radius of only $\sim 8\,\mathrm{au}$. With this configuration they were restricted to only modelling ISOs with $H > 15.6$ and asymptotic speeds $v_\infty \leq 100\,\mathrm{km\,s^{-1}}$, and could only simulate a single year of the LSST. Scaling up this method to model the full ten years of LSST would require sampling ISOs from a volume a factor of 10^3 larger to populate the same 8 au-radius observable sphere.

Inspired by the probabilistic method of Marčeta (2023), my novel method samples the orbits of ISOs directly, such that every ISO modelled passes through the observable sphere at some point in survey. With this we can simulate the full 10 years with no restriction on asymptotic speed and a significantly wider range of absolute magnitudes. This range of absolute magnitudes is actually too wide to simulate efficiently in one go, a problem I describe then solve in Section 4.3.4.

4.3.2 Deriving the Distribution of Orbits

My method of modelling the dynamics of ISOs in the Solar System samples the distribution of their orbits directly. The trajectories of ISOs are well-modelled by hyperbolae with foci at the Solar System barycentre. This holds for the vast majority of ISOs which do not pass too close to either the Sun or one of the planets but does ignore non-gravitational acceleration caused by outgassing, which for the purposes of this work is negligible (Bailer-Jones et al. 2018, 2020). As with all Keplerian orbits, an ISO's orbit is determined by six parameters. The shape of the hyperbolic trajectory is parametrized by the first five: the three components of the ISOs pre-encounter velocity relative to the Solar System $\mathbf{v}_\infty$, the impact parameter B and the position angle of the impact parameter φ. The sixth and final parameter determines the progress of the ISO along this trajectory at a given time; for this I choose the time it passes pericentre τ. One ISO orbit is one sample from the joint distribution of these six parameters; In this section I derive this joint distribution, and in the next (Sec. 4.3.3) I describe my method of drawing samples from it.

Some other quantities and relations are useful to define here. A semi-major axis can be defined for a hyperbolic orbit, it is strictly negative and equal to

$a = -GM_\odot/v_\infty^2$, so I define $A = GM_\odot/v_\infty^2 = -a$ as its absolute value. The barycentric radial velocity of an ISO on a hyperbolic orbit, v_r is found by considering the conservation of energy,

$$\frac{1}{2}(v_r^2 + v_t^2) - \frac{GM_\odot}{r} = \frac{1}{2}v_\infty^2$$

where r is the barycentric distance, and substituting for the barycentric transverse velocity v_t using the conservation of angular momentum, $rv_t = Bv_\infty$, with rearrangement giving

$$v_r = \frac{v_\infty}{r}\sqrt{r^2 + 2Ar - B^2}\,. \tag{4.7}$$

The pericentre q of the orbit can be found by setting $r = q$ when $v_r = 0$, giving

$$q = \sqrt{A^2 + B^2} - A\,. \tag{4.8}$$

At a given v_∞, the perihelion of an orbit increases strictly with impact parameter, meaning there is a maximum $B = B_{\max}$ above which ISOs do not enter the observable sphere. This is found by setting $q = r_{\rm obs}$, implying

$$B_{\max} = \sqrt{r_{\rm obs}^2 + 2Ar_{\rm obs}}\,. \tag{4.9}$$

Now we can begin to derive the distribution function of ISO orbits. First one must consider the differential flux of ISOs along an orbit defined by ($\mathbf{v}_\infty$, B, φ, τ). The range of impact parameters $[B, B + \mathrm{d}B]$ and position angles $[\varphi, \varphi + \mathrm{d}\varphi]$ corresponds to a cross section of $\sigma = B\mathrm{d}B\mathrm{d}\varphi$. For a velocity probability distribution function $p_{\mathbf{v}_\infty}$, the number density of ISOs with velocity at infinity within the infinitesimal volume of velocity space $\mathrm{d}^3\mathbf{v}_\infty$ is given by $n_{\mathbf{v}_\infty}\mathrm{d}^3\mathbf{v}_\infty = np_{\mathbf{v}_\infty}\mathrm{d}^3\mathbf{v}_\infty$, where n is the background number density of the objects being studied, unperturbed and unfocussed by the gravity of the Sun. The rate at which ISOs with these velocities pass on orbits through this cross section is given by the standard formula $v_\infty \cdot n_{\mathbf{v}_\infty} \cdot \sigma = v_\infty \cdot np_{\mathbf{v}_\infty}\mathrm{d}^3\mathbf{v}_\infty \cdot B\mathrm{d}B\mathrm{d}\varphi$. Thus, following a similar notation scheme to Marčeta (2023), the differential flux distribution of ISOs is given by

$$F_{\mathbf{v}_\infty B\varphi} = nBv_\infty p_{\mathbf{v}_\infty} \tag{4.10}$$

such that $F_{\mathbf{v}_\infty B\varphi}\mathrm{d}^3\mathbf{v}_\infty \mathrm{d}B\mathrm{d}\varphi$ is the rate at which ISOs pass on orbits in the infinitesimal region of parameter space $\mathrm{d}^3\mathbf{v}_\infty \mathrm{d}B\mathrm{d}\varphi$. Under the assumption that the density and velocity distribution of ISOs around the Sun remain constant over the timescale of a survey (this is expected, see Portegies Zwart 2021; Forbes et al. 2024). Under the assumption that n and velocity distribution $p_{\mathbf{v}_\infty}$ of ISOs around the Sun remain constant over the timescale of a survey (this is expected, see Portegies Zwart 2021; Forbes et al. 2024), this flux is constant in time and therefore equal at all points along an orbit.

As described in Section 4.2.3, a population of objects in the Solar System has a observable sphere centred on the Sun outside of which they cannot be observed, with radius r_{obs} set by the largest object (lowest H) in the population. The novel innovation of my sampling method is to only sample ISOs which occupy this observable sphere during a survey of length T. A diagram showing an ISO orbit with $v_\infty = 10\,\mathrm{km\,s^{-1}}$ and $B = 4\,\mathrm{au}$ passing through an observable sphere with $r_{\mathrm{obs}} = 8\,\mathrm{au}$ is shown in Fig. 4.1. The length of time an object on a hyperbolic orbit with speed v_∞ and impact parameter B resides inside the observable sphere is given by doubling the time it takes to go from perihelion to a barycentric distance of r_{obs}:

$$\begin{aligned} t_{\mathrm{res}}(v_\infty, B) &= 2\int_q^{r_{\mathrm{obs}}} \frac{\mathrm{d}r}{v_r} \\ &= \frac{2}{v_\infty}\int_q^{r_{\mathrm{obs}}} \frac{r\mathrm{d}r}{\sqrt{r^2 + 2Ar - B^2}} \\ &= \frac{2}{v_\infty}\left(\sqrt{B_{\mathrm{max}}^2 - B^2} - A\log\left(\frac{\sqrt{B_{\mathrm{max}}^2 - B^2} + r_{\mathrm{obs}} + A}{\sqrt{A^2 + B^2}}\right)\right) \end{aligned} \tag{4.11}$$

The Sun is offset from the Solar System barycentre by a displacement of magnitude $\sim 1R_\odot = 0.005\,\mathrm{au}$ which varies on the timescale of years, so the same offset exists between the centre of the observable sphere as defined in Sec. 4.2.3 and the foci of the hyperbolic orbits. I assume that this offset is negligible, as even the smallest observable spheres used have $r_{\mathrm{obs}} > 1\,\mathrm{au}$, and sample ISO orbits passing through a sphere of radius r_{obs} as given by Eq. 4.6 centred on the Solar System barycentre. In Dorsey et al. (2025) this assumption was made for sampling orbits,

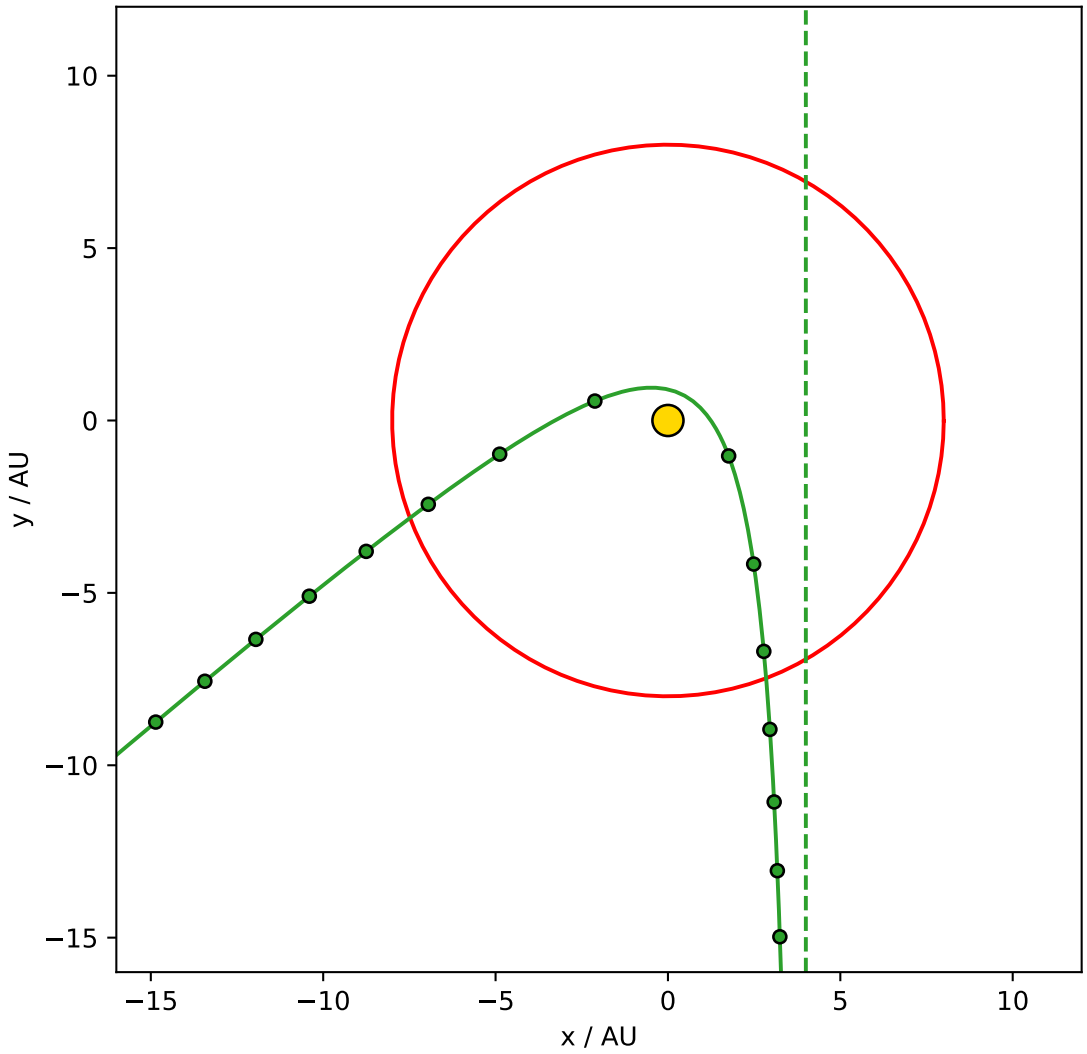

Figure 4.1: A diagram showing the path of an ISO ($v_\infty = 10\,\mathrm{km\,s^{-1}}$, $B = 4\,\mathrm{au}$, in green) passing through an observable sphere ($r_{\mathrm{obs}} = 8\,\mathrm{au}$, red) around the Sun (yellow). A vertical green dashed line shows the unperturbed path of the ISO, and circular markers on the ISO's trajectory show its position at equal intervals in time (220 days).

however the true heliocentric distance r_h was still used to calculate the apparent magnitude of ISOs in the survey simulation.

With residence time $t_{\mathrm{res}}(v_\infty, B)$ for each orbit, the number of objects on an orbit ($\mathbf{v}_\infty$, B, φ) that will be inside the observable sphere at any point in the survey of length T (e.g. $T = 10\,\mathrm{yr}$ for LSST) is equal to the sum of those in the sphere when

the survey begins, plus the number that flow in over time T:

$$\begin{aligned}\frac{\mathrm{d}N}{\mathrm{d}^3\mathbf{v}_\infty \mathrm{d}B\mathrm{d}\varphi} &= \Big(t_{\mathrm{res}}(\mathbf{v}_\infty, B, \varphi) + T\Big) F_{\mathbf{v}_\infty B\varphi} \\ &= 2nBp_{\mathbf{v}_\infty}\left(\sqrt{B_{\mathrm{max}}^2 - B^2} - A\log\left(\frac{\sqrt{B_{\mathrm{max}}^2 - B^2} + r_{\mathrm{obs}} + A}{\sqrt{A^2 + B^2}}\right) + \frac{v_\infty T}{2}\right)\end{aligned} \tag{4.12}$$

This is the number distribution of ISOs on each orbit that pass within the observable sphere during the course of the survey, therefore is the joint distribution of $\mathbf{v}_\infty$, B and φ that we need to sample.

This distribution does not account for shielding, the removal of ISOs from the distribution due to their destruction by the Sun. This process is accounted for intrinsically by the method of Marčeta (2023), however it could easily be included in my method simply by ignoring the relatively few ISOs that reach heliocentric distances less than the 10 Solar radii ($10R_\odot = 0.05\,\mathrm{au}$) limit suggested by Marčeta (2023). This limit comfortably exceeds the distance at which objects would be tidally disrupted ($3.45R_\odot$, Jones et al. 2018)[3], and though Granvik et al. (2016) suggests near-Earth asteroids with perihelia as high as $\sim 50R_\odot$ can be thermally destroyed, that is a process that occurs over many perihelion passages and therefore not applicable to ISOs. In Dorsey et al. (2025) we find that only 0.02% of the ISO population detectable in the LSST have perihelia less than the $10R_\odot$ limit of Marčeta (2023), therefore we treat the effect of shielding as negligible.

This result can be checked by comparison to Marčeta (2023). For $T = 0$, Eq. 4.12 gives the distribution of ISOs within a sphere of radius $r = r_{\mathrm{obs}}$ at single moment in time. Differentiating this with respect to r and dividing by the surface area of this sphere $4\pi r^2$ gives instead the density distribution of ISOs in $\mathbf{v}_\infty$, B, and φ at a barycentric distance r:

$$\begin{aligned}\frac{1}{4\pi r^2}\frac{\mathrm{d}}{\mathrm{d}r}\left(\frac{\mathrm{d}N}{\mathrm{d}^3\mathbf{v}_\infty \mathrm{d}B\mathrm{d}\varphi}\right) &= \frac{\mathrm{d}n}{\mathrm{d}^3\mathbf{v}_\infty \mathrm{d}B\mathrm{d}\varphi} \\ &= \frac{nBp_{\mathbf{v}_\infty}}{2\pi r\sqrt{B_{\mathrm{max}}^2 - B^2}}\end{aligned} \tag{4.13}$$

[3]While reading this work, this DPhil candidate discovered the term 'Marsden Sunskirters' and thinks this would make a good name for a New Zealand-based physics department band.

This equals Marčeta (2023)'s Eq. 12 in the $B_1 \leq B \leq B_2$ range, for orbits unaffected by shielding, which measures the same quantity.

Note that each distribution derived here is a number distribution, not a probability density function, however probability density functions can be acquired with relative ease by normalisation.

In the next subsection I describe how to sample from the distribution of orbits in Eq. 4.12, a non-trivial process, using a method again inspired by that used by Marčeta (2023) to sample their own complex distribution.

4.3.3 Sampling from the Distribution of Orbits

Firstly, the distribution of orbits (Eq. 4.12) is independent of φ, so φ can be drawn independently from the other parameters from a uniform distribution between 0 and 2π and be immediately marginalised over:

$$\begin{aligned}\frac{\mathrm{d}N}{\mathrm{d}^3\mathbf{v}_\infty \mathrm{d}B} &= \int_0^{2\pi} \frac{\mathrm{d}N}{\mathrm{d}^3\mathbf{v}_\infty \mathrm{d}B \mathrm{d}\varphi}\mathrm{d}\varphi \\ &= 4\pi n B p_{\mathbf{v}_\infty}\left(\sqrt{B_{\max}^2 - B^2} - A\log\left(\frac{\sqrt{B_{\max}^2 - B^2} + r_{\mathrm{obs}} + A}{\sqrt{A^2 + B^2}}\right) + \frac{v_\infty T}{2}\right) \\ &= 4\pi n B_{\max}^2 p_{\mathbf{v}_\infty}\left(x\sqrt{1-x^2} - A' x\log\left(\frac{\sqrt{1-x^2} + \sqrt{A'^2+1}}{\sqrt{A'^2 + x^2}}\right) + \frac{v_\infty T}{2B_{\max}}x\right) \quad (4.14)\end{aligned}$$

where I have defined the dimensionless quantities $x = B/B_{\max}$ and $A' = A/B_{\max}$ and made the substitution $r_{\mathrm{obs}} + A = \sqrt{A^2 + B_{\max}^2} = B_{\max}\sqrt{A'^2 + 1}$ (Eq. 4.9).

Eq. 4.14 is the joint distribution in just $\mathbf{v}_\infty$ and B. As a preparatory step, I partially integrate it over B, to acquire a cumulative distribution function in

B at a given value of $\mathbf{v}_\infty$:

$$\begin{aligned}
&\mathrm{CDF}(B \mid \mathbf{v}_\infty) = \int_0^B \frac{\mathrm{d}N}{\mathrm{d}^3\mathbf{v}_\infty \mathrm{d}B}\mathrm{d}B \\
&= 4\pi n B_{\max}^3 p_{\mathbf{v}_\infty} \int_0^x \left(x\sqrt{1-x^2} - A' x \log\left(\frac{\sqrt{1-x^2}+\sqrt{A'^2+1}}{\sqrt{A'^2+x^2}} \right) + \frac{v_\infty T}{2B_{\max}} x \right) \mathrm{d}x \\
&= 4\pi n B_{\max}^3 p_{\mathbf{v}_\infty} \left(\frac{1-(1-x^2)^{3/2}}{3} \right. \\
&- \frac{A'}{2}\left((A'^2+x^2)\log\left(\frac{\sqrt{1-x^2}+\sqrt{A'^2+1}}{\sqrt{A'^2+x^2}} \right) \right. \\
&\qquad - A'^2 \log\left(\frac{1+\sqrt{A'^2+1}}{A'} \right) - \sqrt{A'^2+1}\sqrt{1-x^2} + \sqrt{A'^2+1} \Bigg) \\
&\qquad\qquad \left. + \frac{v_\infty T x^2}{4B_{\max}} \right) \qquad (4.15)
\end{aligned}$$

For $B = B_{\max}$, or equivalently $x = 1$, this is equal to the marginal $\mathbf{v}_\infty$ distribution of all orbits passing through the observable sphere, integrated over all other parameters:

$$\frac{\mathrm{d}N}{\mathrm{d}^3\mathbf{v}_\infty} = 4\pi n B_{\max}^3 \left(\frac{1}{3} - \frac{A'}{2}\left(\sqrt{A'^2+1} - A'^2 \log\left(\frac{1+\sqrt{A'^2+1}}{A'} \right) \right) + \frac{v_\infty T}{4B_{\max}} \right) \cdot p_{\mathbf{v}_\infty} \qquad (4.16)$$

This is a function of only $\mathbf{v}_\infty$, T and r_{obs}.

We can now start sampling. Sampling the distribution in Eq. 4.16 gives the pre-encounter velocities of ISOs passing through the observable sphere. So far I have not specified the form of the underlying velocity distribution of ISOs in the Solar neighbourhood $p_{\mathbf{v}_\infty}$ and this method would work with any form, but I proceed with the underlying ISO velocity distribution calculated in Chapter 3 (Figure 3.4), without the volume sampling rate applied. This $p_{\mathbf{v}_\infty}$ takes the form of a probability mass function, a distribution of weighted points in velocity space (See Table 3.1). Therefore to draw samples from the marginal $\mathbf{v}_\infty$ distribution here, I reweight these points in velocity space by the prefactor to $p_{\mathbf{v}_\infty}$ in Eq. 4.16 and sample from these. This gives us values of $\mathbf{v}_\infty$ for orbits passing through the observable sphere.

We can then work backwards through the integrals calculated in this section to sample the remaining parameters that define each ISO orbit, starting with B.

By evaluating, normalizing and inverting the cumulative distribution $\mathrm{CDF}(B \mid \mathbf{v}_\infty)$ (Eq. 4.15) for each value of $\mathbf{v}_\infty$, a value of B can be drawn by sampling from a uniform distribution between 0 and 1. This gives a value of B corresponding to each value of $\mathbf{v}_\infty$.

As noted at the start of this subsection, the distribution of orbits (Eq. 4.12) is independent of φ, so for each ($\mathbf{v}_\infty$, B) pair a value of φ can be drawn uniformly from between 0 and 2π. This completes the sampling of the distribution of orbits given in Eq. 4.12 and provides a set of hyperbolic trajectories defined by ($\mathbf{v}_\infty$, B, φ).

The final step is to place a single ISO on each of these orbits by sampling a perihelion time τ. Since the flux along each orbit is constant the distribution of τ is uniform along each orbit (Section 4.3.2). An ISO which leaves the observable sphere immediately after the survey begins at time $t = 0$ passes perihelion at $t = -t_{\mathrm{res}}(v_\infty, B)/2$, and one which enters the observable sphere just as the survey ends at time $t = T$ passes perihelion at $T + t_{\mathrm{res}}(v_\infty, B)/2$. Because I am only sampling ISOs that occupy the observable sphere at any time during the survey, these values bound the uniform τ distribution for each orbit. This, finally, gives sets of values ($\mathbf{v}_\infty$, B, φ, τ), each defining an ISO on an orbit passing through the observable sphere of radius r_{obs} during a survey of length T.

4.3.4 A Method of Shells

To make a sample of simulated ISOs, orbits are sampled using the method above and a value of H is assigned to each, drawn from the chosen absolute magnitude distribution (Sec. 4.2.2). This sample of ISOs can then be passed through a survey simulator to calculate which would be discovered. To study the properties of the discovered ISO population with low Poisson errors, a large number of ISOs discoveries need to be simulated. If only a very low fraction of the simulated ISOs are actually discoverable, the number of ISOs which must be passed through the survey simulator becomes intractably large. Even with my novel orbit sampling method, this occurs when a wide range of sizes are simulated simultaneously: the observable sphere orbits are sampled from must be large enough to accommodate the largest sizes

simulated, but due to the power-law nature of the size distribution most objects are significantly smaller than this. Thus when a broad size distribution is passed into the survey simulator, most of the ISOs simulated never reach a detectable magnitude.

To resolve this, I developed a method of splitting the H distribution into narrow bins ($\Delta H = 1.0$) which can be simulated separately then recombined, increasing the fraction of ISOs simulated that are then detected. Each size bin then has its own observable sphere with radius set by the minimum H of just that bin (Eq. 4.6). Simulating each size bin separately has an additional advantage: the number of ISOs simulated in each bin can be tuned to ensure a statistically-useful number of ISOs are discovered in each bin, allowing meaningful inferences to be carried out at all sizes.

However, it is also desirable to combine and compare the simulated ISO discoveries across the size bins. To do this, I calculate the ratio between the number of ISOs from each size bin expected to enter the corresponding observable sphere and the number simulated, then reweight the discovered ISO sample by this amount. I do this by integrating the number distribution of orbits derived in Section 4.3.2 to calculate its normalization, equal to the number of orbits passing through a given observable sphere over the survey length, N. This is achieved by integrating the marginal velocity distribution (Eq. 4.16) over $\mathbf{v}_\infty$. As described in Section 4.3.3, the form of $p_{\mathbf{v}_\infty}$ that I use is the underlying ISO distribution I calculated in Chapter 3), a probability mass function of points in velocity space $\mathbf{v}_i$ with assigned weights w_i, proportional to the values given in Table 3.1 in that same chapter. Crucially for this calculation, I normalize these weights such that $\sum_i w_i = 1$. I can then calculate N for each observable sphere by summing over these points in velocity space the product of the prefactor to $p_{\mathbf{v}_\infty}$ in Eq. 4.16, evaluated at each point's asymptotic velocity $\mathbf{v}_{\infty,i}$, with these weights:

$$\begin{aligned} N &= \int 4\pi n B_{\max}^3 \left(\frac{1}{3} - \frac{A'}{2} \left(\sqrt{A'^2+1} - A'^2 \log \left(\frac{1+\sqrt{A'^2+1}}{A'} \right) \right) + \frac{v_\infty T}{4B_{\max}} \right) \cdot p_{\mathbf{v}_\infty} \, \mathrm{d}^3\mathbf{v}_\infty \\ &= 4\pi n \sum_i B_{\max,i}^3 \left(\frac{1}{3} - \frac{A'_i}{2} \left(\sqrt{A'^2_i+1} - A'^2_i \log \left(\frac{1+\sqrt{A'^2_i+1}}{A'_i} \right) \right) + \frac{v_{\infty,i} T}{4B_{\max,i}} \right) \cdot w_i \\ &= n V_{\mathrm{eff}}(r_{\mathrm{obs}}, T) \end{aligned} \tag{4.17}$$

where for ease of notation I have defined $V_{\rm eff}(r_{\rm obs}, T)$ as an 'effective volume' of space swept out by the motion of ISOs relative to the Solar System. Since $B_{\rm max}$ and A' depend on $\mathbf{v}_\infty$, in the summand they are evaluated at each point's $\mathbf{v}_i$, denoted by a subscript i.

The number density n that should be used in this calculation is the number density of ISOs in the size bin, $n_{[H_{\rm min}, H_{\rm max}]}$. This is calculated by integrating the H distribution (Eq. 4.4) between the limits of the bin, giving

$$n_{[H_{\rm min}, H_{\rm max}]} = n_{22}\left(10^{\alpha(H_{\rm max}-22)} - 10^{\alpha(H_{\rm min}-22)}\right) \tag{4.18}$$

Therefore the number of ISOs within a given size bin expected to enter the corresponding observable sphere is given by

$$N_{[H_{\rm min}, H_{\rm max}]} = n_{22}\left(10^{\alpha(H_{\rm max}-22)} - 10^{\alpha(H_{\rm min}-22)}\right) \cdot V_{\rm eff}(r_{\rm obs}, T) \tag{4.19}$$

4.3.5 The Gravitationally-Focussed Number Density Profile

Substituting $T = 0$ in Eq. 4.17 gives the number of ISOs within a sphere of radius $r = r_{\rm obs}$:

$$\begin{aligned} N &= \int 4\pi n B_{\rm max}^3 \left(\frac{1}{3} - \frac{A'}{2}\left(\sqrt{A'^2+1} - A'^2 \log\left(\frac{1+\sqrt{A'^2+1}}{A'}\right)\right)\right) \cdot p_{\mathbf{v}_\infty}\, \mathrm{d}^3\mathbf{v}_\infty \\ &= 4\pi n \int \left(\frac{B_{\rm max}^3}{3} - \frac{A}{2}\left(B_{\rm max}\sqrt{A^2+B_{\rm max}^2} - A^2 \log\left(\frac{B_{\rm max}+\sqrt{A^2+B_{\rm max}^2}}{A}\right)\right)\right) \cdot p_{\mathbf{v}_\infty}\, \mathrm{d}^3\mathbf{v}_\infty \\ &= 4\pi n \int \left(\frac{B_{\rm max}^3}{3} - \frac{A}{2}(A+r)B_{\rm max} + \frac{A^3}{2}\log\left(1+\frac{B_{\rm max}+r}{A}\right)\right) \cdot p_{\mathbf{v}_\infty}\, \mathrm{d}^3\mathbf{v}_\infty \end{aligned} \tag{4.20}$$

simplified using $\sqrt{A^2+B_{\rm max}^2} = A + r$ (Eq. 4.9). Differentiating N with respect to r, using $B_{\rm max} = \sqrt{r^2+2Ar}$ and $\frac{\mathrm{d}B_{\rm max}}{\mathrm{d}r} = \frac{r+A}{B_{\rm max}}$, gives

$$\begin{aligned} \frac{\mathrm{d}N}{\mathrm{d}r} &= 4\pi n \int r B_{\rm max} \cdot p_{\mathbf{v}_\infty} \mathrm{d}^3\mathbf{v}_\infty \\ &= 4\pi r^2 n \int \sqrt{1+\frac{2A}{B_{\rm max}}} \cdot p_{\mathbf{v}_\infty} \mathrm{d}^3\mathbf{v}_\infty \end{aligned} \tag{4.21}$$

thus the gravitationally-focussed number density of ISOs at a distance of r from the Solar System barycentre, averaged over a thin shell of radius r and thickness $\mathrm{d}r$, is given by

$$\frac{\mathrm{d}N}{4\pi r^2 \mathrm{d}r} = n \int \sqrt{1 + \frac{2GM_\odot}{v_\infty^2 r}} \cdot p_{\mathbf{v}_\infty} \mathrm{d}^3\mathbf{v}_\infty \,. \tag{4.22}$$

This is only the average over the spherical shell; there will be variations in density around this shell but the calculation of these is beyond my skill and the scope of this chapter.

To check this formula I can compare to other works. Marčeta (2023)'s Eq. 18 describes the same quantity up to a factor of n, and corresponds to my formula in the case of $B = B_2$ and $R = 0$ (no shielding) exactly as expected. Siraj et al. (2023)'s Eq. 4 also claims to describe this quantity, however their formula differs from that of mine and Marčeta 2023 by a square root, and I believe this to be an error on their part.

4.4 Results

In Dorsey et al. (2025), the orbit sampling method I developed and describe in Section 4.3 is used to generate populations of ISOs with a range of H distributions, which are then passed through an LSST survey simulator. This simulator was based on the `baseline_v3.3_10yrs` cadence simulation, a planned list of every pointing in the LSST, paired with simulated seeing conditions, limiting magnitudes, and everything needed to calculate the detectability of a Solar System small body. I wrote a script to calculate which pointings each input ISO appeared in, and using this Dr Rosemary Dorsey's code calculated from these which input ISOs would be discovered, given the capabilities of the LSST moving object discovery pipeline.

We tested a series of size distribution slopes: $q_s = 2.5$, 2.8, 3.0, 3.5, 4.0 (corresponding at fixed albedo to H distributions (Eq. 4.4) with $\alpha = 0.3$, 0.36, 0.4, 0.5, 0.6). This covers the range of size distribution slopes found in the Solar System, from the shallow size distribution slope of the main asteroid belt (Gladman et al. 2009) to the steeper slope of the trans-Neptunian objects (Lawler et al. 2018).

We chose to test $q_s = 2.8$ in particular as the size distribution expected to be produced by the streaming instability, a mechanism for planetesimal formation (Simon et al. 2016), and therefore the potential size distribution of primordial planetesimals without collisional evolution.

We considered each size distribution slope q_s separately. For each, we divided the H range ($H = 5$ to $H = 23$) into 1-mag bins and calculated the radius of the observable sphere with the lower H bound for each bin (Sec. 4.2.3). With these observable spheres we drew 10,000 ISO orbits for each bin with $H < 13$ and 50,000 ISO orbits for each bin with $13 < H$. Since the drawn values of $\mathbf{v}_\infty$ are samples from the *Gaia*-based chemodynamical distribution of Chapter 3, we could track the chemical composition and age of the drawn ISOs too to investigate the effects of detection bias on these properties. We finally assigned a value of H to each ISO drawn from the H distribution within each bin.

Passing these drawn ISOs into the survey simulator calculates which ISOs would be discovered. My method of shells described in Section 4.3.4 can be used to reweight the observed ISOs so the different H bins can be compared and combined into a 'discoverable' distribution for each input H distribution.

The velocity distribution of this discoverable population is plotted in Figure 4.2 for H distributions with $q_s = 2.8$ and $q_s = 4.0$. Comparing to the underlying velocity distributions of Fig 3.4 the moving groups in U and V are still clearly visible for both H distributions, meaning that these features of Galactic dynamics will be detectable in the discovered ISOs. The speed distribution shows that the most likely asymptotic speed for discovered ISOs is close to that of 1I and 2I, with detection biases causing a preference for slower ISOs compared to the underlying population, especially for steeper H distributions (higher q_s) which have more smaller objects. This is due to these smaller objects only being detectable closer to the Earth, meaning at high velocities they spend very little time at an observable magnitude, and making them more susceptible to gravitational focussing and trailing loss, both of which are velocity dependent.

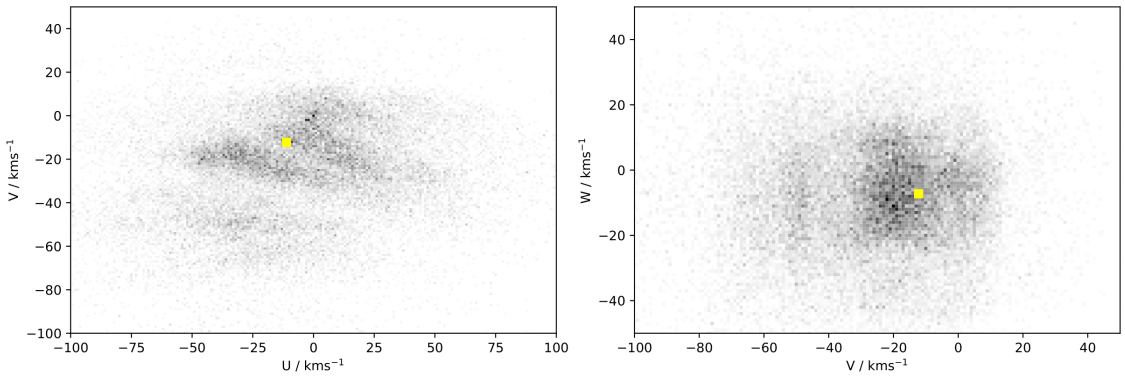

(a) The Galactic velocity distributions of discovered ISOs assuming a $q_s = 2.8$ size distribution. Compare to Fig. 3.4.

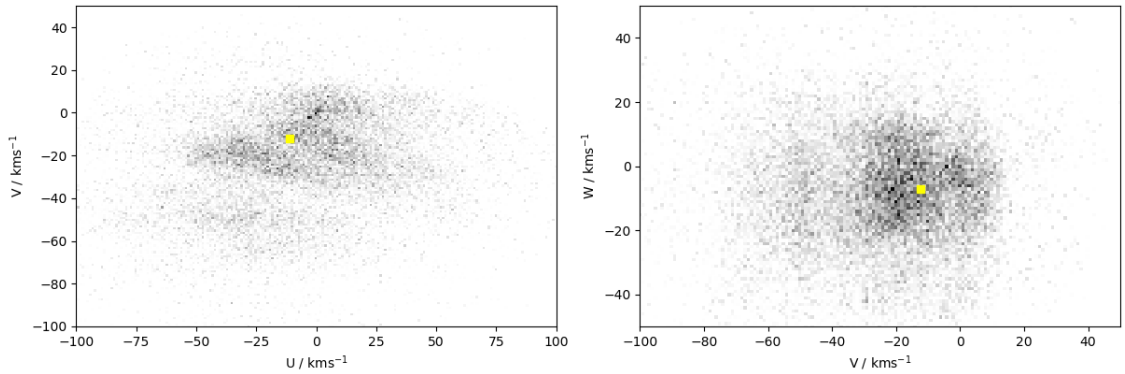

(b) Similar to above, but for a $q_s = 4.0$ size distribution.

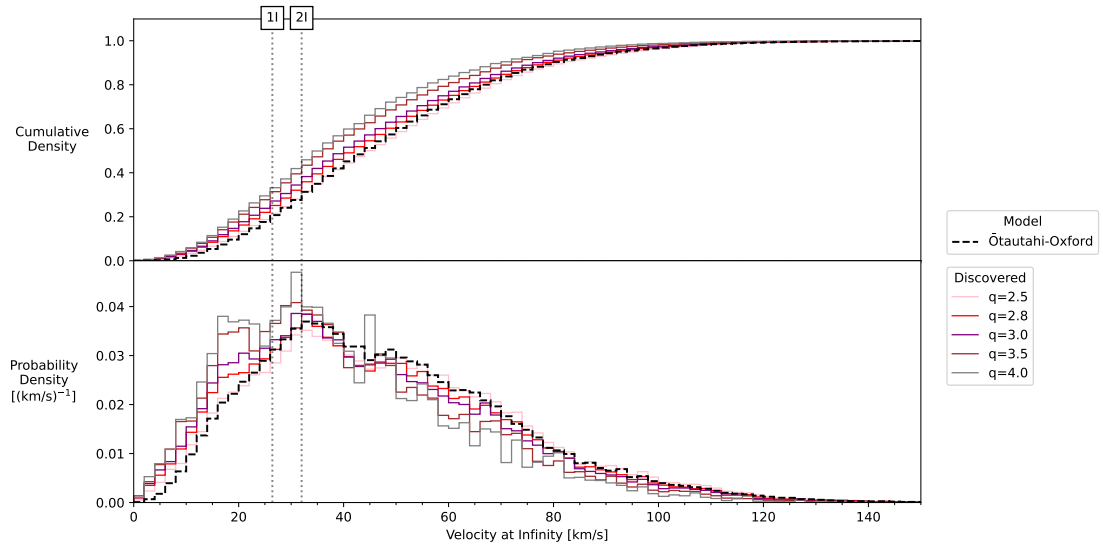

(c) The v_∞ distribution for discovered ISOs drawn from a range of size distributions.

Figure 4.2: Predicted velocity distributions of the discovered ISO population for different H distributions. There is little difference, but steeper H distributions (higher q_s) result in more high-velocity ISOs discovered. The underlying ISO population v_∞ distribution is plotted in for comparison (dashed line labelled Ōtautahi-Oxford). Taken from Dorsey et al. (2025).

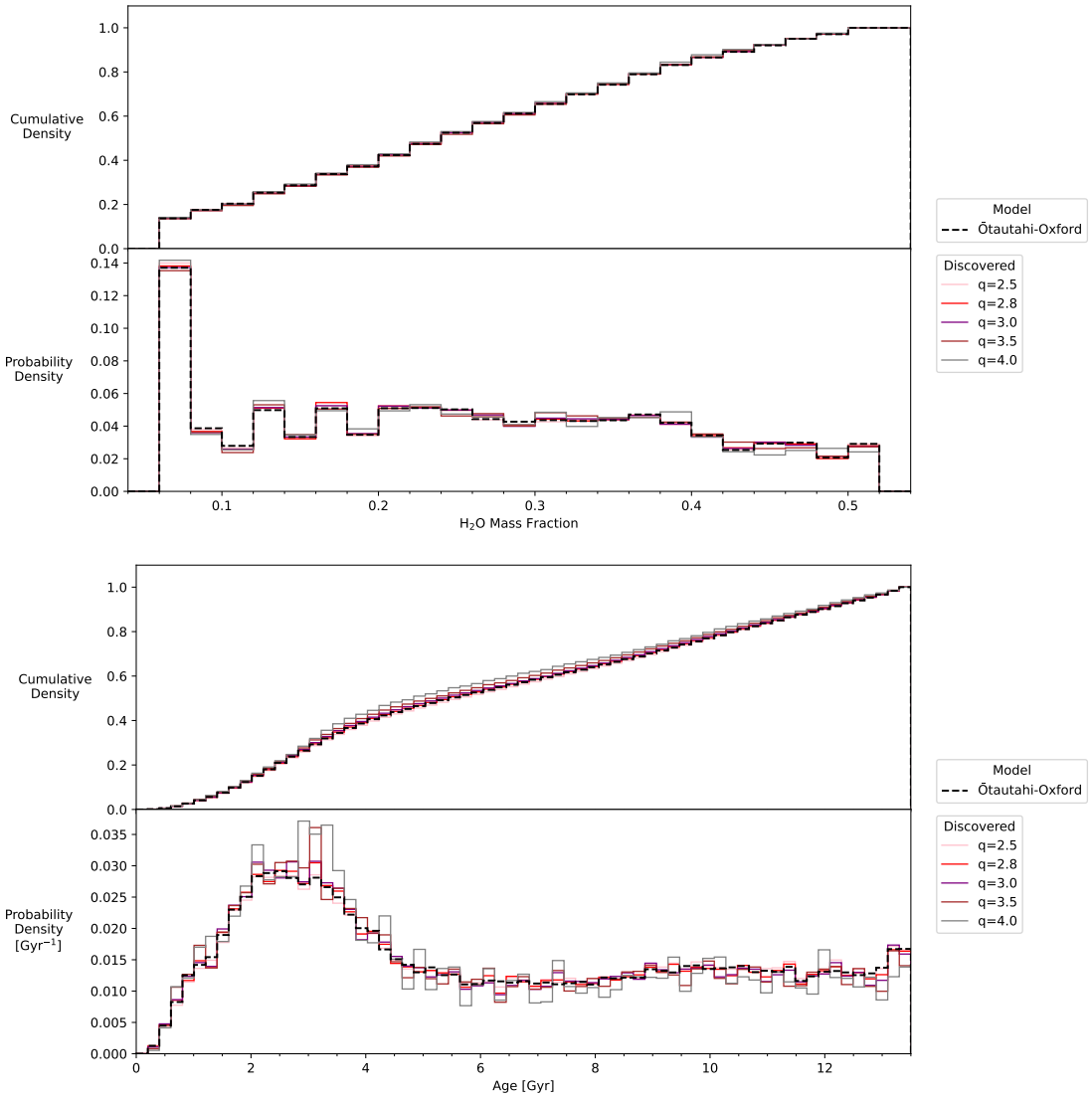

Figure 4.3: Predicted distributions for discovered ISOs in water mass fraction (above) and age (below), with the underlying ISO population for comparison (dashed line labelled Ōtautahi-Oxford). All detected H distributions are essentially indistinguishable from the underlying population.

Fig. 4.3 shows the distributions in water mass fraction and age of the discoverable populations for different H distributions along with the underlying ISO population. For both water mass fraction and age, the discoverable populations are essentially indistinguishable from the underlying population. This implies the sample of ISOs the LSST will discover will be an unbiased sampling of the age and composition distributions.

Figure 4.4 shows the H distribution of the discoverable populations for each

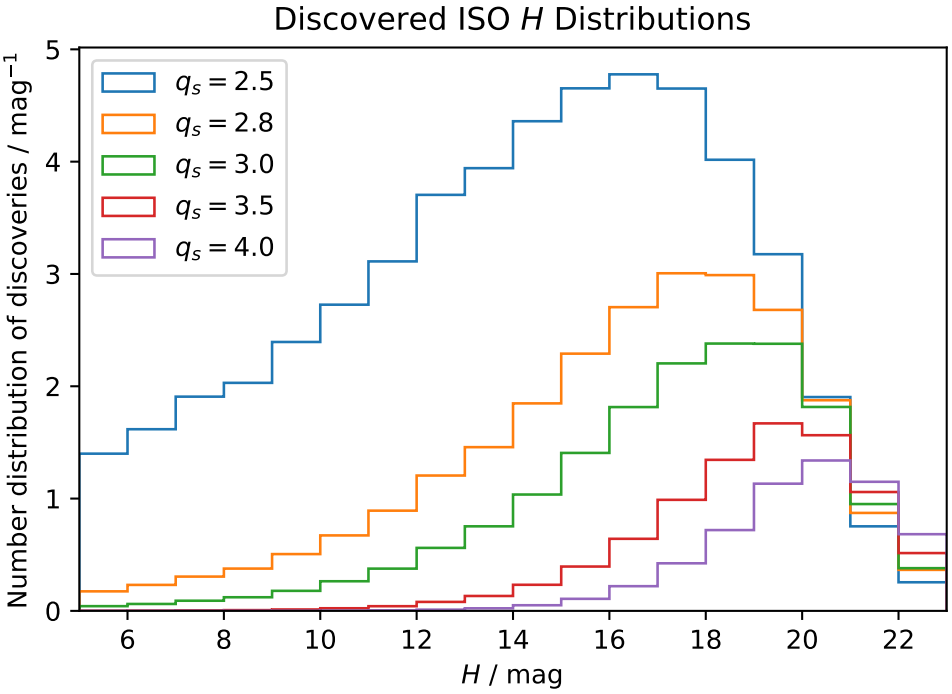

Figure 4.4: Predicted number distributions of discovered ISOs for different H distributions, assuming $n_{22} = 0.1\,\mathrm{au}^{-3}$.

underlying H distribution. As the underlying H distribution becomes flatter (lower q_s), the H distribution of the discoverable population becomes weighted towards lower values of H. These distributions are scaled such that the integral under the curve between two vales of H is equal to the expected number of discoveries in that H range assuming a value for n_{22} of $0.1\,\mathrm{au}^{-3}$.

Fig. 4.4 shows that the non-cometary ISOs the LSST is predicted to find have generally lower values of H than 1I/'Oumuamua ($H \simeq 22$; Meech et al. 2017), including down to $H \lesssim 8$ for lower values of q_s. In the Solar System these values of absolute magnitude correspond to large trans-Neptunian objects, $\gtrsim 100\,\mathrm{km}$ in diameter, and it is interesting that no ISO of this size has been discovered yet in existing surveys such as Pan-STARRS. It could simply be that the depth and cadence of the LSST makes it more sensitive than existing surveys to these low values of H. However, it may instead be the first hint that the ISO size distribution is steep, with a high value of q_s, making large ISOs exceedingly rare. Discerning between these two possibilities would require a precise characterisation of a existing

survey's sensitivity to ISOs of different sizes, similar to the work of Dorsey et al. (2025) on LSST. Fortunately, soon the LSST itself will become an existing survey, and Dorsey et al. (2025) has already determined that only a small number of discovered ISOs are needed to constrain the size distribution slope.

Finally, the number of ISOs that will be detected by LSST can be predicted. This is simply the integral of the number distribution of discovered ISOs for each H distribution slope in Fig. 4.4. As with all quantities in Section 4.3, the number of ISOs detected is simply proportional to the underlying number density of ISOs, which is highly unconstrained. We have assumed a value of $n_{22} = 0.1\,\mathrm{au}^{-3}$, however as this value is better constrained as further ISO discoveries occur our estimates can be simply rescaled. These are listed in Table 4.1.

q_s	ISOs Discovered
2.5	51.4
2.8	24.4
3.0	16.8
3.5	8.71
4.0	5.86

Table 4.1: Prediction for numbers of ISOs discovered in LSST for different H distribution slopes q_s, assuming an underlying density of $n_{22} = 0.1\,\mathrm{au}^{-3}$ to which these values are simply proportional.

4.5 Conclusion

Over the thesis so far I have developed a predictive Bayesian framework for the study of ISOs. In Chapters 2 and 3, by combining models of protoplanetary disks and assumptions about Galactic dynamics with stellar populations fit to surveys of Milky Way stars, I have predicted the chemodynamics of ISOs both in the Solar neighbourhood and across the Milky Way disk. With the work of this Chapter and the survey simulator of Dorsey et al. (2025), the survey biases present in the detectable population of ISOs have been estimated, producing a complete pipeline that produces testable predictions about the detectable ISO population from models

of planetesimal formation, planetary architecture, and Galaxy physics. Thus, when LSST begins to find ISOs starting this year the discovered sample can be used to test models across astrophysical scales.

With just the first year of LSST data, both the underlying density of ISOs n_{22} and their size distribution slope q_s will be constrained. Dorsey et al. (2025)'s Fig. 10 shows that the ISO discovery rate will be almost constant with no preference for any particular year of the survey[4], meaning the full-survey predictions of Fig 4.4 and Table 4.1 can be scaled by a tenth to get the first-year predictions. The number and H values of these 0–5 first-year ISOs will follow a Poisson point process distribution (Sec. 2.2.2) and thus can be compared to the scaled predicted distributions of Fig. 4.4 using likelihood methods (Sec. 3.4.3) to simultaneously constrain n_{22} and q_s. With this method I could constrain n_{22} and q_s even in the event that no ISOs are found.

As the LSST continues past its first year and more ISOs are discovered, the constraints on n_{22} and q_s will improve. Additional science can be done on the other measured properties of ISOs: their velocities and compositions. Pre-encounter asymptotic velocities will be known for all discovered ISOs as fitting an orbit is a necessary step for classifying an object as interstellar. Thus I will be able to place the velocity of each discovered ISO on my Fig. 3.4 and compare it to the moving groups, the overdensities in velocity space sculpted by the Galactic spiral arms and bar (Sec. 3.2.4). 1I and 2I each belonged to a moving group (Sec. 3.4.1), and Fig. 4.2 implies that the majority of the LSST ISO sample will be members of these overdensities as well. What would be more interesting however would be if an ISO was found in one of the gaps between the moving groups: being dynamically disfavourable regions, an ISO here may have been placed there by a recent interaction with a molecular cloud (Pfalzner et al. 2020). Finally, the chemical composition of an ISO can be directly related back to the chemical abundances of its parent star and planetary system, many kiloparsecs away and potentially long dead (Sec. 2.3.2). Though the chemical model used for the work in this thesis is unsophisticated, I

[4]During template building in the first six months of the survey ISOs may not be discovered immediately, but they will be found in data reprocessing for DR1 at the end of the first year (Schwamb et al. 2021)

plan to add complexity and doing so will allow an ISO's composition to tell us its formation location within the protoplanetary disk (Seligman et al. 2022). This will give us valuable insights into planetesimal formation and giant planet migration.

Later this year the LSST will begin a revolution in Solar System science. Though the predicted numbers of ISO discoveries of my Table 4.1 look small compared to the expected ~ 6 million new asteroids (LSST Science Collaboration et al. 2009, their Table 5.1), each and every ISO we discover will advance our understanding of planetary systems and the Galaxy we call home.

BOOM BOOM BOOM BOOM,
BOOM BOOM BOOM,
BOOM BOOM... BOOM BOOM...
BOOM BOOM BOOM.

— Private S. Baldrick's *The German Guns**

5

Interstellar Objects and Fast Radio Bursts

The work described in this chapter constitutes part of that published in Pham et al. (2024), of which I am co-first author. My contribution was the calculation of the expected rate of ISO–NS collisions laid out here in Section 5.2, predictions for the distribution of ISO–NS FRBs in Section 5.3, and the suggestion of the discovery of a binary ISO cause of FRB 200428 in section 5.4.

5.1 Introduction

The only population of ISOs that can be directly observed are those that pass through the inner Solar System. I have shown that these ISOs have origins around stars across the Galaxy (§2.3.2 and §3.2.5) with a wide range of chemical compositions and ages (§3.3.1). However, being ubiquitous products of star and planetary system formation I expect ISOs to exist not just in the solar neighbourhood but across the Milky Way and in all galaxies. I expect the ISO population to vary across the Milky Way due to the stellar metallicity gradient (§2.4.1) and therefore the ISO population will vary between galaxies too. Though not directly observable, under the right circumstances these ISOs outside the solar neighbourhood may be inferred to exist and studied, even at extragalactic distances. In this Chapter I

*The examiners are advised not to enquire what the *S.* stands for.

explore one of these circumstances: the collision between an ISO and a neutron star (NS), which may be a cause of fast radio bursts (FRBs).

FRBs, first discovered in 2007 (Lorimer et al. 2007), are gigahertz-frequency millisecond-duration radio transients. FRBs are largely extragalactic phenomena (Mannings et al. 2021) with only one known to originate in the Milky Way (Bochenek et al. 2020; CHIME/FRB Collaboration et al. 2020). Their origins are undetermined with many hypotheses proposed (Platts et al. 2019; Zhang 2020) but due to the short durations and high energies involved compact objects such as neutron stars are often invoked. Most discovered FRBs are detected by CHIME (the Canadian Hydrogen Intensity Mapping Experiment; CHIME Collaboration et al. 2022) due to its wide field of view; the first year of CHIME FRB detections was published in CHIME/FRB Catalog 1 (CHIME/FRB Collaboration et al. 2021).

The majority of FRBs appear to be one-off events however a handful of sources have been found to stochastically repeat (CHIME/FRB Collaboration et al. 2019). Differences in the emission properties (Pleunis et al. 2021) and environments (e.g. properties of the host galaxy; Gordon et al. 2023) of repeating and non-repeating FRBs may imply they are produced by different mechanisms. This however is a matter of ongoing debate. Both Lu et al. (2020b) and Kirsten et al. (2024) find that the energy distribution of individual bursts from repeaters have the same power-law distribution as bursts from non-repeaters, implying a common emission mechanism. This may mean that FRB sources that are apparently non-repeating are just those with only one detected burst. Alternatively, the variation in environment just within the sample of known repeating sources (Marcote et al. 2022; Michilli et al. 2023) may be evidence that many emission mechanisms contribute to an origin-diverse collection of high-energy, millisecond-duration radio phenomena, umbrellaed under the term FRB.

One suggested mechanism to produce an FRB-like signal is a head-on collision between a NS and an unbound small body, which would generate a radio signal of duration and luminosity consistent with observed FRBs (Geng and Huang 2015; Dai et al. 2016). It is known that NSs can have bound planetary systems (Wolszczan

and Frail 1992), however the slow infall of a small body bound to NS is thought to produce a different signal, such as that found by Brook et al. (2014). Previous work (Dai et al. 2016; Bagchi 2017) invoked this emission mechanism with NSs intruding into the debris disks of other stars to explain repeating FRBs specifically, but this was contested as requiring an unfeasibly high number density of small bodies to match the observed repeat rate of repeating FRBs (Smallwood et al. 2019). This mechanism however remains a valid way for a single small body–NS collision to produce a single non-repeating FRB, if a source of small bodies can be found.

In this Chapter I explore the implications of the population of ISOs being this source of small bodies. In §5.2 I estimate the rate of ISO–NS collisions in the local Universe and discuss potential sources of uncertainty in this estimate; I find that the rate matches the observed FRB rate, making ISO–NS collisions a feasible cause of at least some FRBs. In §5.3 I make testable predictions about the distribution of ISO–NS FRBs, assuming only what is known about the distributions of ISOs and NSs, then compare these with predictions for other hypothesised sources of FRBs to the observed FRB distribution. In §5.4 I suggest that the Galactic FRB FRB 200428 may have been caused by a collision with a binary ISO and discuss the implications of this for ISO formation, and finally in §5.5 I discuss the work of this Chapter in context and conclude.

5.2 The ISO–NS Collision Rate

In this section I first derive an estimate for the ISO–NS collision rate and compare this the observed FRB rate. I then discuss sources of uncertainty in this estimate.

5.2.1 Derivation

I start by deriving the rate of ISOs colliding with a single NS. In the vicinity of a NS of mass $M_{\rm NS} \simeq 1.4$ M$_\odot$ (Weisberg and Taylor 2003), ISOs follow hyperbolic trajectories defined by their impact parameter B and relative speed at infinity v_∞, related to the periastron q by $B^2 = q^2(1 + 2GM_{\rm NS}/qv_\infty^2)$, as derived in §4.3.2. An ISO impacts the NS surface when it has a periastron less than the NS radius

$R_{\rm NS} \simeq 10\,{\rm km}$ (Miller et al. 2021), therefore the cross-section of ISOs with a relative speed at infinity v_∞ colliding with the NS surface is

$$\begin{aligned}\sigma = \pi B^2 &= \pi R_{\rm NS}^2 \left(1 + \frac{2GM_{\rm NS}}{v_\infty^2 R_{\rm NS}}\right) \\ &\approx 10^9\ {\rm km}^2 \left(\frac{M_{\rm NS}}{1.4\ {\rm M}_\odot}\right)\left(\frac{R_{\rm NS}}{10\ {\rm km}}\right)\left(\frac{v_\infty}{100\ {\rm km\ s^{-1}}}\right)^{-2} .\end{aligned} \tag{5.1}$$

Due to the high mass and small radius of the neutron star, impacting ISO orbits are highly gravitationally focussed and $1 \ll 2GM_{\rm NS}/R_{\rm NS}v_\infty^2$ can be assumed.

For this collision cross section, the flux of ISOs onto a single NS is given by $\Gamma = \langle n_{\rm ISO} v_\infty \sigma \rangle$, averaged over the velocity distribution. To estimate the density and velocity distribution of ISOs around NSs I make a number of assumptions. Since ISOs are an abundant, expected product of planetary systems (Shoemaker and Wolfe 1984; Stern 1990; Jewitt and Seligman 2023), I first assume that planetary systems and therefore ISO populations are present in galaxies throughout the Universe. The solar neighbourhood population of ISOs larger than 1I/'Oumuamua has a number density of $n_{\rm ISO} \sim 10^{15}\ {\rm pc}^{-3}$ (Do et al. 2018), and a velocity distribution with a width of approximately 50 km s^{-1} (equal to that of the stellar population; §3.3.1, Fig. 3.4). I assume the population of ISOs around all neutron stars shares these properties. Since upon creation NSs receive a large natal kick on the order of $\sim 100\,{\rm km\ s^{-1}}$ (Lyne and Lorimer 1994; Hobbs et al. 2005), and as this is significantly larger than the width of the ISO velocity distribution, I assume this value for the relative speed v_∞ of ISOs encountering NSs.

Thus, taking $n_{\rm ISO} \sim 10^{15}\ {\rm pc}^{-3}$, $v_\infty \sim 100$ km s^{-1} and $\sigma \sim 10^9$ km^2 gives the collision rate of ISOs onto a single NS as

$$\Gamma = n_{\rm ISO} v_\infty \sigma \sim 10^{-7}\,{\rm yr^{-1}} . \tag{5.2}$$

This timescale is far longer than that of repeating FRBs, which occur on timescale of weeks. Thus, ISO–NS collisions cannot explain repeating FRBs, and ISO–NS collisions cannot be the only cause of FRBs. This is not unexpected: as discussed in §5.1 there is evidence that multiple different mechanisms contribute FRB-like signals to the observable population, especially between repeaters and non-repeaters.

FRBs are detected over cosmological distances, with the most distant being detected at a redshift of $z \simeq 1$ (Ryder et al. 2023), thus the cosmological rate of ISO–NS collisions must be considered. Stars over $9M_\odot$ make up $\sim 0.5\%$ of all stars formed (assuming the universal initial mass function of Kroupa 2001), have lifetimes $\lesssim 0.1$ Gyr and largely form neutron stars upon their deaths (Heger et al. 2003). Thus with approximately 10^{11} stars (e.g. Licquia and Newman 2015), the Milky Way contains about $N_{\rm NS} \sim 10^9$ NS. For a number density of Milky Way-mass galaxies of $n_{\rm Gal} \sim 10^7\,{\rm Gpc}^{-3}$ (Blanton et al. 2003), the cosmological rate of ISO–NS collisions is

$$R_{\rm col} = \Gamma \cdot n_{\rm Gal} \cdot N_{\rm NS} \sim 10^9\,{\rm Gpc}^{-3}\,{\rm yr}^{-1}. \tag{5.3}$$

FRBs produced by ISO–NS collisions are thought to be strongly beamed by a factor $f \sim 10^{-2}$ (Geng and Huang 2015; Dai 2020) meaning if every 1I-sized ISO–NS collision produced an FRB the observable rate of ISO–NS collisions would be

$$R_{\rm obs} = fR_{\rm col} \sim 10^7\,{\rm Gpc}^{-3}\,{\rm yr}^{-1}. \tag{5.4}$$

This is comparable to the observed FRB rate of $(7^{+9}_{-6}) \times 10^7\,{\rm Gpc}^{-3}\,{\rm yr}^{-1}$ (Bochenek et al. 2020). Since ISO–NS collisions are expected to produce observable FRB-like signals, and the rates of observable ISO–NS collisions and observed FRBs are comparable, ISO–NS collisions represent a feasible origin for at least a subset of FRBs.

5.2.2 Sources of Uncertainty

The most significant source of uncertainty in this estimate is the average number density of ISOs around neutron stars. The density of ISOs has only been measured for the solar neighbourhood, and this estimate has an order of magnitude uncertainty (Do et al. 2018). Additionally, the density around different neutron stars across the local Universe may vary significantly. We expect the density of ISOs to vary both across the Milky Way (§2.4.1) and between different galaxies due to a dependence of small body formation on stellar metallicity (Williams et al. 2022; Andama et al. 2024).

Additionally, the natal kick that NSs receive (Hobbs et al. 2005; Chatterjee et al. 2005) can place them on an orbit removed from their galaxy's stars and ISOs,

or completely eject them. Sweeney et al. (2022) model the Milky Way, predicting that 40% of NS are completely ejected and the remaining NS occupy a disk with a vertical scale height five times that of the stellar disk. I expect ISOs to retain the same spatial distribution as their parent stars (§2.3.2 and §3.2.5), therefore NS natal kicks could reduce the expected ISO–NS collision rate. This however will not be a major effect in elliptical galaxies, which make up $\sim 40\%$ of galaxies in the local universe with r-band absolute magnitude $M_r < -19$ (Lintott et al. 2008).

An additional issue lies in ensuring I am comparing like for like: The rate of observable ISO–NS collisions of $\sim 10^7$ Gpc^{-3}yr^{-1} that I calculate in Section 5.2 is not directly comparable to the rate of FRBs of $(7^{+9}_{-6}) \times 10^7$ Gpc^{-3} yr^{-1} inferred by Bochenek et al. (2020). The rate I calculate corresponds to 1I-sized ISOs colliding with all NSs, whereas the observable FRB rate inferred by Bochenek et al. (2020) corresponds to FRBs of at least the energy of FRB 200428, with an isotropic-equivalent energy release of 2×10^{35} erg. Ideally I would use a combination of the ISO size distribution and NS magnetic field distribution to calculate the distribution of ISO–NS collision energies, and compare the observable ISO–NS collision rate at the energy of FRB 200428. However, neither the ISO size distribution nor NS magnetic field strength distribution are well constrained, making this calculation beyond the scope of currently possible work.

5.3 Testable Predictions

As noted above ISO–NS collisions cannot be only source of FRBs, however I can make testable predictions about the distribution of ISO–NS FRBs assuming nothing about the emission mechanism by which an ISO–NS collision produces an FRB, by just considering the distribution of their ISO and NS progenitors. Firstly, I predict the existence of differences between the properties of repeating and non-repeating FRBs. Since ISO–NS cannot cause repeating FRBs, repeating FRBs must be have a different source and thus must have different properties. This seems to be confirmed by Pleunis et al. (2021) who find differences in burst morphology between repeating

and non-repeating FRBs, as well as Gordon et al. (2023) who find differences between the star formation rates of repeating and non-repeating FRB host galaxies.

Secondly, I predict ISO–NS FRBs to not be correlated with star formation. This is because both ISOs and NSs are long-lived, so the populations of both will build up over cosmic time. This is in contrast to other hypothesised progenitors of FRBs, such as magnetars (e.g. Metzger et al. 2019; Wadiasingh and Timokhin 2019; Margalit et al. 2019). These are NSs with extreme magnetic fields which decay on timescales of only $\sim 10\,\mathrm{kyr}$ (Reisenegger 2003; Mondal 2021), meaning magnetars will only be present when and where star formation is actively occurring. Having long-lived progenitors, ISO–NS FRBs will originate from all galaxies including those that are quiescent, as well as regions of low star formation within star-forming galaxies. This is corroborated by findings of Bhandari et al. (2020) and Mannings et al. (2021), both of which have localised single-burst FRBs to both such environments. Even if not caused by ISO–NS collisions, these FRBs are unlikely to have short-lived progenitors. One FRB source has been even been localised to a globular cluster with age $\sim 9\,\mathrm{Gyr}$ (Kirsten et al. 2022), implying a very old progenitor. This however is a repeating source, and displays periods of high burst rates (e.g. 53 bursts in 40 min; Nimmo et al. 2023) which are difficult to explain as ISO–NS collisions.

Since FRBs can be observed out to redshifts of $z \simeq 1$, the cosmological evolution of the FRB rate can be estimated and compared to the cosmic star-formation rate. The redshift of an FRB is inferred from its dispersion measure, a quantity equal to the column density of free elections between the source and observer, measured for every detected FRB. This is done using a relation between redshift and dispersion measure fit to the relatively small number of FRBs localised to host galaxies with a measured redshift (Deng and Zhang 2014; Macquart et al. 2020). Again since both ISOs and NSs are long-lived and their populations build up over time, I predict that the ISO–NS collision rate should increase over cosmic time and thus decrease with redshift, decoupled from the cosmic star formation rate which increases with redshift up to $z \simeq 2$ (Madau and Dickinson 2014). This matches the literature with many studies finding the non-repeating FRB rate to be inconsistent with the cosmic star

formation rate (Lin and Zou 2024; Lin et al. 2024), decreasing with redshift (Tang et al. 2023; Chen et al. 2024), or being consistent instead with the integrated mass of stars formed over time (Hashimoto et al. 2020b, 2022). Other studies including repeating FRBs find similar results (Zhang and Zhang 2022; Zhang et al. 2024). Each of these studies imply that the majority of FRB progenitors are long-lived.

Each of the above predictions can be made assuming nothing about the emission mechanism. In addition to these, in Pham et al. (2024) my co-author Dang Pham uses the emission mechanism of Geng and Huang (2015) and Dai et al. (2016) to relate the observed FRB durations and energies to ISO sizes. Firstly he finds that the durations of observed FRBs correspond to sizes of ISOs broadly consistent with the sizes of 1I/'Oumuamua and 2I/Borisov, the two observed ISOs. Secondly he finds that the power-law energy distribution of observed FRBs implies a ISO power-law size distribution with a slope consistent with Solar System small body populations.

5.4 A Binary ISO?

FRB 200428 is the only observed FRB known to originate from within our own Galaxy and have a progenitor identified: the magnetar SGR 1935+2154. Dai (2020), one of the main proponents of the small body–NS mechanism for producing FRBs, interpreted FRB 200428 as collision between the magnetar and single small body. However, they used an obsolete value for the tensile strength of a colliding small body, motivating a second look at the potential collisional origin of FRB 200428.

Many recent works studying small body–NS collisions (Geng and Huang 2015; Dai et al. 2016; Siraj and Loeb 2019a) copy the value of the tensile strength of a colliding small body from Colgate and Petschek (1981): a high value of $\sim 10^9$ Pa, measured from Fe–Ni meteorites, which assumes small bodies are monoliths. However, it now known that Solar System bodies are rubble piles (Davis et al. 1985; Weissman 1986; Lauretta et al. 2017) with significantly lower tensile strengths of ~ 500 Pa, measured from cometary fragmentation events (Greenberg et al. 1995; Asphaug and Benz 1996) and asteroid rotation curves (Harris and Pravec 2006).

This is the value used in Pham et al. (2024), where we derive the duration of an FRB caused by an ISO–NS collision to be directly related to the size of the ISO by

$$\Delta t \simeq 4\,\mathrm{ms}\left(\frac{R}{1\,\mathrm{km}}\right)^{\frac{4}{3}} \tag{5.5}$$

for a NS of mass $1.4M_\odot$ and a small body of density $3\,\mathrm{g\,cm^{-3}}$ and tensile strength 500 Pa. Using this relation, I reconsider the case study of FRB 200428.

Unlike most FRBs (Pleunis et al. 2021) FRB 200428 showed a strong bimodality, consisting of two highly-distinct subbursts of length 0.6ms and 0.3ms separated by a large gap of no signal 29ms long (See Fig. 1 of CHIME/FRB Collaboration et al. 2020). Dai (2020) proposed that this structure was caused by a single small body which fragmented into two major parts due to tidal disruption during infall. However, with a modern understanding of small bodies as low-tensile-strength rubble piles, this cannot be the case. As a rubble-pile ISO approaches the NS the tidal forces continually increase, causing a series of rapid sequential fragmentation events that disrupt the ISO completely into a mostly-homogeneous stream of material shortly before impact occurs.[1] This will produce an FRB with very little substructure.

Instead, for FRB 200428's origin to be collisional, it must have been caused by a collision of the magnetar with a binary ISO: two distinct but gravitationally bound bodies of radius 200 m and 100 m respectively, with a separation of several kilometres. Binaries are common within the Solar System (Margot et al. 2002; Walsh et al. 2008; Fraser et al. 2017), but the potential existence of binary ISOs presents a fascinating opportunity for study.

If formed as a binary before ejection from their home planetary systems, the ejection mechanism must be gentle enough to allow the constituent bodies to remain gravitationally bound. McDonald and Veras (2023) find that ejection by scattering off planets disrupts all binaries, however other ejection mechanisms such as stellar flybys (Pfalzner et al. 2021b) or the effect of the Galactic tide on the

[1]The difference between this scenario and fragmentation events observed in the Solar System such as that of Shoemaker-Levy 9 by Jupiter (Asphaug and Benz 1994) and the Kreutz family of sungrazers (Sekanina 2001) is that these objects do not collide with the larger body immediately after fragmentation. This allows them to instead disrupt only partially then continue orbiting, allowing time for their fragments to drift apart.

outer edges of exo-Oort clouds (Brasser et al. 2010; Kaib et al. 2011) may be sufficiently gentle. Alternatively, binaries could perhaps be formed in the tidal disruption events that may be the source of some ISOs (Walsh and Richardson 2006; Ćuk 2018; Zhang and Lin 2020).

An interesting prediction of connecting FRB subbursts to binary ISOs is that they should be largely limited to two subbursts, since triple (and higher) systems are much rarer: in the Solar System only three triple asteroids and two triple trans-Neptunian objects are known (Winter et al. 2020; Nelsen et al. 2025). This seems to be the case: of the non-repeating FRBs in the CHIME/FRB Catalog 1 there are 450 events consisting of one burst, 19 events with two subbursts, and only 5 events with more than two subbursts. As discussed above ISO–NS collisions cannot be the source of all FRBs, but if they are the source of some then FRBs may potentially be a probe for studying ISOs well beyond the limits of the Solar System.

5.5 Discussion and Conclusion

The study of both FRBs and ISOs is currently limited by a lack of well-characterised examples. CHIME/FRB Catalog 1 consists of only the first year of data, so there remains 6 years of CHIME FRB detections currently unpublished. A larger sample of localised FRBs will be especially useful, as these can tell us about the environments of FRBs, giving clues to their origins. FRBs will be localised in current survey such as CHIME, EVA and ASKAP (Michilli et al. 2023; Marcote et al. 2022; Bhandari et al. 2020) and upcoming surveys such as CHORD and SKA (Vanderlinde et al. 2019; Hashimoto et al. 2020a). The sample of known ISOs is even smaller, but this is soon to change with the imminent start of the LSST (Chapter 4). A larger sample of ISOs will allow the constraining of the solar neighbourhood ISO size distribution, and this could be compared to the distributions of FRB durations and energies predicted to result from ISO–NS collisions by Pham et al. (2024).

Many origins for FRBs have been proposed, and many remain feasible. The diversity in environments and properties of observed FRBs may imply that multiple different pathways contribute to our growing sample. The pathway described here

could be one of them. In this Chapter I have shown ISO–NS collisions to be a feasible pathway to produce a number of observable FRB-like signals comparable to the observed FRB rate. Even if the majority of observed FRBs are not caused by ISO–NS collisions, since both NSs and ISOs are ubiquitous products of star formation these collisons will occur, and under the mechanism of Geng and Huang (2015) and Dai et al. (2016) they will produce observable FRB-like signals. Under these assumptions, at least a fraction of FRB-like signals must be caused by ISO–NS collisions.

If FRBs can be confirmed to have origins in ISO–NS collisions, their signals will allow us to study ISOs from afar, well outside the Solar System and even outside the Milky Way. Though planetary system formation appears to be ubiquitous in our Galaxy, this presents the opportunity of testing this assumption out to redshifts of $z \simeq 1$. If it is indeed ubiquitous across the Universe, every galaxy will have its own galactic population of ISOs.

5.6 Postscript

The argument I make in this Chapter is remarkably similar to that made by Whipple (1939), who argues that collisions between stars in other galaxies are a feasible cause of supernovae. I only discovered this work while writing the introduction to this thesis, long after Pham et al. (2024) was published, by way of Fred Whipple's better-known work on comets (discussed in §1.1.1). Whipple was of course wrong, as we now know that non-type Ia supernovae are caused by a variety of core-collapse mechanisms in single stars (Trimble 1982; Janka 2012), but it is clear in his writing that being in error is a possibility he is open to and would accept with dignity—an inspiration to all of us, from DPhil candidate to Harvard professor.

Well, the thing about a black hole - its main distinguishing feature - is it's black.
And the thing about space, the colour of space, your basic space colour, is black.
So how are you supposed to see them?

— Holly, *Red Dwarf*

6 The Milky Way Black Hole Gradient

The work described in this chapter constitutes a large part of an as-of-yet unpublished paper, the entirety of which I led.

6.1 Introduction

The model of the Milky Way disk's *sine morte* stellar population which I calculated in Chapter 2 can be used for more than just the prediction of the distribution of ISOs. Including the distribution of dead stars, this model is also useful to study the distribution of stellar black holes, and this is what I do in this Chapter.

Isolated stellar black holes in the Milky Way, with negligible radiation due to negligible accretion (Fender et al. 2013), are currently only detected by their gravitational effect on the light from other stars: gravitational microlensing. Microlensing surveys[1] detect massive objects, including black holes, by observing the increase in brightness of a background source star caused by the gravitational magnification of a massive foreground object passing in front of them. These surveys are generally pointed towards the Galactic centre, through the inner Galactic disk, to take advantage of the high density of background stars as sources.

[1] e.g. OGLE (Udalski et al. 1992, 2015), MACHO (Alcock et al. 1993), EROS (Aubourg et al. 1993), MOA (Bond et al. 2001), and KMTNet (Kim et al. 2016).

However, black holes are yet to be frequently identified with certainty in microlensing surveys. Due to degeneracies between the physical properties of a lens in the first-order light curve, secondary effects that are difficult to detect must be measured in order to characterize a lens. These include the effect of annual parallax (the motion of the observer around the Sun) on the light curve (Gould 1992), or the change in the apparent position of the source centroid during the lensing event (Hog et al. 1995; Walker 1995). Both must be combined to measure the mass and distance of a lens. This degeneracy between lens mass and distance means that despite the detection of tens of thousands of microlensing events (Wyrzykowski et al. 2023), with $\sim 1\%$ of them expected to be due to black holes (Gould 2000), only one stellar-mass black hole has been detected and characterized using high-precision Hubble astrometry (Sahu et al. 2022; Lam and Lu 2023).

The rate of detection of black holes by microlensing depends on the density and distribution of black holes in the Galaxy. Several works have estimated the distribution of black holes in the Milky Way for this purpose (Shapiro and Teukolsky 1983; Wyrzykowski et al. 2016; Moniez et al. 2017; Wiktorowicz et al. 2019; Sajadian and Sahu 2023), but each assumes that the distribution of black holes is identical to the distribution of currently living stars in the Galaxy. This is not realistic: being dead stars, the relationship between the number density of black holes and living stars in a stellar population depends on the age distribution, which changes with position in the Galaxy. The fraction of stars able to form black holes additionally depends on the metallicity distribution of the population (Heger et al. 2003), and natal kicks may dramatically change the vertical distribution of the black holes away from the Galactic disk midplane (Sweeney et al. 2022).

In this work, I use the *sine morte* stellar population model I calculated in Chapter 2 to estimate a more realistic model of the distribution of black holes in the Milky Way. From the *sine morte* population I can infer the fraction of dead stars directly, and I include a metallicity-dependent black hole formation model. In §6.2 I discuss these models and the assumptions I make in using them, then in §6.3 I show that my model predicts a gradient in the ratio of black holes to

stars with distance from the Galactic centre. In §6.4 I discuss the implications of this gradient for microlensing surveys with a focus on the planned *Nancy Grace Roman Space Telescope* (Spergel et al. 2015), and estimate that it will be able to accurately characterise slightly fewer black holes than previously predicted, a difference that is negligible compared to other uncertainties. In §6.5 I conclude by discussing potential improvements to this model and other uses of the *sine morte* population for studying stellar remnants such as white dwarfs and neutron stars.

6.2 Method

Similar to ISOs, which remain when their parent stars die, it is the *sine morte* population that must be used to estimate the distribution of stellar black holes. This because stellar black holes are dead stars, thus the distribution of dead stars must be found.

I calculate the fraction of the *sine morte* stellar population that would form a black hole on death. I use a model based on Heger et al. (2003), where stars form black holes when they have a zero-age main-sequence mass (ZAMS) over $25M_\odot$ and metallicity less than Solar, $Z < Z_\odot$, or equivalently [Fe/H] < 0. The reason for this metallicity cutoff in black hole formation is that high-metallicity stars experience mass loss due to line-driven winds, resulting in a lower mass at the end of their lives, with less mass available for forming a black hole. This means that in reality instead of an exact cutoff at [Fe/H] $= 0$, the ZAMS mass required to form a black hole increases sharply around Solar metallicity (Elbert et al. 2018), causing a sharp decrease in black hole formation. I assume the ZAMS distribution of the *sine morte* population follows the universal initial mass function of Kroupa (2001), which gives the fraction of stars with [Fe/H] < 0 massive enough to form black holes as 1.34×10^{-3}.

Though Heger et al. (2003) focus on single massive stars, it is now thought that the majority of massive stars form in binaries (Mason et al. 2009; Sana and Evans 2011; Sana et al. 2012). I assume that the same trend of lower black hole formation efficiency at higher stellar metallicity holds, as massive high-metallicity

stars in binaries will also lose mass due to winds. These binary star systems will still produce a black hole population dominated by single black holes, as the majority of these binaries either merge or are disrupted before or on the formation of a black hole (Wiktorowicz et al. 2019). I assume a one-to-one ratio of the number of *sine morte* stars which meet the conditions to form a black hole and the number of black holes, however merging binary systems may change this. A merger of two stars individually meeting the conditions to form a black hole may form only one black hole, and the merger of two stars individually under the mass threshold may form a star above the mass threshold which then forms a black hole. Mergers of black holes themselves are rare when considering a single galaxy, occurring on cosmic scales at rates measured in $\mathrm{yr}^{-1}\,\mathrm{Gpc}^{-3}$ (Dominik et al. 2013). Stellar-mass black holes can also form in the merger of binary neutron stars if the remnant is sufficiently massive (Abbott et al. 2017; Margalit and Metzger 2017). However, the rate of formation by this pathway is low, with a Galactic rate of binary neutron star mergers of $\sim 10\,\mathrm{Myr}^{-1}$ (Chruslinska et al. 2018). I assume each of these processes have a negligible effect on the number and spatial distribution of black holes.

I assume that the lifetimes of stars large enough to form black holes ($\lesssim 10\,\mathrm{Myr}$, Brott et al. 2011) are sufficiently small, compared to the average stellar lifetime, that I do not need to account for the delay between their birth and their death. This means I can assume any star born that would go on to form a black hole has already done so. I also ignore pair-instability supernovae, which do not form black holes (Rakavy and Shaviv 1967; Fraley 1968). Only extremely high mass, low metallicity stars can undergo a pair-instability supernova, making them very rare. At zero metallicity, only stars in the ZAMS range $140 - 260 M_\odot$ undergo pair-instability supernovae (Heger et al. 2003), corresponding to 6% of stars over $25_\odot$. The required pair-instability SNe initial mass increases with metallicity, decreasing the fraction of massive stars in the required mass range, until a threshold at which they no longer occur is reached at $Z = Z_\odot/20$, or $[\mathrm{Fe/H}] = -1.3$ (Sabhahit et al. 2023). Only 0.3% of the *sine morte* stellar population lies below that threshold, making the fraction of stars also massive enough to undergo a pair-instability supernova less than $\sim 0.02\%$.

Stars in the Galaxy undergo orbital evolution, migrating and mixing (Sellwood and Binney 2002), and my model of the *sine morte* stellar population takes this into account. By this, I mean the density of the model at a point in space includes stars which died at a previous time in a different location, but if they had not died, would have reached this point in space by the present day. I can do this because the longer-lived companions of these long dead stars are subject to the same dynamical effects as they would have been. I calculate the spatial distribution of black holes by calculating the fraction of stars in my *sine morte* stellar model that form a black hole at each point in space, according to the black hole formation model above. For this, I am assuming that black holes are subject to the same dynamical effects as their progenitor stars would be.

This would be true if black holes continued on the same orbits as their parent stars — however, this may not be the case, due to black hole natal kicks. Black holes commonly experience kicks in velocity in their formation in a core-collapse supernova (Janka 2013), identified mainly in the observed distribution of X-ray binaries (Repetto et al. 2012). The maximum size of these natal kicks is debated; it is generally thought to be $\sim 100\,\mathrm{km\,s^{-1}}$ (Mandel 2016; Andrews and Kalogera 2022). Theses kicks will perturb black holes away from the circular orbits of their progenitor stars (Wielen 1977), meaning their true spatial distribution will vary from that predicted from the *sine morte* distribution. Though a black hole natal kick is qualitatively similar to the ejection of an ISO, in the sense that it changes the orbit of the object away from the orbit of the *sine morte* star it originated from, quantitatively it is of a much higher magnitude (c.f. $\lesssim 10\,\mathrm{km\,s^{-1}}$ for an ISO ejection; Hands et al. 2019; Pfalzner et al. 2021b) therefore cannot be treated identically.

Any component of a natal kick in the plane of the Galaxy will induce an oscillation in the Galactocentric radius R of the black hole, blurring the radial distribution. However, each black hole will oscillate around the Galactocentric radius of their progenitor star. A natal kick is as likely to move a black hole inwards as outward, so I do not account for this effect. The remaining vertical component of a natal kick will induce a vertical oscillation out of the plane of the Galactic disk,

giving the black hole distribution a larger vertical extent than its progenitor stellar population. I can negate this by integrating my model over the vertical direction to estimate the surface density distribution of black holes. However, it does mean that my estimate of the black hole volume density near the Galactic midplane will be an upper limit. The validity of this approach is corroborated by the results of Sweeney et al. (2022) who find Milky Way black holes occupy a disk with a significantly larger scale height but a similar radial distribution compared to the stellar population.

There are additional dynamical effects which I do not account for that may change the spatial distribution of black holes from that calculated from the *sine morte* distribution. The random orbital energy black holes gain from natal kicks will make them less susceptible to radial migration than their origin stellar population (Daniel and Wyse 2015). Also, being generally more massive than stars, black holes are more affected by dynamical friction (Chandrasekhar 1943a,b,c). This effect however will be negligible for stellar black holes, with the in-spiral timescale of a $\sim 10 M_{\odot}$ black hole in the Milky Way disk being $\sim 10^7$ Gyr (Binney and Tremaine 2008), far longer than the age of the Galaxy.

6.3 The Black Hole Gradient

The surface number density distribution of stellar-mass black holes over Galactocentric radius is plotted in the upper panel of Figure 6.1, with the corresponding distribution of living and *sine morte* stellar populations for comparison. All decrease monotonically across the section of the disk modelled. Evaluated at the position of the Sun, taken here to be ($R = 8.1$ kpc; GRAVITY Collaboration et al. 2018)[2], the surface number density of black holes in the Solar neighbourhood is $0.051\,\mathrm{pc}^{-2}$. Integrating over the modelled part of the disk gives 2.5×10^7 black holes in total between 4 kpc and 12 kpc.

[2]As noted in Chapter 2, since this work Leung et al. (2023) was published which includes a comparison of many measurements of R_0, placing its value at (8.2 ± 0.1) kpc

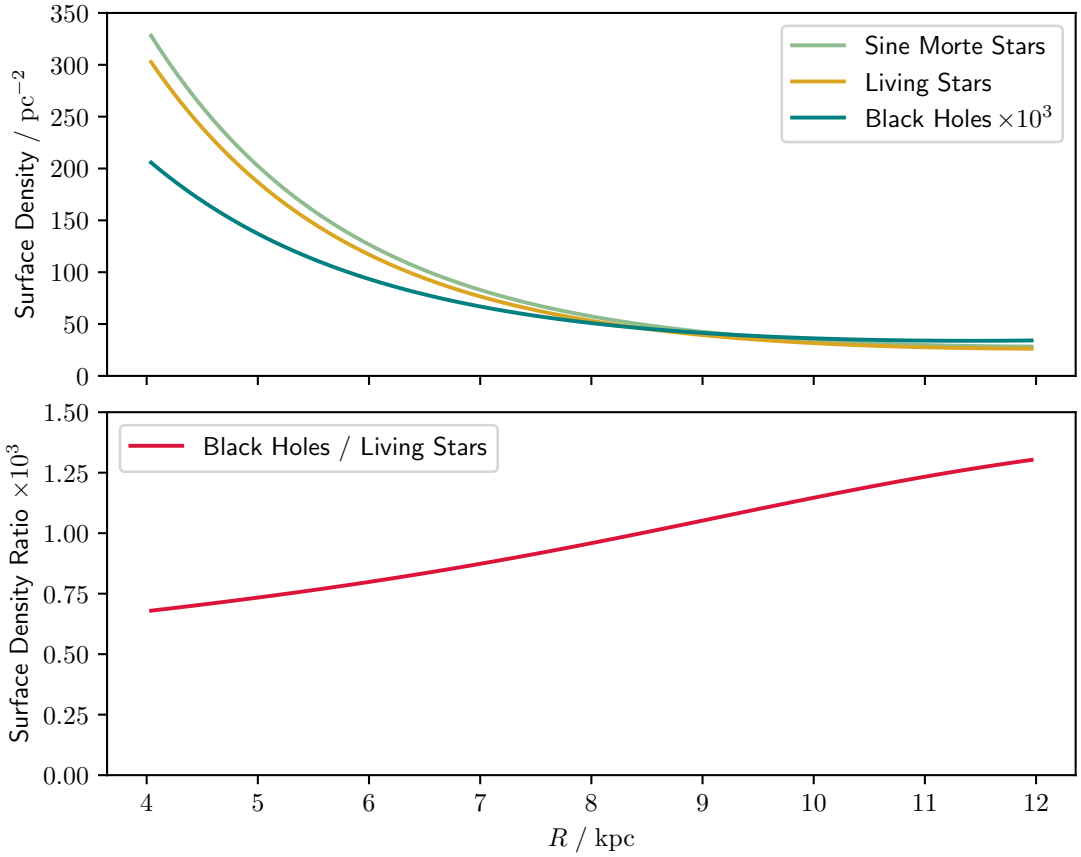

Figure 6.1: Above is plotted the surface number density profiles of the *sine morte* stellar population, currently living stellar population, and the black hole population (multiplied by 10^3) over Galactocentric radius R. Below is plotted the ratio of the surface number densities of black holes and living stars (multiplied by 10^3).

The ratio between the living and *sine morte* stellar surface densities increases only slightly with R, varying from 0.921 to 0.931 over $R = 4 - 12\,\mathrm{kpc}$. This variation is due to the decrease in average age of stars with R.

The ratio of surface densities of black holes to living stars is plotted in the lower panel of Figure 6.1. Though the absolute density of black holes decreases with distance from the Galactic centre, the ratio of black holes to currently living stars increases steadily and significantly over the range modelled, almost doubling from 0.7 black holes per thousand stars at $R = 4\,\mathrm{kpc}$ to 1.3 black holes per thousand stars at $R = 12\,\mathrm{kpc}$. Because the ratio of *sine morte* stars to living stars changes so little, this ratio increase must be a consequence of the Galactic metallicity gradient: stars further from the Galactic centre generally have lower metallicities (Caputo

et al. 2001; Vickers et al. 2021, or my Fig. 2.6). Thus, in the inner disk, a greater proportion of the stars are formed over the metallicity cutoff for black hole formation, reducing the relative abundance of black holes to currently living stars.

Microlensing surveys generally look towards the Galactic centre along the midplane of disk from the radius of Sun $R = 8.1$ to $R = 0$, and are sensitive to the volume density of lenses along this line of sight. As described in §6.2, I expect the distribution of black holes to be more vertically extended than the distribution of stars, due to the vertical components of their natal kicks. This will make the midplane volume density that is calculated here from stars an overestimate.

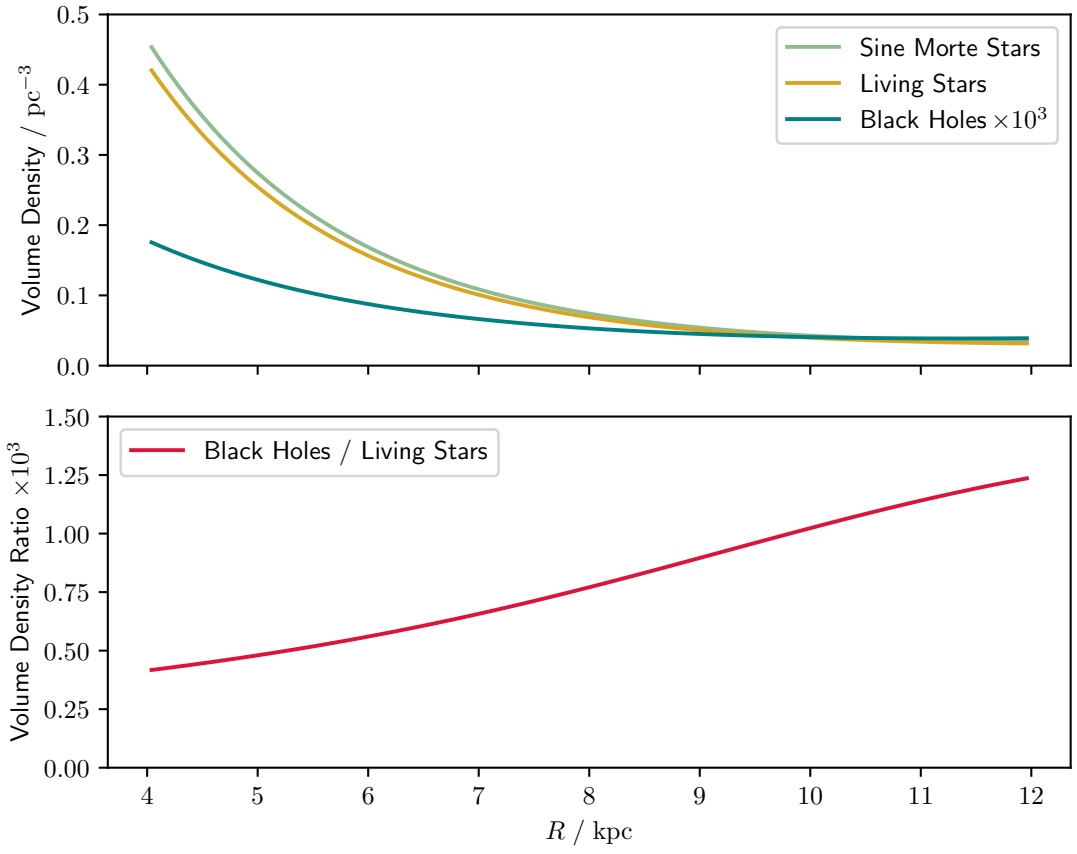

Figure 6.2: Above is plotted the midplane volume number density profiles of the *sine morte* stellar population, currently living stellar population, and the black hole population (multiplied by 10^3) over Galactocentric radius R. Below is plotted the ratio of the midplane volume number densities of black holes and living stars (multiplied by 10^3). Due to the effects of natal kicks on the vertical distribution of black holes I expect the density plotted here to be an overestimate.

Plotted in Figure 6.2 are the midplane density profiles of living stars and black

holes and their ratio. The trends in the surface densities between $R = 4\,\mathrm{kpc}$ to $12\,\mathrm{kpc}$ continue in the midplane volume densities with a strong gradient in the relative abundance of black holes. Even though the midplane volume density ratio here is an upper limit, it is still lower than the surface density ratio plotted in Figure 6.1. This is because the Milky Way disk has a vertical stellar metallicity gradient (Schlesinger et al. 2014) which makes the Galactic midplane high in metallicity, reducing the number of black holes which form.

6.4 Implications for Microlensing Surveys

Gravitational microlensing surveys are the principal method by which isolated stellar black holes can be observed, and *Roman* in particular will have the photometric and astrometric precision required to detect the second-order effects required to characterize lenses as black holes. *Roman* will observe stars within $\sim 2^\circ$ of the Galactic centre (Penny et al. 2019). It will therefore detect black holes along the line of sight between the Sun and the Galactic centre, through the midplane of the inner Galactic disk. Previous studies which predict the number of black hole microlensing events (e.g. Gould 2000; Wiktorowicz et al. 2019; Sajadian and Sahu 2023) make the simplifying assumption that that the Galactic black hole distribution is proportional to the distribution of the currently living stars. This omits the effect of metallicity on black hole formation. Our prediction in §6.3 that the ratio of black holes to living stars increases with distance from the Galactic centre means that there are significantly fewer black holes in the Galactic disk inwards of the Sun. These previous studies therefore over-predict the number of black holes that will be detected. I use my model to estimate corrections to these predictions.

The microlensing optical depth is equal to the fraction of sources at a distance D_S lying within the Einstein ring of a lens (Alcock et al. 1996), equal to

$$\tau = \frac{4\pi G D_S^2}{c^2} \int_0^1 \rho(x) x(1-x)\,\mathrm{d}x \tag{6.1}$$

with x as the fractional distance from the observer to the source population and $\rho(x)$ as the mass density of lensing objects along the line of sight at that distance.

Sajadian and Sahu (2023) calculate the number of black holes that *Roman* will detect as proportional to the fraction of the total microlensing optical depth caused by black holes, $\mathcal{F}_1$, given by

$$\mathcal{F}_1 = \frac{\tau_{\rm BH}}{\tau_{\rm total}} = \frac{\int \rho_{\rm BH}(x) x(1-x)\,{\rm d}x}{\int \rho_{\rm total}(x) x(1-x)\,{\rm d}x} = \frac{\langle M_{\rm BH}\rangle \int n_{\rm BH}(x) x(1-x)\,{\rm d}x}{\langle M_{\rm total}\rangle \int n_{\rm total}(x) x(1-x)\,{\rm d}x}\,. \tag{6.2}$$

This formula differs from Sajadian and Sahu (2023) as they assume no black hole gradient, meaning in their formula the dependence on x cancels out. Ordinarily this would require a model of the stellar and black hole populations extending into the Galactic centre where the Galactic bulge provides a high density of sources. However Sajadian and Sahu (2023) find that only black holes closer to the observer than half the distance to the source will be well characterised. Assuming the majority of sources lie in the Galactic bulge at with $R \simeq 0$, well-characterised black holes will only be found at $R \gtrsim 4\,{\rm kpc}$, within the range of my model. I use my model to calculate a value of $\mathcal{F}_1$ with this range which includes the gradient in relative black hole abundance, then predict the number of black holes *Roman* will detect by scaling the number predicted by Sajadian and Sahu (2023) by the ratio of my value of $\mathcal{F}_1$ to theirs.

Since *Roman* will observe within 2° of the Galactic centre (Penny et al. 2019) and the Sun is only $z = 21\,{\rm pc}$ above the midplane (Bennett and Bovy 2019), the line of sight along which we calculate $\mathcal{F}_1$ lies along the midplane of the Galaxy between $R = 4\,{\rm kpc}$ to $R = 8.1\,{\rm kpc}$. $n_{\rm BH}(x)$ is the volume number density of black holes, which I take to be the upper limit in the density profile plotted in Figure 6.2 (as per discussion in §6.2 and §6.3). $\langle M_{\rm BH}\rangle$ is the average mass, which I take to be $20 M_\odot$ based on Belczynski et al. (2004) and Wiktorowicz et al. (2019). Like Sajadian and Sahu (2023), I assume that the overall optical depth is dominated by stellar objects and brown dwarfs. I take $n_{\rm total}(x)$ to be the sum of the midplane living stellar density profile plotted in Fig. 6.2, and a profile of brown dwarfs, which I calculate from the *sine morte* profile, assuming the brown dwarf IMF $\propto M^{-0.7}$ (Mužić et al. 2015). These living stars $n_{\rm total}(x)$ are plotted in Figure 6.2. Similarly, by integrating the combination of the Mužić brown dwarf IMF and the Kroupa universal stellar IMF, I

find an average lens mass of $\langle M_{\rm total} \rangle = 0.40 M_\odot$. This gives my value of $\mathcal{F}_1 = 0.013$, somewhat less than that of $\mathcal{F}_1 = 0.019$ calculated by Sajadian and Sahu (2023).

I expect the black hole midplane density $n_{\rm BH}(x)$ that I have used to be an upper limit, due to the vertical component of black hole natal kicks reducing their midplane density. Therefore I expect my scaled value of $\mathcal{F}_1$ to be an upper limit as well. Since Sajadian and Sahu (2023) predict *Roman* will characterize 17–24 black holes to within 10% fractional error on physical parameters, I predict that it will instead characterize fewer than 16 to this level. This is not a very significant decrease, given the large uncertainties in the fraction of stars formed which become black holes at the end of their lives (Rose et al. 2022), however as discussed above this estimate is a upper limit due to my estimate of the midplane black hole density not accounting for black hole natal kicks.

6.5 Conclusion

I predict the distribution of black holes in the Milky Way using the stellar population model of Chapter 2. Being a model of the *sine morte* stellar distribution, it contains all stars ever born, not just those currently living. I combine this with a metallicity-dependent black hole formation model based on Heger et al. (2003).

To partially negate the effect of black hole natal kicks, I calculate the surface density of black holes in the Galactic disk at each galactocentric radius R, and find that the surface number density of black holes decreases with distance from the Galactic centre, similar to the stellar distribution, however at a slower rate. This results in a steep gradient in the ratio of stars to black holes, doubling from 0.7 black holes per thousand stars at $R = 4\,\mathrm{kpc}$ to 1.3 black holes per thousand stars at $R = 12\,\mathrm{kpc}$. This is caused by the Milky Way metallicity gradient, the decreasing metallicity of stars with distance from the Galactic centre, and the prediction that black holes do not form from stars at high metallicity.

This Galactic black hole gradient has implications for microlensing surveys which search for black holes between the Sun and the Galactic centre. Previous predictions of microlensing detection rates assume the black hole distribution to

be proportional to the living stellar distribution with no accounting for metallicity, so over-predict the number of black holes they will detect. I use my model of the black hole distribution to calculate a correction to the prediction of Sajadian and Sahu (2023), and estimate that *Roman* will detect and characterize at most 16 black holes to within 10% fractional errors, slightly less than the number predicted by Sajadian and Sahu (2023). This effect is small compared to the uncertainties in the fraction of stars which become black holes which dominate this estimate. However, my prediction is a strict overestimate as it does not include the effect of black hole natal kicks which will remove them from the midplane.

This work demonstrates the application of the concept of the *sine morte* population to other fields. Other areas of astrophysics for which it would be useful may include neutron stars, which are also stellar remnants, and significantly easier to observe.

Let us think the unthinkable, let us do the undoable, let us prepare to grapple with the ineffable itself, and see if we may not eff it after all.

— Douglas Adams, *Dirk Gently's Holistic Detective Agency*

7 Conclusions

7.1 3I

The Vera C. Rubin Observatory's Legacy Survey of Space and Time will begin this year. Following the predictions of Chapter 4 and Dorsey et al. (2025), by the time of its first data release 12–14 months after survey start (Guy et al. 2023) we are likely to have discovered our third interstellar object: 3I. Increasing our sample size by 50%, even this one discovery will represent the opportunity to vastly increase our knowledge of the ISO population. With the work of Chapter 4 and Dorsey et al. (2025), we will be able to significantly improve our constraints on the number density of ISOs, which so far is just estimated from the one discovery of 1I in Pan-STARRS. This will answer questions first posed in the 1980s, discussed in §1.1.2: how many ISOs are produced by each planetary system? Is the Solar System unusual in the number of objects it must have ejected to populate the Öpik–Oort cloud? Additionally, with a measured absolute magnitude H we will be able to begin to constrain the size distribution of ISOs in the Solar neighbourhood. This too carries information about planetesimal formation across the Milky Way, as a steep size distribution with many small objects implies collisional evolution or fragmentation processes (§4.4).

Given the work of Chapter 2, the velocity of 3I will also inform us of its origins: even if its composition cannot be calculated with a measured spectrum, the velocity with which it enters the Solar System can be used to make inferences about its age and the abundances of the planetary system it formed around (§3.4.2). I predict that, like 1I and 2I, the pre-encounter velocity of 3I will lie within a moving group. If it does not, this could be an indication either that it is a very old object, or that there are dynamical effects which I have not taken into account in my model, for example the formation of tidal streams (Forbes et al. 2024).

If 3I displays cometary activity like 2I/Borisov, with spectra its composition can be estimated. Its composition can be compared to that expected from the abundances of the stars and planetary systems it shares a velocity with, and its formation location within its parent protoplanetary disk can be conjectured (Seligman et al. 2022). As the sample of measured ISO compositions grows, this can be compared to my predictions in Chapter 2 in order to draw inferences about planetesimal formation in a range of environments across the Milky Way.

If 3I does not display cometary activity, instead being more similar to 1I, this presents an equally interesting opportunity to potentially resolve the mysteries ʻOumuamua left behind when it faded beyond the magnitude limit of observation. We now have JWST (Gardner et al. 2006), significantly more sensitive than *Spitzer* (cf. Fig. 4 of Arendt et al. 2023), which will be able to either detect or place strong upper limits on any outgassing that may be occurring (Meech et al. 2023; Cordiner et al. 2024). Better characterisation along with the better chance the LSST gives us of discovering 1I-like ISOs before they pass perihelion will enable us to rule out many of the hypotheses of its origin discussed in §1.2.3.

A third possibility, discussed in §4.4, is that 3I is similar to neither 1I nor 2I. The distribution of expected absolute magnitudes H for the LSST ISO sample, plotted in Fig. 4.4, shows that for a sufficiently flat absolute magnitude distribution ($q_s \lesssim 2.8$) the LSST is likely to find ~ 1 large ISOs with $H \lesssim 8$. With typical Solar System albedos this corresponds to the size of large trans-Neptunian objects, $\gtrsim 100\,\mathrm{km}$ in diameter. Objects of this size will have a remarkably different formation pathway

to both 1I and 2I, and similar objects in the Solar System represent one of the most primitive populations of planetesimals. Alternatively, as with the discovery of 1I, we may be entirely surprised again.

7.2 The LSST ISO Sample

1I/'Oumuamua may have been unlike anything seen before in our Solar System, but it is highly unlikely that the first ISO to be discovered happens to be unique among ISOs. Thus as the LSST sample grows at a rate of ~ 1 per year (Chapter 4) we will be able to answer the question of how unusual 1I really was. As our discovered sample populates the parameter space of possible ISOs, it may turn out that 1I was simply drawn from the edge of a distribution of asteroidal objects not too different from those in our Solar System. Alternatively, 1I may indeed have been typical of an atypical population, objects not found in the Solar System such as those discussed in §1.2.3: tidal disruption fragments, fractal dust aggregates, or chunks of N_2 or H_2 ice. If so, the relative abundance of each type of ISO relative to the more-traditional cometary ISOs such as 2I/Borisov will contain information about how planetary systems form and eject planetesimals. Different compositions of ISOs will additionally inform us of the relative number of ISOs originating from each part of the protoplanetary disk, as using methods such as that of Seligman et al. (2022) cometary ISOs with measured production rates can be traced back to annuli in their protoplanetary disks between pairs of icelines.

Excitingly, Forbes et al. (2024) estimate that the LSST ISO sample has a chance of containing a pair of ISO 'cousins', sourced from the same stellar birth cluster. This would be indicated by the two having a similar velocity, and a statistical measure of how likely two given ISOs in the sample are to be cousins could be calculated using the predicted velocity distribution of Chapter 3, combined with the selection effects estimated with the work of Chapter 4 in Dorsey et al. (2025). With colour and composition measurements, a pair of ISO cousins would be a fascinating study of the diversity of objects a different planetary system can form. Of further interest is the unlikely but feasible possibility of a binary ISO as discussed

in Chapter 5. The tenuous nature of the binding between the two components would place strong constraints on the potential mechanism by which they were ejected from their home system, and the tidal forces they had experienced in their wandering through the Galaxy.

As the population of ISOs is better characterised, investigations into the interactions between the Galactic ISO population and other other objects will be of interest. Building on the work of Chapter 5 and Pham et al. (2024), a better constrained size distribution may allow further testing of our hypothesis that ISO–NS collisions may be the cause of some FRBs, as the size of ISOs is related to both the duration and luminosity of FRBs. Further study of FRBs, including well-characterised surveys with estimated selection effects, would help this effort too.

ISOs will also impact white dwarfs in the Galaxy, contributing to the pollution that is observed on their surfaces (Farihi 2016). The fraction of this pollution that is due to ISOs as opposed to planetary material that originated around the white dwarf is currently unclear, but could be constrained. Finally, the detection or non-detection of massive ISOs in pulsar timing arrays (Jennings et al. 2020) could constrain the size distribution of ISOs at larger sizes, and due to the distributed nature of the pulsar sources this could constrain the number density profile of ISOs across the Galaxy.

To complete one's DPhil at the dawn of a new era in science is a privilege. The LSST is expected to revolutionise multiple disciplines of astronomy, and by interacting with astrophysics at all scales the ISOs that it will find have the potential to contribute to the study of as many fields as we have the imagination to apply them to.

I'm looking forward to taking a break after I finish my minor corrections tomorrow.

— Matthew J. Hopkins (Monday, 30th June 2025)

8 Postscript

8.1 3I/ATLAS

As my final minor correction I add this note for posterity on the discovery of the third interstellar object, just five days after my *viva voce* examination, in the early hours of Tuesday, 1st July 2025.

Observationally 3I/ATLAS (MPEC 2025-N12) is cometary (Seligman et al. 2025), with a largely-featureless spectrum and colour similar to D-type asteroids, some TNOs and 1I/'Oumuamua but redder than most Solar System comets (Opitom et al. 2025; Bolin et al. 2025; Belyakov et al. 2025; Kareta et al. 2025; de la Fuente Marcos et al. 2025; Yang et al. 2025). 3I was serendipitously imaged by the Vera C. Rubin Observatory during commissioning 10 days before its discovery, providing the earliest high-resolution detection of cometary activity (Chandler et al. 2025).

Using the Ōtautahi–Oxford model developed in this thesis, my collaborators and I predict from its velocity that 3I/ATLAS is water-rich and old, with a 68% confidence interval on its age of 7.6–14 Gyr (Hopkins et al. 2025b).

MJH

23rd July 2025

Appendices

A

Gaia Archive Queries

Quoted below are the ADQL queries made to the Gaia archive to acquire the data for Chapter 3.

For data:

```
SELECT s.parallax AS plx, s.parallax_over_error,
s.ra AS ra, s.dec AS dec, s.pmra AS pmra, s.pmdec AS pmdec,
s.radial_velocity AS rv, s.radial_velocity_error,
ap.mh_gspspec AS mh, apsupp.age_flame_spec,
apsupp.flags_flame_spec FROM gaiadr3.gaia_source AS s
JOIN gaiadr3.astrophysical_parameters AS ap USING (source_id)
JOIN gaiadr3.astrophysical_parameters_supp as apsupp
USING (source_id) WHERE s.parallax>5 AND s.parallax_over_error>10
AND s.radial_velocity IS NOT NULL AND s.radial_velocity_error<5
AND ap.mh_gspspec IS NOT NULL AND apsupp.age_flame_spec IS NOT NULL
AND apsupp.flags_flame_spec='0'
```

For selection function k:

```
SELECT GAIA_HEALPIX_INDEX(2,source_id) AS healpix_,
FLOOR((gs.phot_g_mean_mag - 3)/1.0) AS phot_g_mean_mag_,
FLOOR((gs.g_rp - -1.0)/0.2) AS g_rp_, COUNT(*) AS k
FROM gaiadr3.gaia_source AS gs
JOIN gaiadr3.astrophysical_parameters AS ap USING (source_id)
JOIN gaiadr3.astrophysical_parameters_supp AS apsupp
USING (source_id) WHERE gs.parallax_over_error>10
AND gs.radial_velocity_error<5 AND gs.radial_velocity IS NOT NULL
AND ap.mh_gspspec IS NOT NULL AND apsupp.age_flame_spec IS NOT NULL
AND apsupp.flags_flame_spec='0' AND gs.phot_g_mean_mag > 3
AND gs.phot_g_mean_mag < 17 AND gs.g_rp > -1.0 AND gs.g_rp < 2.0
GROUP BY healpix_, phot_g_mean_mag_, g_rp_
```

For selection function n:

```
SELECT sq.healpix_, sq.phot_g_mean_mag_, sq.g_rp_, COUNT(*) AS n
FROM ( SELECT GAIA_HEALPIX_INDEX(2,source_id) AS healpix_,
FLOOR((gs.phot_g_mean_mag - 3)/1.0) AS phot_g_mean_mag_,
FLOOR((gs.g_rp - -1.0)/0.2) AS g_rp_ FROM gaiadr3.gaia_source AS gs
WHERE gs.phot_g_mean_mag > 3 AND gs.phot_g_mean_mag < 17
AND gs.g_rp > -1.0 AND gs.g_rp < 2.0
) AS sq GROUP BY sq.healpix_, sq.phot_g_mean_mag_, sq.g_rp_
```

"Your talk," I said, "is surely the handiwork of wisdom because not one word of it do I understand."

— Flann O'Brien, *The Third Policeman* (1967)

References

'Oumuamua ISSI Team et al. (2019). *Nature Astronomy* 3, pp. 594–602.

Abbott, B. P. et al. (2017). Phys. Rev. Lett. 119.16, 161101, p. 161101.

Abolfathi, B. et al. (2018). ApJS 235.2, 42, p. 42.

Adams, D. (1980). *The Resturant at the End of the Universe*. Pan Books.

Akaike, H. (1974). *IEEE Transactions on Automatic Control* 19, pp. 716–723.

Albrow, L., Bannister, M., and Forbes, J. (2024). In: *AAS/Division for Extreme Solar Systems Abstracts*. Vol. 56. AAS/Division for Extreme Solar Systems Abstracts, 615.17, p. 615.17.

Alcock, C. et al. (1993). In: *Sky Surveys. Protostars to Protogalaxies*. Ed. by B. T. Soifer. Vol. 43. Astronomical Society of the Pacific Conference Series, p. 291.

Alcock, C. et al. (1996). ApJ 461, p. 84.

Almeida-Fernandes, F. and Rocha-Pinto, H. J. (2018a). MNRAS 480.4, pp. 4903–4911.

Almeida-Fernandes, F. and Rocha-Pinto, H. J. (2018b). MNRAS 476.1, pp. 184–197.

Andama, G., Mah, J., and Bitsch, B. (2024). A&A 683, A118, A118.

Andrews, J. J. and Kalogera, V. (2022). ApJ 930.2, 159, p. 159.

Andrews, S. M. et al. (2013). ApJ 771.2, 129, p. 129.

Anguiano, B. et al. (2020). AJ 160.1, 43, p. 43.

Angus, R. et al. (2015). MNRAS 450.2, pp. 1787–1798.

Ansdell, M. et al. (2018). ApJ 859.1, 21, p. 21.

Antoja, T. et al. (2008). A&A 490.1, pp. 135–150.

Antoja, T. et al. (2018). Nature 561.7723, pp. 360–362.

Arendt, R. G. et al. (2023). ApJ 959.2, 95, p. 95.

Armitage, P. J. (2024). *arXiv e-prints*, arXiv:2412.11064, arXiv:2412.11064.

Asphaug, E. and Benz, W. (1994). Nature 370.6485, pp. 120–124.

Asphaug, E. and Benz, W. (1996). Icarus 121.2, pp. 225–248.

Astropy Collaboration et al. (2013). A&A 558, A33, A33.

Astropy Collaboration et al. (2018). AJ 156.3, 123, p. 123.

Astropy Collaboration et al. (2022). ApJ 935.2, 167, p. 167.

Aubourg, E. et al. (1993). Nature 365.6447, pp. 623–625.

Baade, W. (1946). PASP 58.343, pp. 249–252.

Baba, J. (2015). MNRAS 454.3, pp. 2954–2964.

Bagchi, M. (2017). ApJ 838.2, L16, p. L16.

Bagnulo, S. et al. (2021). *Nature Communications* 12, 1797, p. 1797.

Bailer-Jones, C. A. L. et al. (2018). AJ 156.5, 205, p. 205.

Bailer-Jones, C. A. L. et al. (2020). A&A 634, A14, A14.

Bannister, M. T. et al. (2017). ApJ 851.2, L38, p. L38.

Bannister, M. T. et al. (2020). *arXiv e-prints*, arXiv:2001.11605, arXiv:2001.11605.

Barker, P. (2002). *Perspectives on Science* 10.2, pp. 208–227.

Bashi, D. and Zucker, S. (2019). AJ 158.2, 61, p. 61.

Bayes, M. and Price, M. (1763). *Philosophical Transactions of the Royal Society of London Series I* 53, pp. 370–418.

Belbruno, E. et al. (2012). *Astrobiology* 12.8, pp. 754–774.

Belczynski, K., Sadowski, A., and Rasio, F. A. (2004). ApJ 611.2, pp. 1068–1079.

Belton, M. J. S. et al. (2018). ApJ 856.2, L21, p. L21.

Belyakov, M. et al. (2025). *arXiv e-prints*, arXiv:2507.11720, arXiv:2507.11720.

Bennett, M. and Bovy, J. (2019). MNRAS 482.1, pp. 1417–1425.

Bensby, T., Feltzing, S., and Lundström, I. (2003). A&A 410, pp. 527–551.

Bensby, T. et al. (2007). ApJ 655.2, pp. L89–L92.

Bergner, J. B. and Seligman, D. Z. (2023a). Nature 615.7953, pp. 610–613.

Bergner, J. B. and Seligman, D. Z. (2023b). Nature 623.7989, E16–E17.

Bhandari, S. et al. (2020). ApJ 895.2, L37, p. L37.

Bialy, S. and Loeb, A. (2018). ApJ 868.1, L1, p. L1.

Bianco, F. B. et al. (2022). *Updated estimates of the Rubin system throughput and expected LSST image depth*.

Binney, J. and Merrifield, M. (1998). *Galactic Astronomy*.

Binney, J. and Tremaine, S. (2008). *Galactic Dynamics: Second Edition*.

Bitsch, B. and Battistini, C. (2020). A&A 633, A10, A10.

Blanton, M. R. et al. (2003). ApJ 592.2, pp. 819–838.

Bochenek, C. D. et al. (2020). Nature 587.7832, pp. 59–62.

Bodewits, D. et al. (2020). *Nature Astronomy* 4, pp. 867–871.

Bolin, B. T. et al. (2018). ApJ 852.1, L2, p. L2.

Bolin, B. T. et al. (2020). AJ 160.1, 26, p. 26.

Bolin, B. T. et al. (2025). *arXiv e-prints*, arXiv:2507.05252, arXiv:2507.05252.

Bonaca, A. and Price-Whelan, A. M. (2025). New A Rev. 100, 101713, p. 101713.

Bond, I. A. et al. (2001). MNRAS 327.3, pp. 868–880.

Borucki, W. J. et al. (2010). *Science* 327.5968, p. 977.

Bottke, W. F. et al. (2005). Icarus 175.1, pp. 111–140.

Bovy, J. (2016). ApJ 817.1, 49, p. 49.

Bovy, J. (2017). MNRAS 470.2, pp. 1360–1387.

Bovy, J. et al. (2012a). ApJ 759.2, 131, p. 131.

Bovy, J. et al. (2012b). ApJ 753.2, 148, p. 148.

Bovy, J. et al. (2016a). ApJ 818.2, 130, p. 130.

Bovy, J. et al. (2016b). ApJ 823.1, 30, p. 30.

Box, G. E. P. (1976). *Journal of the American Statistical Association* 71.356, pp. 791–799.

Brasser, R., Duncan, M. J., and Levison, H. F. (2006). Icarus 184.1, pp. 59–82.

Brasser, R., Higuchi, A., and Kaib, N. (2010). A&A 516, A72, A72.

Bressan, A. et al. (2012). MNRAS 427.1, pp. 127–145.

Brewer, J. M. et al. (2018). ApJ 867.1, L3, p. L3.

Brook, P. R. et al. (2014). ApJ 780.2, L31, p. L31.

Brott, I. et al. (2011). A&A 530, A115, A115.

Brown, P. G. and Borovička, J. (2023). ApJ 953.2, 167, p. 167.

Brownlee, D. E. et al. (2003). *Journal of Geophysical Research (Planets)* 108.E10, 8111, p. 8111.

Buder, S. et al. (2018). MNRAS 478.4, pp. 4513–4552.

Caffau, E. et al. (2011). Sol. Phys. 268.2, pp. 255–269.

Cannon, A. J. and Pickering, E. C. (1901). *Annals of Harvard College Observatory* 28, 129–P.6.

Cantat-Gaudin, T. et al. (2023). A&A 669, A55, A55.

Cao, D., Plavchan, P., and Summers, M. (2024). ApJ 971.2, 160, p. 160.

Caputo, F. et al. (2001). A&A 372, pp. 544–550.

Castro-Ginard, A. et al. (2023). A&A 677, A37, A37.

Cazzoletti, P. et al. (2019). A&A 626, A11, A11.

Chabrier, G. (2003). PASP 115.809, pp. 763–795.

Chambers, K. C. et al. (2016). *arXiv e-prints*, arXiv:1612.05560, arXiv:1612.05560.

Chandler, C. O. et al. (2025). *arXiv e-prints*, arXiv:2507.13409, arXiv:2507.13409.

Chandrasekhar, S. (1943a). ApJ 97, p. 255.

Chandrasekhar, S. (1943b). ApJ 97, p. 263.

Chandrasekhar, S. (1943c). ApJ 98, p. 54.

Chatterjee, S. et al. (2005). ApJ 630.1, pp. L61–L64.

Chen, J. H. et al. (2024). ApJ 973.2, L54, p. L54.

Cheng, J. Y. et al. (2012). ApJ 746.2, 149, p. 149.

Chesley, S. R. et al. (2016). In: *Asteroids: New Observations, New Models*. Ed. by S. R. Chesley et al. Vol. 318. IAU Symposium, pp. 250–258.

Chiappini, C., Matteucci, F., and Gratton, R. (1997). ApJ 477.2, pp. 765–780.

Childs, A. C. and Martin, R. G. (2022). ApJ 935.2, L31, p. L31.

CHIME Collaboration et al. (2022). ApJS 261.2, 29, p. 29.

CHIME/FRB Collaboration et al. (2019). ApJ 885.1, L24, p. L24.

CHIME/FRB Collaboration et al. (2020). Nature 587.7832, pp. 54–58.

CHIME/FRB Collaboration et al. (2021). ApJS 257.2, 59, p. 59.

Chruslinska, M. et al. (2018). MNRAS 474.3, pp. 2937–2958.

Cochran, A. L., Nelson, T., and McKay, A. J. (2020). PSJ 1.3, 71, p. 71.

Colgate, S. A. and Petschek, A. G. (1981). ApJ 248, pp. 771–782.

Cook, N. V. et al. (2016). ApJ 825.1, 51, p. 51.

Cordiner, M. A. et al. (2020). *Nature Astronomy* 4, pp. 861–866.

Cordiner, M. A. et al. (2024). *Composition of an Interstellar Object - Unique Insights into Protoplanetary Disk Midplane Chemistry*. JWST Proposal. Cycle 3, ID. #5094.

Cowie, C. (2021). *Nature Astronomy* 5, pp. 526–527.

Creevey, O. L. and Lebreton, Y. (2022). "Masses and ages from FLAME in DR3". Technical Note.

Creevey, O. L. et al. (2023). A&A 674, A26, A26.

Cremonese, G. et al. (2020). ApJ 893.1, L12, p. L12.

Cropper, M. et al. (2018). A&A 616, A5, A5.

Ćuk, M. (2018). ApJ 852.1, L15, p. L15.

Dai, Z. G. (2020). ApJ 897.2, L40, p. L40.

Dai, Z. G. et al. (2016). ApJ 829.1, 27, p. 27.

Daniel, K. J. and Wyse, R. F. G. (2015). MNRAS 447.4, pp. 3576–3592.

Davis, D. R. et al. (1985). Icarus 62.1, pp. 30–53.

de la Fuente Marcos, R. et al. (2025). *arXiv e-prints*, arXiv:2507.12922, arXiv:2507.12922.

de León, J. et al. (2020). MNRAS 495.2, pp. 2053–2062.

de León, J. et al. (2019). *Research Notes of the American Astronomical Society* 3.9, 131, p. 131.

De Silva, G. M. et al. (2015). MNRAS 449.3, pp. 2604–2617.

de Vaucouleurs, G. (1964). In: *The Galaxy and the Magellanic Clouds*. Ed. by F. J. Kerr. Vol. 20. IAU Symposium, p. 195.

Dehnen, W. (1998). AJ 115.6, pp. 2384–2396.

Dehnen, W., Hands, T. O., and Schönrich, R. (2022). MNRAS 512.3, pp. 4078–4085.

Deienno, R. et al. (2024). PSJ 5.5, 110, p. 110.

Delhaye, J. (1965). "Solar Motion and Velocity Distribution of Common Stars". In: *Galactic structure. Edited by Adriaan Blaauw and Maarten Schmidt. Published by the University of Chicago Press*. Ed. by A. Blaauw and M. Schmidt, p. 61.

Deng, W. and Zhang, B. (2014). ApJ 783.2, L35, p. L35.

Deo, S. N. and Kushvah, B. S. (2017). *Astronomy and Computing* 20, pp. 97–104.

Desch, S. J. and Jackson, A. P. (2021). *Journal of Geophysical Research (Planets)* 126.5, e06807, e06807.

Desch, S. (2024). *arXiv e-prints*, arXiv:2403.05161, arXiv:2403.05161.

Desch, S. and Jackson, A. (2023). *arXiv e-prints*, arXiv:2311.07699, arXiv:2311.07699.

Desch, S. J. and Jackson, A. P. (2022). *Astrobiology* 22.12, pp. 1400–1413.

Do, A., Tucker, M. A., and Tonry, J. (2018). ApJ 855.1, L10, p. L10.

Dominik, M. et al. (2013). ApJ 779.1, 72, p. 72.

Domokos, G. et al. (2017). *Research Notes of the American Astronomical Society* 1.1, 50, p. 50.

Dones, L. et al. (2004). In: *Star Formation in the Interstellar Medium: In Honor of David Hollenbach*. Ed. by D. Johnstone et al. Vol. 323. Astronomical Society of the Pacific Conference Series, p. 371.

Dorsey, R. C. et al. (2025). *arXiv e-prints*, arXiv:2502.16741, arXiv:2502.16741.

Drahus, M. et al. (2018). *Nature Astronomy* 2, pp. 407–412.

Dressing, C. D. and Charbonneau, D. (2015). ApJ 807.1, 45, p. 45.

Drimmel, R., Cabrera-Lavers, A., and López-Corredoira, M. (2003). A&A 409, pp. 205–215.

Dybczyński, P. A. and Królikowska, M. (2018). A&A 610, L11, p. L11.

Dybczyński, P. A., Królikowska, M., and Wysoczańska, R. (2019). *arXiv e-prints*, arXiv:1909.10952, arXiv:1909.10952.

Eddington, A. S. (1906). MNRAS 67, pp. 34–63.

Edvardsson, B. et al. (1993). A&A 275, p. 101.

Ekers, R. D. et al. (2002). *SETI 2020 : a roadmap for the search for extraterrestrial intelligence / produced for the SETI Institute by the SETI Science & Technology Working Group.*

Elbert, O. D., Bullock, J. S., and Kaplinghat, M. (2018). MNRAS 473.1, pp. 1186–1194.

Engelhardt, T. et al. (2017). AJ 153.3, 133, p. 133.

Eubanks, T. M. et al. (2021). *arXiv e-prints*, arXiv:2103.03289, arXiv:2103.03289.

Fabry, L. (1893). *Etude sur la probabilite des cometes hyperboliques et l'origine des cometes ...*

Famaey, B., Siebert, A., and Jorissen, A. (2008). A&A 483.2, pp. 453–459.

Farihi, J. (2016). New A Rev. 71, pp. 9–34.

Farnocchia, D. et al. (2023). PSJ 4.2, 29, p. 29.

Fedele, D. and Favre, C. (2020). A&A 638, A110, A110.

Fender, R. P., Maccarone, T. J., and Heywood, I. (2013). MNRAS 430.3, pp. 1538–1547.

Feng, F. and Jones, H. R. A. (2018). ApJ 852.2, L27, p. L27.

Ferlet, R., Hobbs, L. M., and Vidal-Madjar, A. (1987). A&A 185, pp. 267–270.

Fernandez, J. A. (1978). Icarus 34.1, pp. 173–181.

Fernando, B. et al. (2024). *Geophysical Journal International*.

Filacchione, G. et al. (2022). *arXiv e-prints*, arXiv:2210.02741, arXiv:2210.02741.

Fischer, D. A. and Valenti, J. (2005). ApJ 622.2, pp. 1102–1117.

Fitzmaurice, E., Martin, D. V., and Fabrycky, D. C. (2022). MNRAS 512.4, pp. 5023–5036.

Fitzsimmons, A. et al. (2018). *Nature Astronomy* 2, pp. 133–137.

Fitzsimmons, A. et al. (2019). ApJ 885.1, L9, p. L9.

Fitzsimmons, A. et al. (2023). *arXiv e-prints*, arXiv:2303.17980, arXiv:2303.17980.

Flekkøy, E. G., Luu, J., and Toussaint, R. (2019). ApJ 885.2, L41, p. L41.

Flekkøy, E. G. and Toussaint, R. (2023). MNRAS 523.1, pp. L9–L14.

Forbes, J. C. and Loeb, A. (2019). ApJ 875.2, L23, p. L23.

Forbes, J. C. et al. (2024). *arXiv e-prints*, arXiv:2411.14577, arXiv:2411.14577.

Fouesneau, M. et al. (2023). A&A 674, A28, A28.

Fraley, G. S. (1968). Ap&SS 2.1, pp. 96–114.

Frankel, N. et al. (2019). ApJ 884.2, 99, p. 99.

Frankel, N. et al. (2020). ApJ 896.1, 15, p. 15.

Fraser, W. C. et al. (2017). *Nature Astronomy* 1, 0088, p. 0088.

Fraser, W. C. et al. (2018). *Nature Astronomy* 2, pp. 383–386.

Fujiwara, A. et al. (2006). *Science* 312.5778, pp. 1330–1334.

Gaia Collaboration et al. (2016). A&A 595, A1, A1.

Gaia Collaboration et al. (2018). A&A 616, A1, A1.

Gaia Collaboration et al. (2023). A&A 674, A1, A1.

Gaidos, E. (2018). MNRAS 477.4, pp. 5692–5699.

Gallardo, P. A. (2023). *Research Notes of the American Astronomical Society* 7.10, 220, p. 220.

Gallardo, P. A. (2024). *Research Notes of the American Astronomical Society* 8.3, 88, p. 88.

García Pérez, A. E. et al. (2016). AJ 151.6, 144, p. 144.

Gardner, J. P. et al. (2006). Space Sci. Rev. 123.4, pp. 485–606.

Gauss, K. F. (1809). *Theoria motvs corporvm coelestivm in sectionibvs conicis solem ambientivm.*

Geng, J. J. and Huang, Y. F. (2015). ApJ 809.1, 24, p. 24.

Gentile Fusillo, N. P. et al. (2021). MNRAS 508.3, pp. 3877–3896.

Gilmore, G. and Reid, N. (1983). MNRAS 202, pp. 1025–1047.

Ginsburg, I., Lingam, M., and Loeb, A. (2018). ApJ 868.1, L12, p. L12.

Gladman, B. J. et al. (2009). Icarus 202.1, pp. 104–118.

Gomes, R. et al. (2005). Nature 435.7041, pp. 466–469.

Gordon, A. C. et al. (2023). ApJ 954.1, 80, p. 80.

Górski, K. M. et al. (2005). ApJ 622.2, pp. 759–771.

Gould, A. (1992). ApJ 392, p. 442.

Gould, A. (2000). ApJ 535.2, pp. 928–931.

Granvik, M. et al. (2016). Nature 530.7590, pp. 303–306.

Gratton, R. et al. (1996). In: *Formation of the Galactic Halo...Inside and Out*. Ed. by H. L. Morrison and A. Sarajedini. Vol. 92. Astronomical Society of the Pacific Conference Series, p. 307.

GRAVITY Collaboration et al. (2018). A&A 615, L15, p. L15.

Green, G. M. et al. (2019). ApJ 887.1, 93, p. 93.

Greenberg, J. M., Mizutani, H., and Yamamoto, T. (1995). A&A 295, pp. L35–L38.

Gregg, C. R. and Wiegert, P. A. (2025). PSJ 6.3, 56, p. 56.

Grenon, M. (1972). In: *IAU Colloq. 17: Age des Etoiles*. Ed. by G. Cayrel de Strobel and A. M. Delplace, p. 55.

Grishin, E., Perets, H. B., and Avni, Y. (2019). MNRAS 487.3, pp. 3324–3332.

Guerra-Alvarado, O. M. et al. (2025). A&A 696, A232, A232.

Guilbert-Lepoutre, A. et al. (2015). Space Sci. Rev. 197.1-4, pp. 271–296.

Gustafsson, B. et al. (2016). A&A 593, A85, A85.

Guy, L. P. et al. (2023). *Rubin Observatory Plans for an Early Science Program*.

Guzik, P. et al. (2020). *Nature Astronomy* 4, pp. 53–57.

Hallatt, T. and Wiegert, P. (2020). AJ 159.4, 147, p. 147.

Halley, E. (1704). *Philosophical Transactions of the Royal Society of London Series I* 24, pp. 1882–1899.

Hands, T. O. et al. (2019). MNRAS 490.1, pp. 21–36.

Hansen, B. and Zuckerman, B. (2017). *Research Notes of the American Astronomical Society* 1.1, 55, p. 55.

Harp, G. R. et al. (2019). *Acta Astronautica* 155, pp. 51–54.

Harris, A. W. and Pravec, P. (2006). In: *Asteroids, Comets, Meteors*. Ed. by D. Lazzaro, S. Ferraz-Mello, and J. A. Fernández. Vol. 229. IAU Symposium, pp. 439–447.

Hashimoto, T. et al. (2020a). MNRAS 497.4, pp. 4107–4116.

Hashimoto, T. et al. (2020b). MNRAS 498.3, pp. 3927–3945.

Hashimoto, T. et al. (2022). MNRAS 511.2, pp. 1961–1976.

Haywood, M. et al. (2013). A&A 560, A109, A109.

Hearnshaw, J. B. (1972). MmRAS 77, p. 55.

Heger, A. et al. (2003). ApJ 591.1, pp. 288–300.

Heidarzadeh, T. (2008). *A History of Physical Theories of Comets, From Aristotle to Whipple*.

Heyl, J., Caiazzo, I., and Richer, H. B. (2022). ApJ 926.2, 132, p. 132.

Hoang, T. and Loeb, A. (2020). ApJ 899.2, L23, p. L23.

Hoang, T. and Loeb, A. (2023). ApJ 951.2, L34, p. L34.

Hobbs, G. et al. (2005). MNRAS 360.3, pp. 974–992.

Hog, E., Novikov, I. D., and Polnarev, A. G. (1995). A&A 294, pp. 287–294.

Holtzman, J. A. et al. (2018). AJ 156.3, 125, p. 125.

Hoover, D. J., Seligman, D. Z., and Payne, M. J. (2022). PSJ 3.3, 71, p. 71.

Hopkins, M. J., Bannister, M. T., and Lintott, C. (2025a). AJ 169.2, 78, p. 78.

Hopkins, M. J. et al. (2023). AJ 166.6, 241, p. 241.

Hopkins, M. J. et al. (2025b). *arXiv e-prints*, arXiv:2507.05318, arXiv:2507.05318.

Hsieh, C.-H., Laughlin, G., and Arce, H. G. (2021). ApJ 917.1, 20, p. 20.

Hui, M.-T. and Knight, M. M. (2019). AJ 158.6, 256, p. 256.

Hui, M.-T. et al. (2020). AJ 160.2, 92, p. 92.

Hunt, J. A. S. et al. (2018). MNRAS 481.3, pp. 3794–3803.

Hunt, J. A. S. et al. (2019). MNRAS 490.1, pp. 1026–1043.

Ivezić, Ž. et al. (2019). ApJ 873.2, 111, p. 111.

Iwamoto, K. et al. (1999). ApJS 125.2, pp. 439–462.

Izidoro, A. et al. (2022). *Nature Astronomy* 6, pp. 357–366.

Jackson, A. P. and Desch, S. J. (2021). *Journal of Geophysical Research (Planets)* 126.5, e06706, e06706.

Jackson, A. P. et al. (2018). MNRAS 478.1, pp. L49–L53.

Janes, K. A. and McClure, R. D. (1972). In: *Bulletin of the American Astronomical Society*. Vol. 4, p. 241.

Janka, H.-T. (2012). *Annual Review of Nuclear and Particle Science* 62.1, pp. 407–451.

Janka, H.-T. (2013). MNRAS 434.2, pp. 1355–1361.

Jennings, R. J., Cordes, J. M., and Chatterjee, S. (2020). ApJ 889.2, 145, p. 145.

Jenniskens, P. (1998). *Earth, Planets and Space* 50.6-7, pp. 555–567.

Jewitt, D. and Luu, J. (2019). ApJ 886.2, L29, p. L29.

Jewitt, D. and Seligman, D. Z. (2023). ARA&A 61, pp. 197–236.

Jewitt, D. et al. (2017). ApJ 850.2, L36, p. L36.

Jewitt, D. et al. (2020a). ApJ 896.2, L39, p. L39.

Jewitt, D. et al. (2020b). ApJ 888.2, L23, p. L23.

Jiménez-Esteban, F. M. et al. (2023). MNRAS 518.4, pp. 5106–5122.

Jones, G. H. et al. (2018). Space Sci. Rev. 214.1, 20, p. 20.

Jones, G. H. et al. (2024). Space Sci. Rev. 220.1, 9, p. 9.

Jönsson, H. et al. (2020). AJ 160.3, 120, p. 120.

Jurić, M. et al. (2008). ApJ 673.2, pp. 864–914.

Kaib, N. A., Roškar, R., and Quinn, T. (2011). Icarus 215.2, pp. 491–507.

Kaib, N. A. and Volk, K. (2022). *arXiv e-prints*, arXiv:2206.00010, arXiv:2206.00010.

Kareta, T. et al. (2025). *arXiv e-prints*, arXiv:2507.12234, arXiv:2507.12234.

Katz, J. I. (2018). MNRAS 478.1, pp. L95–L98.

Keller, H. U. (1989). In: *Physics and Mechanics of Cometary Materials*. Ed. by J. J. Hunt and T. D. Guyenne. Vol. 302. ESA Special Publication, pp. 39–45.

Kenyon, S. J. (2002). PASP 114.793, pp. 265–283.

Kim, S.-L. et al. (2016). *Journal of Korean Astronomical Society* 49.1, pp. 37–44.

Kim, Y. et al. (2020). ApJ 895.2, L34, p. L34.

Kipping, D. (2025). *arXiv e-prints*, arXiv:2504.05993, arXiv:2504.05993.

Kirsten, F. et al. (2022). Nature 602.7898, pp. 585–589.

Kirsten, F. et al. (2024). *Nature Astronomy* 8, pp. 337–346.

Knight, M. M. et al. (2017). ApJ 851.2, L31, p. L31.

Kormendy, J. and Kennicutt Jr., R. C. (2004). ARA&A 42.1, pp. 603–683.

Królikowska, M. (2004). A&A 427, pp. 1117–1126.

Kroupa, P. (2001). MNRAS 322.2, pp. 231–246.

Kuiper, G. P. (1938). ApJ 88, p. 472.

Lacey, C. G. (1984). MNRAS 208, pp. 687–707.

Lallement, R. et al. (2022). A&A 661, A147, A147.

Lam, C. Y. and Lu, J. R. (2023). ApJ 955.2, 116, p. 116.

Laplace, P.-S. (1813). "Sur les Cometès". In: *Connaissance des temps ou des mouvements célestes à l'usage des astronomes et des navigateurs*. Le Bureau des Longitudes.

Larson, R. B. (1976). MNRAS 176, pp. 31–52.

Lauretta, D. S. et al. (2017). Space Sci. Rev. 212.1-2, pp. 925–984.

Lawler, S. M. et al. (2018). AJ 155.5, 197, p. 197.

Leavitt, H. S. and Pickering, E. C. (1912). *Harvard College Observatory Circular* 173, pp. 1–3.

Lebreton, Y. and Montalbán, J. (2009). In: *The Ages of Stars*. Ed. by E. E. Mamajek, D. R. Soderblom, and R. F. G. Wyse. Vol. 258. IAU Symposium, pp. 419–430.

Leung, H. W. and Bovy, J. (2019a). MNRAS 483.3, pp. 3255–3277.

Leung, H. W. and Bovy, J. (2019b). MNRAS 489.2, pp. 2079–2096.

Leung, H. W. et al. (2023). MNRAS 519.1, pp. 948–960.

Levine, W. G. and Laughlin, G. (2021). ApJ 912.1, 3, p. 3.

Levine, W. G. et al. (2021). ApJ 922.1, 39, p. 39.

Levine, W. G. et al. (2023). PSJ 4.7, 124, p. 124.

Lian, J. et al. (2022a). MNRAS 511.4, pp. 5639–5655.

Lian, J. et al. (2022b). MNRAS 513.3, pp. 4130–4151.

Licquia, T. C. and Newman, J. A. (2015). ApJ 806.1, 96, p. 96.

Ligterink, N. F. W. (2023). Nature 623.7989, E14–E15.

Lin, H.-N., Li, X.-Y., and Zou, R. (2024). ApJ 969.2, 123, p. 123.

Lin, H.-N. and Zou, R. (2024). ApJ 962.1, 73, p. 73.

Lindegren, L. et al. (2021). A&A 649, A4, A4.

Lintott, C., Bannister, M. T., and Mackereth, J. T. (2022). ApJ 924.1, L1, p. L1.

Lintott, C. J. et al. (2008). MNRAS 389.3, pp. 1179–1189.

Lisse, C. M. et al. (2022). PSJ 3.5, 112, p. 112.

Loeb, A. (2021). *Extraterrestrial: the first sign of intelligent life beyond Earth*.

Loeb, A. (2022). *Astrobiology* 22.12, pp. 1392–1399.

Lorek, S. and Johansen, A. (2024). A&A 683, A38, A38.

Lorimer, D. R. et al. (2007). *Science* 318.5851, p. 777.

LSST Science Collaboration et al. (2009). *arXiv e-prints*, arXiv:0912.0201, arXiv:0912.0201.

Lu, C. X., Schlaufman, K. C., and Cheng, S. (2020a). AJ 160.6, 253, p. 253.

Lu, W., Piro, A. L., and Waxman, E. (2020b). MNRAS 498.2, pp. 1973–1982.

Lucchini, S. et al. (2023). MNRAS 519.1, pp. 432–444.

Luu, J. X., Flekkøy, E. G., and Toussaint, R. (2020). ApJ 900.2, L22, p. L22.

Lyne, A. G. and Lorimer, D. R. (1994). Nature 369.6476, pp. 127–129.

Lyttleton, R. A. (1948). MNRAS 108, p. 465.

Mackereth, J. T. et al. (2017). MNRAS 471.3, pp. 3057–3078.

Mackereth, J. T. et al. (2018). MNRAS 477.4, pp. 5072–5089.

Mackereth, J. T. et al. (2019). MNRAS 489.1, pp. 176–195.

Macquart, J. .-. et al. (2020). Nature 581.7809, pp. 391–395.

Madau, P. and Dickinson, M. (2014). ARA&A 52, pp. 415–486.

Maeder, A. (1992). A&A 264.1, pp. 105–120.

Majewski, S. R. et al. (2017). AJ 154.3, 94, p. 94.

Mamajek, E. (2017). *Research Notes of the American Astronomical Society* 1.1, 21, p. 21.

Mandel, I. (2016). MNRAS 456.1, pp. 578–581.

Mannings, A. G. et al. (2021). ApJ 917.2, 75, p. 75.

Marčeta, D. (2023). *Astronomy and Computing* 42, 100690, p. 100690.

Marčeta, D. and Novaković, B. (2020). MNRAS 498.4, pp. 5386–5398.

Marčeta, D. and Seligman, D. Z. (2023). PSJ 4.12, 230, p. 230.

Marcote, B. et al. (2022). In: *European VLBI Network Mini-Symposium and Users' Meeting 2021*. Vol. 2021, 35, p. 35.

Margalit, B., Berger, E., and Metzger, B. D. (2019). ApJ 886.2, 110, p. 110.

Margalit, B. and Metzger, B. D. (2017). ApJ 850.2, L19, p. L19.

Margot, J. L. et al. (2002). *Science* 296.5572, pp. 1445–1448.

Marigo, P. et al. (2017). ApJ 835.1, 77, p. 77.

Marsden, B. G., Sekanina, Z., and Yeomans, D. K. (1973). AJ 78, p. 211.

Marshall, D. J. et al. (2006). A&A 453.2, pp. 635–651.

Martig, M. et al. (2016). MNRAS 456.4, pp. 3655–3670.

Mashchenko, S. (2019). MNRAS 489.3, pp. 3003–3021.

Mashonkina, L. I. et al. (2019). *Astronomy Reports* 63.9, pp. 726–738.

Masiero, J. (2017). *arXiv e-prints*, arXiv:1710.09977, arXiv:1710.09977.

Mason, B. D. et al. (2009). AJ 137.2, pp. 3358–3377.

Mātāmua, R. (2020). "Matariki and the decolonisation of time". In: *Routledge Handbook of Critical Indigenous Studies*. Ed. by B. Hokowhitu et al. 1. Routledge.

Matteucci, F. (2021). A&A Rev. 29.1, 5, p. 5.

Maury, A. C. and Pickering, E. C. (1897). *Annals of Harvard College Observatory* 28, pp. 1–128.

McDonald, C. H. and Veras, D. (2023). MNRAS 520.3, pp. 4009–4022.

McDowell, J. (2025). *Research Notes of the American Astronomical Society* 9.3, 55, p. 55.

McGlynn, T. A. and Chapman, R. D. (1989). ApJ 346, p. L105.

McKay, A. J. et al. (2020). ApJ 889.1, L10, p. L10.

McLaughlin, M. A. (2013). *Classical and Quantum Gravity* 30.22, 224008, p. 224008.

Meech, K. J. et al. (2016). *Science Advances* 2, e1600038, e1600038.

Meech, K. J. et al. (2017). Nature 552.7685, pp. 378–381.

Meech, K. J. et al. (2023). *Close up samples of Exoplanetary Systems: Characterizing the next Interstellar Object*. JWST Proposal. Cycle 2, ID. #4116.

Metzger, B. D., Margalit, B., and Sironi, L. (2019). MNRAS 485.3, pp. 4091–4106.

Micheli, M. et al. (2018). Nature 559, pp. 223–226.

Michilli, D. et al. (2023). ApJ 950.2, 134, p. 134.

Michtchenko, T. A. et al. (2018). ApJ 863.2, L37, p. L37.

Miller, M. C. et al. (2021). ApJ 918.2, L28, p. L28.

Mondal, T. (2021). ApJ 913.1, L12, p. L12.

Moniez, M. et al. (2017). A&A 604, A124, A124.

Moore, K. et al. (2021). Planet. Space Sci. 197, 105137, p. 105137.

Morbidelli, A. et al. (2005). Nature 435.7041, pp. 462–465.

Morgan, W. W., Sharpless, S., and Osterbrock, D. (1952). AJ 57, pp. 3–3.

Morgan, W. W., Whitford, A. E., and Code, A. D. (1953). ApJ 118, p. 318.

Moro-Martín, A. (2018). ApJ 866.2, 131, p. 131.

Moro-Martín, A. (2019). ApJ 872.2, L32, p. L32.

Moro-Martín, A. and Norman, C. (2022). ApJ 924.2, 96, p. 96.

Moro-Martín, A., Turner, E. L., and Loeb, A. (2009). ApJ 704.1, pp. 733–742.

Mužić, K. et al. (2015). ApJ 810.2, 159, p. 159.

Navarro, J. F. et al. (2011). MNRAS 412.2, pp. 1203–1209.

Nelsen, M. A. et al. (2025). PSJ 6.3, 53, p. 53.

Nesvorný, D. (2018). ARA&A 56, pp. 137–174.

Newton, I. (1687). *Philosophiae Naturalis Principia Mathematica.*

Nimmo, K. et al. (2023). MNRAS 520.2, pp. 2281–2305.

Nomoto, K., Thielemann, F. .-., and Yokoi, K. (1984). ApJ 286, pp. 644–658.

Nordström, B. et al. (2004). A&A 418, pp. 989–1019.

O'Dell, C. R. and Wong, K. (1996). AJ 111, p. 846.

Öberg, K. I. and Bergin, E. A. (2021). Phys. Rep. 893, pp. 1–48.

Oke, J. B. and Gunn, J. E. (1982). PASP 94, p. 586.

Oort, J. H. (1927). Bull. Astron. Inst. Netherlands 3, p. 275.

Oort, J. H. (1950). Bull. Astron. Inst. Netherlands 11, pp. 91–110.

Öpik, E. (1932). *Proceedings of the American Academy of Arts and Sciences* 67, p. 169.

Öpik, E. J. (1951). *Pattern Recognition and Image Analysis* 54, pp. 165–199.

Opitom, C. et al. (2019). A&A 631, L8, p. L8.

Opitom, C. et al. (2025). *arXiv e-prints*, arXiv:2507.05226, arXiv:2507.05226.

Osborn, A. and Bayliss, D. (2020). MNRAS 491.3, pp. 4481–4487.

Ovid (8). *Metamorphoses*.

Parenago, P. P. (1951). *Trudy Gosudarstvennogo Astronomicheskogo Instituta* 20, pp. 26–80.

Park, R. S. et al. (2018). AJ 155.5, 185, p. 185.

Payne-Gaposchkin, C. H. (1925). "Stellar atmospheres: A contribution to the observational study of high temperature in the reversing layers of stars". PhD thesis. Radcliffe College, United States.

Penny, M. T. et al. (2019). ApJS 241.1, 3, p. 3.

Petigura, E. A., Howard, A. W., and Marcy, G. W. (2013). *Proceedings of the National Academy of Science* 110.48, pp. 19273–19278.

Petigura, E. A. et al. (2018). AJ 155.2, 89, p. 89.

Petit, J.-M., Morbidelli, A., and Chambers, J. (2001). Icarus 153.2, pp. 338–347.

Pfalzner, S. and Bannister, M. T. (2019). ApJ 874.2, L34, p. L34.

Pfalzner, S. and Dincer, F. (2024). ApJ 963.2, 122, p. 122.

Pfalzner, S. et al. (2020). ApJ 903.2, 114, p. 114.

Pfalzner, S. et al. (2021a). ApJ 921.2, 168, p. 168.

Pfalzner, S. et al. (2021b). A&A 651, A38, A38.

Pham, D. et al. (2024). ApJ 977.2, 232, p. 232.

Phan, V. H. M., Hoang, T., and Loeb, A. (2021). *arXiv e-prints*, arXiv:2109.04494, arXiv:2109.04494.

Pilmer, H. (1937). *The Pageant of Persia*. Kegan Paul, Trench, Trubner & Co.

Planck Collaboration et al. (2020). A&A 641, A6, A6.

Platts, E. et al. (2019). Phys. Rep. 821, pp. 1–27.

Pleunis, Z. et al. (2021). ApJ 923.1, 1, p. 1.

Portegies Zwart, S. (2021). A&A 647, A136, A136.

Portegies Zwart, S. et al. (2018). MNRAS 479.1, pp. L17–L22.

Posti, L. and Helmi, A. (2019). A&A 621, A56, A56.

Powell, A. L. T. (1972). MNRAS 155, p. 483.

Protopapa, S. et al. (2017). Icarus 287, pp. 218–228.

Quillen, A. C. et al. (2011). MNRAS 417.1, pp. 762–784.

Rafikov, R. R. (2018a). ApJ 861.1, 35, p. 35.

Rafikov, R. R. (2018b). ApJ 867.1, L17, p. L17.

Rakavy, G. and Shaviv, G. (1967). ApJ 148, p. 803.

Ramos, P., Antoja, T., and Figueras, F. (2018). A&A 619, A72, A72.

Raymond, S. N., Armitage, P. J., and Veras, D. (2018a). ApJ 856.1, L7, p. L7.

Raymond, S. N. and Izidoro, A. (2017). *Science Advances* 3.9, e1701138.

Raymond, S. N. et al. (2018b). MNRAS 476.3, pp. 3031–3038.

Raymond, S. N. et al. (2020). ApJ 904.1, L4, p. L4.

Rebassa-Mansergas, A. et al. (2021). MNRAS 505.3, pp. 3165–3176.

Reber, G. (1944). ApJ 100, p. 279.

Recio-Blanco, A. et al. (2014). A&A 567, A5, A5.

Recio-Blanco, A. et al. (2023). A&A 674, A29, A29.

Reddy, V. et al. (2012). Icarus 219.1, pp. 382–392.

Reddy, V. et al. (2021). In: *7th IAA Planetary Defense Conference*, 36, p. 36.

Reisenegger, A. (2003). *arXiv e-prints*, astro-ph/0307133, astro–ph/0307133.

Repetto, S., Davies, M. B., and Sigurdsson, S. (2012). MNRAS 425.4, pp. 2799–2809.

Roman, N. G. (1954). AJ 59, pp. 307–312.

Rose, S. et al. (2022). ApJ 941.2, 116, p. 116.

Ryder, S. D. et al. (2023). *Science* 382.6668, pp. 294–299.

Sabhahit, G. N. et al. (2023). MNRAS 524.1, pp. 1529–1546.

Sahu, K. C. et al. (2022). ApJ 933.1, 83, p. 83.

Sajadian, S. and Sahu, K. C. (2023). AJ 165.3, 96, p. 96.

Salaris, M. and Cassisi, S. (2005). *Evolution of Stars and Stellar Populations*.

Salaris, M. et al. (2015). A&A 583, A87, A87.

Sana, H. et al. (2012). *Science* 337.6093, p. 444.

Sana, H. and Evans, C. J. (2011). In: *Active OB Stars: Structure, Evolution, Mass Loss, and Critical Limits*. Ed. by C. Neiner et al. Vol. 272. IAU Symposium, pp. 474–485.

Santos, N. C., Israelian, G., and Mayor, M. (2004). A&A 415, pp. 1153–1166.

Savitzky, A. and Golay, M. J. E. (1964). *Analytical Chemistry* 36, pp. 1627–1639.

Schaye, J. et al. (2015). MNRAS 446.1, pp. 521–554.

Schlesinger, K. J. et al. (2014). ApJ 791.2, 112, p. 112.

Schmidt, M. (1963). ApJ 137, p. 758.

Schneider, J. (2017). *Research Notes of the American Astronomical Society* 1.1, 18, p. 18.

Schönrich, R. and Binney, J. (2009a). MNRAS 396.1, pp. 203–222.

Schönrich, R. and Binney, J. (2009b). MNRAS 399.3, pp. 1145–1156.

Schönrich, R., Binney, J., and Dehnen, W. (2010). MNRAS 403.4, pp. 1829–1833.

Schramm, D. N. and Turner, M. S. (1998). *Reviews of Modern Physics* 70.1, pp. 303–318.

Schwamb, M. E. et al. (2019). ApJS 243.1, 12, p. 12.

Schwamb, M. E. et al. (2021). *Research Notes of the American Astronomical Society* 5.6, 143, p. 143.

Schwamb, M. E. et al. (2023). ApJS 266.2, 22, p. 22.

Sekanina, Z. (1968). *Bulletin of the Astronomical Institutes of Czechoslovakia* 19, p. 343.

Sekanina, Z. (1976). Icarus 27.1, pp. 123–133.

Sekanina, Z. (2001). *Publications of the Astronomical Institute of the Czechoslovak Academy of Sciences* 89, pp. 78–93.

Sekanina, Z. (2019a). *arXiv e-prints*, arXiv:1901.08704, arXiv:1901.08704.

Sekanina, Z. (2019b). *arXiv e-prints*, arXiv:1905.00935, arXiv:1905.00935.

Seligman, D. and Laughlin, G. (2018). AJ 155.5, 217, p. 217.

Seligman, D. and Laughlin, G. (2020). ApJ 896.1, L8, p. L8.

Seligman, D., Laughlin, G., and Batygin, K. (2019). ApJ 876.2, L26, p. L26.

Seligman, D. Z. et al. (2021). ApJ 920.1, 28, p. 28.

Seligman, D. Z. et al. (2022). PSJ 3.7, 150, p. 150.

Seligman, D. Z. et al. (2023). PSJ 4.2, 35, p. 35.

Seligman, D. Z. et al. (2025). *arXiv e-prints*, arXiv:2507.02757, arXiv:2507.02757.

Sellwood, J. A. and Binney, J. J. (2002). MNRAS 336.3, pp. 785–796.

Shapiro, S. L. and Teukolsky, S. A. (1983). *Black holes, white dwarfs and neutron stars. The physics of compact objects*.

Shapley, H. (1939). *Proceedings of the National Academy of Science* 25.3, pp. 113–118.

Shaver, P. A. et al. (1983). MNRAS 204, pp. 53–112.

Shoemaker, E. M. and Wolfe, R. F. (1984). In: *Lunar and Planetary Science Conference*. Lunar and Planetary Science Conference, pp. 780–781.

Simon, J. B. et al. (2016). ApJ 822.1, 55, p. 55.

Siraj, A. and Loeb, A. (2022). New A 92, 101730, p. 101730.

Siraj, A. and Loeb, A. (2019a). *Research Notes of the American Astronomical Society* 3.9, 130, p. 130.

Siraj, A. and Loeb, A. (2019b). *arXiv e-prints*, arXiv:1904.07224, arXiv:1904.07224.

Siraj, A. et al. (2023). *Journal of Astronomical Instrumentation* 12.1, 2340001-12, pp. 2340001–12.

Skuljan, J., Hearnshaw, J. B., and Cottrell, P. L. (1999). MNRAS 308.3, pp. 731–740.

Smallwood, J. L., Martin, R. G., and Zhang, B. (2019). MNRAS 485.1, pp. 1367–1376.

Smith, B. A. and Terrile, R. J. (1984). *Science* 226.4681, pp. 1421–1424.

Spada, F. (2025). *Research Notes of the American Astronomical Society* 9.3, 58, p. 58.

Spergel, D. et al. (2015). *arXiv e-prints*, arXiv:1503.03757, arXiv:1503.03757.

Stanek, K. Z. et al. (1994). ApJ 429, p. L73.

Stanford, P. K. (2006). *Exceeding Our Grasp: Science, History, and the Problem of Unconceived Alternatives*. Oxford University Press.

Stern, S. A. (1990). PASP 102, p. 793.

Stern, S. A. (1995). AJ 110, p. 856.

Stern, S. A. and Shull, J. M. (1988). Nature 332.6163, pp. 407–411.

Stern, S. A. (1989). "The Evolution of Comets and the Detectability of Extra-Solar Oort Clouds." PhD thesis. University of Colorado, Boulder.

Sturm, J. A. et al. (2023). A&A 679, A138, A138.

Sweeney, D. et al. (2022). MNRAS 516.4, pp. 4971–4979.

Tang, L., Lin, H.-N., and Li, X. (2023). *Chinese Physics C* 47.8, 085105, p. 085105.

Taylor, A. G. et al. (2023). PSJ 4.10, 186, p. 186.

Taylor, A. G. et al. (2024a). Icarus 408, 115822, p. 115822.

Taylor, A. G. et al. (2024b). ApJ 976.2, 190, p. 190.

Tinsley, B. M. (1980). Fund. Cosmic Phys. 5, pp. 287–388.

Trapman, L. et al. (2020). A&A 640, A5, A5.

Trick, W. H. et al. (2021). MNRAS 500.2, pp. 2645–2665.

Trilling, D. E. et al. (2018). AJ 156.6, 261, p. 261.

Trimble, V. (1982). *Reviews of Modern Physics* 54.4, pp. 1183–1224.

Tsiganis, K. et al. (2005). Nature 435.7041, pp. 459–461.

Udalski, A., Szymański, M. K., and Szymański, G. (2015). Acta Astron. 65.1, pp. 1–38.

Udalski, A. et al. (1992). Acta Astron. 42, pp. 253–284.

van de Hulst, H. C., Muller, C. A., and Oort, J. H. (1954). Bull. Astron. Inst. Netherlands 12, p. 117.

van Woerkom, A. J. J. (1948). Bull. Astron. Inst. Netherlands 10, pp. 445–472.

Vanderlinde, K. et al. (2019). In: *Canadian Long Range Plan for Astronomy and Astrophysics White Papers*. Vol. 2020, 28, p. 28.

Vaubaillon, J. (2022). *WGN, Journal of the International Meteor Organization* 50.5, pp. 140–143.

Vavilov, D. E. and Medvedev, Y. D. (2019). MNRAS 484.1, pp. L75–L78.

Veras, D. et al. (2011). MNRAS 417.3, pp. 2104–2123.

Veras, D. et al. (2014). MNRAS 437.2, pp. 1127–1140.

Vickers, J. J., Shen, J., and Li, Z.-Y. (2021). ApJ 922.2, 189, p. 189.

Vokrouhlický, D. and Milani, A. (2000). A&A 362, pp. 746–755.

Wadiasingh, Z. and Timokhin, A. (2019). ApJ 879.1, 4, p. 4.

Walker, M. A. (1995). ApJ 453, p. 37.

Walker, T. P. et al. (1991). ApJ 376, p. 51.

Walsh, C. et al. (2014). A&A 563, A33, A33.

Walsh, K. J. and Richardson, D. C. (2006). Icarus 180.1, pp. 201–216.

Walsh, K. J., Richardson, D. C., and Michel, P. (2008). Nature 454.7201, pp. 188–191.

Weber, E. J. and Davis Jr., L. (1967). ApJ 148, pp. 217–227.

Weisberg, J. M. and Taylor, J. H. (2003). In: *Radio Pulsars*. Ed. by M. Bailes, D. J. Nice, and S. E. Thorsett. Vol. 302. Astronomical Society of the Pacific Conference Series, p. 93.

Weissman, P. R. (1983). A&A 118.1, pp. 90–94.

Weissman, P. R. (1986). Nature 320.6059, pp. 242–244.

Wheeler, J. C., Sneden, C., and Truran Jr., J. W. (1989). ARA&A 27, pp. 279–349.

Whipple, F. L. (1975). AJ 80, pp. 525–531.

Whipple, F. L. (1939). *Proceedings of the National Academy of Science* 25.3, pp. 118–125.

Whipple, F. L. (1950). ApJ 111, pp. 375–394.

Whipple, F. L. (1951). ApJ 113, p. 464.

Whipple, F. L. (1955). ApJ 121, p. 750.

Wielen, R. (1977). A&A 60.2, pp. 263–275.

Wiersma, R. P. C. et al. (2009). MNRAS 399.2, pp. 574–600.

Wiktorowicz, G. et al. (2019). ApJ 885.1, 1, p. 1.

Williams, T. G. et al. (2022). MNRAS 509.1, pp. 1303–1322.

Wilson, R. F. et al. (2022). AJ 163.3, 128, p. 128.

Winter, O. C. et al. (2020). MNRAS 492.3, pp. 4437–4455.

Wolszczan, A. and Frail, D. A. (1992). Nature 355.6356, pp. 145–147.

Wootten, A. and Thompson, A. R. (2009). *IEEE Proceedings* 97.8, pp. 1463–1471.

Worden, S. P. et al. (2017). *Acta Astronautica* 139, pp. 98–101.

Wright, J. T. (2022). *Acta Astronautica* 190, pp. 24–29.

Wyrzykowski, Ł. et al. (2016). MNRAS 458.3, pp. 3012–3026.

Wyrzykowski, Ł. et al. (2023). A&A 674, A23, A23.

Xing, Z. et al. (2020). ApJ 893.2, L48, p. L48.

Yabushita, S. (1996). MNRAS 283, p. 347.

Yang, B. et al. (2025). *arXiv e-prints*, arXiv:2507.14916, arXiv:2507.14916.

Ye, Q.-Z. et al. (2017). ApJ 851.1, L5, p. L5.

Ye, Q. et al. (2020). AJ 159.2, 77, p. 77.

Yeomans, D. K. (1994). In: *Asteroids, Comets, Meteors 1993*. Ed. by A. Milani, M. di Martino, and A. Cellino. Vol. 160. IAU Symposium, p. 241.

Young, L. A. et al. (2008). Space Sci. Rev. 140.1-4, pp. 93–127.

Zasowski, G. et al. (2013). AJ 146.4, 81, p. 81.

Zasowski, G. et al. (2017). AJ 154.5, 198, p. 198.

Zhang, B. (2020). Nature 587.7832, pp. 45–53.

Zhang, K. J. et al. (2024). *arXiv e-prints*, arXiv:2406.00476, arXiv:2406.00476.

Zhang, Q. (2018). ApJ 852.1, L13, p. L13.

Zhang, R. C. and Zhang, B. (2022). ApJ 924.1, L14, p. L14.

Zhang, Y. and Lin, D. N. C. (2020). *Nature Astronomy* 4, pp. 852–860.

Zhao, J., Zhao, G., and Chen, Y. (2009). ApJ 692.2, pp. L113–L117.

Zhao, P. and Lai, L. (2020). *arXiv e-prints*, arXiv:2010.00438, arXiv:2010.00438.

Zhen-Tao, X., Stephenson, F. R., and Yao-Tiao, J. (1995). QJRAS 36, p. 397.

Zhou, W.-H. et al. (2022). A&A 667, A108, A108.

Zuluaga, J. I. et al. (2018). AJ 155.6, 236, p. 236.